

Everything has shape, if you look for it. There is no escape from form.

Salman Rushdie  
From "Midnight's Children" (1981)

# University of Alberta

## Active Open-Loop Control of a Backward-Facing Step Flow

by

Aaron R. Baugh

A thesis submitted to the Faculty of Graduate Studies and Research  
in partial fulfillment of the requirements for the degree of

Master of Science

Department of Mechanical Engineering

©Aaron R. Baugh

Fall 2010

Edmonton, Alberta

Permission is hereby granted to the University of Alberta Libraries to reproduce single copies of this thesis and to lend or sell such copies for private, scholarly or scientific research purposes only. Where the thesis is converted to, or otherwise made available in digital form, the University of Alberta will advise potential users of the thesis of these terms.

The author reserves all other publication and other rights in association with the copyright in the thesis and, except as herein before provided, neither the thesis nor any substantial portion thereof may be printed or otherwise reproduced in any material form whatsoever without the author's prior written permission.

## **Examining Committee**

Lorenz Sigurdson, Mechanical Engineering

Roger Toogood, Mechanical Engineering

Mark Loewen, Civil and Environmental Engineering

Für meinen Opa, der an mich glaubt, auch dann wenn ich es nicht tue.

## **Abstract**

A robotically-controlled actuation system has been developed and built to perform active open-loop flow control experiments on transitional and turbulent backward-facing step flows in water. Control of the reattaching shear layer used hydraulic suction-and-blowing actuation emanating from 128 individual ports along the separation edge of the step. Each port's perturbation was periodic in time, but individually controlled to produce either spanwise-invariant (2D) or spanwise-varying (3D) spatial actuation profiles. An image processing system and special aqueous tuft were developed to measure the length of the recirculation bubble. Multiple images of a tuft array were time-averaged to do so. In general, 3D forcing was no more effective in reducing bubble length than 2D forcing. However, greater local spanwise reductions in reattachment length were observed for some cases of spanwise-varying forcing. Backlit dye was used to track the evolution of vorticity in the flow in video and still images.

## Acknowledgements

First, I would to thank Dr. Lorenz Sigurdson; his aerodynamics course inspired me to pursue a graduate degree, and his guidance, friendship, and (probably most importantly) patience helped me through it. I also wish to thank all past and present V $f$ DL group members: Stuart Gilbert for entrusting me with his prototype brainchild, Marc Schostek for his brilliant tuft and RPM sensor inventions, David Breakey for his invaluable contributions to the control and image processing aspects of the project, Dory Parsonage for his construction expertise and tuft work, Nesma Ansari and Jordan Leung for their assistance with the light table, and Graeme Watson and Justin Wiwchar for helping a frightened new grad student acclimatize to the fast-paced world of fluid dynamics.

I am also eternally indebted to the machine shop/electronics lab staff for their assistance in constructing various aspects of the RoboStep experiment, and for fixing things whenever I broke them. In particular, this project would not yet be completed without the help of Bernie Faulkner, Rick Bubenko, Roger Marchand, Greg Miller, or Rick Conrad.

I would like to say a special thank you to Marc “Marco” Schostek and Gillian “Redmanus Maximus” Redman, who over the past two years have grown from colleagues into lifelong friends. We truly are the three prettiest fluid dynamicists in Western Canada (and I’m still number one). Marc, your ability to be completely enthusiastic about anything never ceases to amaze me. Thank you for inspiring me to pick up a guitar, and for trusting me enough to let me fly a plane with you in it. Jill, thanks for making the unbearable parts of grad school bearable, and also for your perpetual willingness to go for afternoon beers at RATT.

Last (but certainly not least), I would like to thank my family (Dad, Mom, Lauren, Opa, Oma, and Luca) and my wonderful girlfriend Sarah; for both their continued love and support, and also for their tolerance of my mood swings throughout this whole ordeal.

# Contents

1	Introduction .....	1
1.1	Objectives.....	2
1.2	Thesis Outline .....	3
2	Literature Review .....	5
2.1	The Backward-Facing Step (BFS) .....	5
2.2	Previous BFS Flow Control .....	7
2.3	Vorticity and the BFS.....	10
2.3.1	Spanwise and Sidewall Vortices.....	10
2.3.2	Corner Vortices.....	11
2.3.3	Taylor-Görtler Vortices .....	11
3	Experimental Apparatus .....	13
3.1	Overview .....	13
3.2	The “RoboStep” .....	15
3.3	The Gilbert Prototype Actuator (2007) .....	22
3.3.1	Technology Selection Review .....	22
3.3.2	The Selected Prototype .....	23
3.3.3	Initial Performance Testing.....	25
3.3.4	Alterations Made to the Prototype .....	25
3.3.5	The Actuator Board.....	26
3.3.6	Power Connections .....	28
3.3.7	Actuator Control .....	29
3.4	Hydraulic Connections.....	31
3.4.1	Actuator-to-RoboStep Connection Overview.....	31
3.4.2	Experimental Connections .....	33
3.5	Dye Injection System .....	34
4	Methodology.....	37
4.1	Overview .....	37
4.2	Actuation Characteristics .....	37

4.2.1	Forcing Amplitudes .....	37
4.2.2	Spanwise Wavelengths .....	38
4.3	Experiments Visited .....	39
4.3.1	Overview .....	39
4.3.2	Reattachment Length vs. Reynolds Number .....	40
4.3.3	Two-Dimensional Forcing .....	41
4.3.3.1	Reattachment Length vs. Perturbation Amplitude .....	41
4.3.3.2	Reattachment Length vs. Strouhal Number .....	42
4.3.4	Three-Dimensional Forcing .....	42
4.3.4.1	Spanwise Wavelength and Amplitude Calculations .....	42
4.3.4.2	Reattachment vs. Strouhal Number .....	43
4.3.5	Dye Visualization .....	44
4.4	Reattachment Location Measurement .....	45
4.4.1	Overview .....	45
4.4.2	Tufts .....	46
4.4.2.1	Aqueous Tuft Requirements .....	46
4.4.2.2	Tuft Development .....	46
4.4.2.3	The Tuft Plate .....	47
4.4.3	Data Collection .....	48
4.4.4	Image Processing .....	50
4.4.4.1	Image Registration .....	50
4.4.4.2	Tuft Isolation .....	51
4.4.4.3	Tuft Direction Determination: The Centroid Method .....	51
4.4.4.4	Tuft Direction Determination: The Regression Method .....	51
4.4.4.5	Experiment-Specific Problems .....	53
4.4.4.6	Averaging Velocity Field Data .....	54
5	Results and Discussion .....	59
5.1	Overview .....	59
5.2	Reattachment Length vs. Reynolds Number .....	59
5.3	Two-Dimensional Forcing .....	63
5.3.1	Reattachment vs. Perturbation Amplitude .....	63

5.3.2	Reattachment vs. Strouhal Number .....	64
5.3.2.1	High Reynolds Number .....	64
5.3.2.2	Low Reynolds Number.....	67
5.4	Three-Dimensional Forcing .....	69
5.4.1	Reattachment Length vs. Strouhal Number: The High $Re_h$ Case ...	69
5.4.2	Reattachment Length vs. Strouhal Number: The Low $Re_h$ Case ....	70
5.5	Two-Dimensional vs. Three-Dimensional Forcing.....	71
5.5.1	Effectiveness in Average Reattachment Reduction .....	71
5.5.2	Spanwise Variation of Reattachment.....	74
5.6	Dye Visualization Experiments.....	77
5.6.1	Sample Images and Results .....	77
5.6.2	Effect of Low $Re_h$ Forcing on the Expected Structures .....	81
6	Conclusions and Proposed Future Work .....	83
6.1	Summary and Conclusions.....	83
6.2	Future Work .....	86
6.2.1	Proposed Apparatus Improvements .....	86
6.2.2	Additional Experiments .....	88
6.2.2.1	Low Reynolds Number Testing.....	88
6.2.2.2	Additional Wavelengths .....	89
6.2.2.3	Time-Varying Phase .....	89
6.2.2.4	Multiple Frequency Forcing .....	89
6.2.2.5	Feedback Control.....	91
7	References .....	92
8	Appendices .....	97
	Appendix A: Tunnel Velocity Calibration – RoboStep In.....	98
	Appendix B: Experiments Visited and Complete Results .....	100
	B1: Complete Table of Experiments .....	100
	B2: Complete Table of Results.....	102
	B3: Collection of Generated Charts.....	104
	Appendix C: Operational Procedures.....	124
	C1: Air Bleed.....	124

C2: Actuator Use .....	125
Appendix D: LabVIEW .....	127
D1: TopLevelServoController.vi Program Overview .....	127
D2: Program Usage Instructions.....	127
Appendix E: MATLAB.....	129
E1: tuftImgProApp.m Program Overview: ReadMe.txt.....	129
E2: Screen Images .....	135
Appendix F: Statistical Error Analysis.....	137
F1: Number of Images Necessary for Convergence.....	137
F2: Repeatability of Results .....	138
Appendix G: Fidelity of Forcing.....	139
G1: Initial Calibration Results.....	139
G2: Manual Calibration .....	140
G3: Final Calibration Results .....	140

## List of Tables

Table 3.1 Some pertinent backward-facing step and test section experimental parameters. Original values are shown in the second column, while effective values (which account for the thickness of the tuft plate when it is in place) are displayed in the third column.....	17
Table 3.2 The hydraulic actuation slots that each actuator is connected to. Actuators are numbered according to Section 3.3.7, and actuation slots are numbered from the top of the test section ( $z = 45.72$ cm) to the bottom ( $z = 0$ ).....	34
Table 8.1 (a) Table of experiments, from (1): $X_R$ vs. $Re_h$ to (4): 2D Forcing - $X_R$ vs. $St_h$ ( $Re_h \approx 24500$ ).....	100
Table 8.1 (b) Table of experiments, from (5): 2D Forcing - $X_R$ vs. $St_h$ ( $Re_h \approx 24500$ ) to (9): 3D Forcing - $X_R$ vs. $St_h$ ( $Re_h \approx 24500$ ).....	101
Table 8.1 (c) Table of experiments, from (10): 3D Forcing - $X_R$ vs. $St_h$ ( $Re_h \approx 12540$ ) to (11): 3D Forcing - $X_R$ vs. $St_h$ ( $Re_h \approx 12540$ ).....	102
Table 8.2 (a) Table of results, from (1): $X_R$ vs. $Re_h$ to (2): 2D Forcing - $X_R$ vs. $St_h$ ( $Re_h \approx 24500$ ). Results are shown for each of the 4 $X_R$ calculation methods.....	102
Table 8.2 (b) Table of results, from (3): 2D Forcing - $X_R$ vs. $St_h$ ( $Re_h \approx 24500$ ) to (7): 2D Forcing - $X_R$ vs. $St_h$ ( $Re_h \approx 12540$ ). Results are shown for each of the 4 $X_R$ calculation methods.....	103
Table 8.2 (c) Table of results, from (8): 3D Forcing - $X_R$ vs. $St_h$ ( $Re_h \approx 24500$ ) to (11): 3D Forcing - $X_R$ vs. $St_h$ ( $Re_h \approx 12540$ ). Results are shown for each of the 4 $X_R$ calculation methods.....	104
Table 8.3 Results from 5 separate repeatability verifications performed for our high Reynolds number, 2D forcing experiments.....	138

## List of Figures

Figure 1.1 The 3D vortex structures found in the reattaching shear layer for flow over a blunt-faced cylinder. Taken from Sigurdson [Bull. Am. Phys. Soc. 26, 1275 (1984)], and reproduced here with the express written consent of the author. ....	2
Figure 2.1 A general schematic of an unforced backward-facing step flow. The coordinates are noted, and inlet and time-averaged flow qualities are represented in grey. ....	6
Figure 3.1 An overview of various components of the experimental apparatus. (a) The black, anodized backward-facing step module situated vertically in the test section of the water tunnel, looking from the front of the test section. The separation edge of the step is shown in white, and flow is right to left. (b) Four individual actuators from our actuator array. (c) The system of hydraulic connections, looking from behind the test section. Actuation flow comes from the actuator array on the top of the water, into the distribution manifolds, and then out of the ports at the separation edge of the backward-facing step (again denoted by a white line, flow left to right this time). (d) The storage reservoir for the dye that is used in flow visualization experiments. ....	14
Figure 3.2 A representation of the RoboStep geometry, with key lengths and features noted. Inset: The locations of the dye injection slit and the actuation ports relative to the separation edge of the backward-facing step. The global coordinates are identical to those shown in Figure 2.1. ....	16
Figure 3.3 The RoboStep module. (a) A fully assembled view. (b) An exploded view, showing the dye module (1), the actuator module (2), and the step module (3). ....	19
Figure 3.4 A photograph of the vertical orientation of the backward-facing step (1) in the water tunnel test section (2). The settling tank is labeled as component (3), and the global coordinates are shown. Flow direction $U_\infty$ is indicated, and as before, the separation edge of the RoboStep is indicated by a white line. ....	21
Figure 3.5 A section view sketch of the leading edge gap-bridging connector (shown in grey), and its associated fastening screws. The connector also extends over the flange joint at the connection of the settling tank and test section of the water tunnel. ....	22

Figure 3.6 Four array actuators constructed from the prototype specifications of Gilbert (2007). The pinion gears attached to the servo motors (1) drive the racks (2), which are connected to the syringe plungers (3b) via the syringe housing (4b) and plate (4a) systems. At the end of each syringe (3a), there is a luer lock fitting (5) which is press fit into a 3/8 inch inner diameter reinforced hose. The hoses are held in place by rectangular tube clamps (6). ..... 24

Figure 3.7 The overview of the actuator board situated on top of the water tunnel's settling tank, looking down toward the test section. Point (1) denotes the water tunnel's snorkel, (2) shows the elevated structure for the servo controller card, (3) labels the rail which supports the power wires, and (4) labels an LVDT mounted to the bottom-right servo as used by Marc Schostek in his calibrations (Appendices G1 and G3). ..... 28

Figure 3.8 The power and logic connections for the servos. The large positive (1a) and negative (1b) wires are connected to a power supply providing 6 VDC. Each individual servo has a crimp terminal connection (2) that connects to the main lines using T-connectors (1a) and (1b). Wires (3) and (4) represent the servo potentiometer and servo signal wires, respectively (Section 3.3.7). ..... 29

Figure 3.9 The hydraulic connection system for the RoboStep. (a) An overview of the hydraulic system, looking from the behind the water tunnel. The manifold support frame (1), height-adjustable manifold rack (2), and additional tube reservoir (3) are highlighted. (b) A close up photograph of two manifold pairs (5), with the three major tube diameters noted (4), (6), and (7). In both images, the separation edges of the RoboStep are highlighted by white lines. ..... 32

Figure 3.10 The dye reservoir, and dye reservoir support frame. The frame connects to a cable winch at location (1), and the flow can be controlled by the valve at (2). ..... 35

Figure 3.11 The dye injection system, as it connects into the back of the RoboStep module (viewed from behind the test section). The inflow direction is indicated by the white arrow. The gate valve, dye manifold, and port holes are labeled by (1), (2), and (3), respectively. The separation edge of the BFS is highlighted with a white line. .... 36

Figure 4.1 Our cosine forcing approximation for a spanwise wavelength of  $4h$ , with an arbitrary perturbation amplitude of 1. The upper horizontal axis indicates that for this wavelength, 8 adjacent tubes force at a given velocity type. The

bottom horizontal axis indicates the spanwise location normalized by the actuated span. ....	43
Figure 4.2 The method in which the tuft plate was fastened to the interior side of the water tunnel test section window. ....	48
Figure 4.3 An example of an unprocessed tuft plate image, with the backward-facing step edge and flow directions shown. The reattachment line, estimated by eye, is indicated by the vertical dashed line. A second dashed line highlights a region containing a possible counter rotating streamwise vortex pair, with positive $\omega_x$ at the top of the region and negative $\omega_x$ at the bottom. ....	49
Figure 4.4 Single-image vector field calculation plots. (a) A sample single tuft plate image (vector field superimposed) after image registration. The bolt areas are indicated by the red circles. (b) The resulting output vector field image from the image registration process. Top and bottom water tunnel walls are at $z = 46$ cm and $z = 0$ cm, respectively, and the step edge is at $x = 0$ cm. ....	52
Figure 4.5 Time-averaged vector fields generated by the vector magnitude averaging calculation method. (a) Without unit normalizing. (b) With unit normalizing. ....	55
Figure 4.6 Time-averaged contour plots generated by the vector magnitude averaging calculation method. (a) Without unit normalizing. (b) With unit normalizing. ....	56
Figure 4.7 An output contour plot from the percentage of images downstream averaging method. The bolts, missing tufts, and reattachment line are shown in the same way as with the magnitude averaging method. ....	57
Figure 5.1 A plot of the average unforced reattachment lengths for various step-height Reynolds numbers. As will be common practice from the remainder of this thesis, only data from the percent of images downstream calculation method is presented. ....	60
Figure 5.2 The effect of forcing amplitude on the reattachment length, for 2D forcing at our predicted optimal $St_h = 0.3$ . ....	63
Figure 5.3 The normalized reattachment length plotted as a function of the step height Strouhal number, for four values of 2D perturbation velocity at $Re_h = 24500$ . ....	64

Figure 5.4 A comparison between the 2D forcing results of Henning and King (2007), the 2D simulation results Kang and Choi (2002), and our 2D forcing at $u'/U_\infty = 0.35$ and $Re_h = 24500$ . .....	66
Figure 5.5 A comparison of the results obtained from the high ( $Re_h = 24500$ ) and low ( $Re_h = 12540$ ) 2D $X_R/X_{Ro}$ vs. $St_h$ experiments, forcing with $u'/U_\infty = 0.35$ .....	68
Figure 5.6 Time-averaged reduction in reattachment length plotted as a function of the step height Strouhal number. Three different 3D perturbation velocity curves ( $u'_{rms}/U_\infty = 0.1, 0.2,$ and $0.35$ ) are plotted for $Re_h = 24500$ .....	69
Figure 5.7 A comparison of the results obtained from the high ( $Re_h = 24500$ ) and low ( $Re_h = 12540$ ) 3D $X_R/X_{Ro}$ vs. $St_h$ experiments, forcing with $u'_{rms}/U_\infty = 0.35$ at $\lambda_z = 4h$ . .....	71
Figure 5.8 A comparison between the 2D and 3D forcing techniques, based on the results of the $X_R/X_{Ro}$ vs. $St_h$ experiment for $Re_h = 24500$ . (a) Perturbation amplitudes are 10% of $U_\infty$ (previous page). (b) Perturbation amplitudes are 20% of $U_\infty$ (previous page). (c) Perturbation amplitudes 35% of $U_\infty$ . .....	73
Figure 5.9 A comparison between the 2D and 3D forcing techniques, based on the results of the $X_R/X_{Ro}$ vs. $St_h$ experiment for $Re_h = 12450$ . Perturbation amplitudes are 35% of $U_\infty$ .....	74
Figure 5.10 The reattachment variation in the spanwise direction due to 2D forcing for selected experimental run characteristics. ....	75
Figure 5.11 The reattachment variation in the spanwise direction due to 3D forcing for selected experimental run characteristics. ....	76
Figure 5.12 Sample photographs from the dye visualization experiments at $Re_h = 12540$ . For photos with forcing, $St_h = 0.35$ and $u'/U_\infty = u'_{rms}/U_\infty = 0.35$ . (a) The unforced case. (b) Uniform spanwise (2D) forcing, with the wavelength of the natural 3D instability highlighted by a dashed white line. (c) Spanwise-varying (3D) forcing at $\lambda_z = 4h$ .....	78
Figure 5.13 Sample photographs from the dye visualization experiments at the transitional $Re_h = 2140$ . For photos with forcing, $St_h = 0.35$ with $u'$ and $u'_{rms} \gg U_\infty$ . Forcing profiles (not to scale) are presented in white. (a) The unforced case. (b) Uniform spanwise (2D) forcing. (c) Spanwise-varying (3D) forcing at $\lambda_z = 4h$ , with possible “chain-link fence” structures highlighted by white dotted lines.....	80

Figure 5.14 The projected suction-and-blowing actuation velocity profiles in the $x$ - $z$ (left) and $y$ - $z$ (right) planes are shown for one wavelength of actuation. The signs of vorticity generation are shown by the counterclockwise (for positive) and clockwise arrows (for negative). The step separation point is represented by a dashed line for both planes. ....	82
Figure 8.1 The calibration curves for the velocity testing with the backward-facing step in the water tunnel. Curves and equations are shown for both the inlet and downstream velocities and Reynolds numbers. ....	99
Figure 8.2 Spanwise variation of the reattachment lines for 2D forcing at $u'/U_\infty = 0.1$ , for $Re_h = 24500$ . ....	105
Figure 8.3 Spanwise variation of the reattachment lines for 2D forcing at $u'/U_\infty = 0.2$ , for $Re_h = 24500$ . ....	106
Figure 8.4 Spanwise variation of the reattachment lines for 2D forcing at $u'/U_\infty = 0.35$ , for $Re_h = 24500$ . ....	107
Figure 8.5 Spanwise variation of the reattachment lines for 2D forcing at $u'/U_\infty = 1.08$ , for $Re_h = 24500$ . ....	108
Figure 8.6 Spanwise variation of the reattachment lines for 2D forcing at $u'/U_\infty = 0.35$ , for $Re_h = 12540$ . ....	109
Figure 8.7 Spanwise variation of the reattachment lines for 3D forcing at $u'_{rms}/U_\infty = 0.1$ , for $Re_h = 24500$ . ....	110
Figure 8.8 Spanwise variation of the reattachment lines for 3D forcing at $u'_{rms}/U_\infty = 0.2$ , for $Re_h = 24500$ . ....	111
Figure 8.9 Spanwise variation of the reattachment lines for 3D forcing at $u'_{rms}/U_\infty = 0.35$ , for $Re_h = 24500$ . ....	112
Figure 8.10 Spanwise variation of the reattachment lines for 3D forcing at $u'_{rms}/U_\infty = 0.35$ , for $Re_h = 12540$ . ....	113
Figure 8.11 Normalized reattachment length vs. perturbation amplitude for 2D forcing at $St_h = 0.3$ , for the different $X_R$ calculation methods. ....	114

Figure 8.12 Normalized reattachment length vs. Strouhal number based on step height, for 2D forcing at $u'/U_\infty = 0.1$ and $Re_h = 24500$ . Results are plotted for the four different reattachment length calculation methods. ....	115
Figure 8.13 Normalized reattachment length vs. Strouhal number based on step height, for 2D forcing at $u'/U_\infty = 0.2$ and $Re_h = 24500$ . Results are plotted for the four different reattachment length calculation methods. ....	116
Figure 8.14 Normalized reattachment length vs. Strouhal number based on step height, for 2D forcing at $u'/U_\infty = 0.35$ and $Re_h = 24500$ . Results are plotted for the four different reattachment length calculation methods. ....	117
Figure 8.15 Normalized reattachment length vs. Strouhal number based on step height, for 2D forcing at $u'/U_\infty = 1.08$ and $Re_h = 24500$ . Results are plotted for the four different reattachment length calculation methods. ....	118
Figure 8.16 Normalized reattachment length vs. Strouhal number based on step height, for 2D forcing at $u'/U_\infty = 0.35$ and $Re_h = 12540$ . Results are plotted for the four different reattachment length calculation methods. ....	119
Figure 8.17 Normalized reattachment length vs. Strouhal number based on step height, for 3D forcing at $u'_{rms}/U_\infty = 0.1$ and $Re_h = 24500$ . Results are plotted for the four different reattachment length calculation methods. ....	120
Figure 8.18 Normalized reattachment length vs. Strouhal number based on step height, for 3D forcing at $u'_{rms}/U_\infty = 0.2$ and $Re_h = 24500$ . Results are plotted for the four different reattachment length calculation methods. ....	121
Figure 8.19 Normalized reattachment length vs. Strouhal number based on step height, for 3D forcing at $u'_{rms}/U_\infty = 0.35$ and $Re_h = 24500$ . Results are plotted for the four different reattachment length calculation methods. ....	122
Figure 8.20 Normalized reattachment length vs. Strouhal number based on step height, for 3D forcing at $u'_{rms}/U_\infty = 0.35$ and $Re_h = 12540$ . Results are plotted for the four different reattachment length calculation methods. ....	123
Figure 8.21 Important components and positions associated with the air bleed procedure.....	124
Figure 8.22 The TopLevelServoController.vi program front panel. ....	128

Figure 8.23 The main window for tuftImgProApp.m (accompanies instruction points I to IV in ReadMe.txt)..... 135

Figure 8.24 The vector field averaging window for tuftImgProApp.m (accompanies instruction points V and VI in ReadMe.txt)..... 136

Figure 8.25 Data from the test to determine the number of images that were required for time averaging of a single data point. The data point, randomly selected, corresponded to  $Re_h = 24500$ ,  $u^*/U_\infty = 1.08$ ,  $St_h = 0.3$  for 2D forcing. The average value of  $X_R/h$  was 3.988 over 150 images. .... 137

## Nomenclature

### Symbols

$AR$	Step Aspect Ratio
$AR_a$	Actuated Aspect Ratio
$A_v$	Servo peak angular velocity
$ER$	Geometric Expansion Ratio
$f$	Actuation frequency
$h$	Step height
$H$	Full height of the water tunnel test section
$H_i$	Inlet, or throat, height of the geometry
$n$	Spanwise forcing wave number
$r$	Radius of the pinion gear
$Re_h$	Reynolds number based on step height
$Re_\theta$	Reynolds number based on momentum thickness
$St_h$	Strouhal number based on step height
$St_\theta$	Strouhal number based on momentum thickness
$t$	Time variable
$u, v, w$	Streamwise, transverse, and spanwise component velocities
$u'$	Peak perturbation velocity/peak actuation slot exit velocity
$U_\infty$	Mean free stream velocity at the point of separation
$V_A(t)$	Tangential velocity of the rack and pinion force transmission system
$V_{A,peak}$	Peak tangential velocity

$W$	Step span, or width
$W_a$	Actuated span of the step
$w_a$	Width of a single actuation slot
$x, y, z$	Streamwise, transverse, and spanwise global coordinates
$X_R(z,t)$	Downstream reattachment location
$X_R$	Time averaged reattachment location
$X_{R0}$	Baseline time averaged reattachment location
$z_p(t)$	Time-varying spanwise phase
$\delta$	Boundary layer thickness
$\theta$	Boundary layer momentum thickness
$\lambda_z$	Spanwise wavelength of actuation
$\lambda_{z,o}$	Fundamental spanwise wavelength of actuation
$\nu$	Kinematic viscosity of water
$\omega_x, \omega_y, \omega_z$	Streamwise, transverse, and spanwise components of vorticity

## Abbreviations

BFS	Backward-Facing Step
ICV	Image Correlation Velocimetry
KH	Kelvin-Helmholtz
LDA	Laser Doppler Anemometry
LSS	Large-Scale Structures
LVDT	Linear Variable Differential Transformer
MEMS	Micro-Electro Mechanical Systems
PIV	Particle Image Velocimetry

QRP	Quasi-Random Phase
rms	Root Mean Square quantity
THD	Total Harmonic Distortion
VfDL	Vortex Fluid Dynamics Laboratory
2D	Two-Dimensional
3D	Three-Dimensional

# 1 Introduction

The related phenomena of separation and reattachment in turbulent fluid flows are prominent in many engineering applications; such as flow around buildings, over a stalled airfoil or compressor blade, in pipes with sudden expansions, or in combustion chambers; yet our comprehension of and ability to control these phenomena are somewhat limited. Even as this thesis was being written, French aerospace engineers at the Centre National d'Etudes Spatiales were studying the dynamic loading effects of the massive pressure fluctuations caused by these phenomena on the main nozzle of the Ariane 5 rocket (Marié and Lambaré, 2010). Thus far, various control schemes have been implemented by researchers in hopes of influencing turbulent separation over a vast number of bluff body geometries. A few of these methods have been implemented in practical applications (for example, the steady- or pulsed-blowing boundary layer control systems on the wings of Lockheed F-104 or MiG-21 fighter jets circa the late 1950s), although in most cases, current research on turbulent flow control is undertaken more to enhance the basic physical understanding of these flows (Greenblatt and Wygnanski, 2000). In short, much more work is needed before many of these control methods can be adapted to engineering applications. Choi et al. (2008) give a current review of many of these techniques, which can be classified into three main categories: passive control, active open-loop control, and active closed-loop control.

Passive control does not require continual energy input into the system, does not vary in time, and typically consists of some sort of structural modification to the surface of the bluff body; the boundary layer tripping cylinders of Isomoto and Honami (1989) provide a good example of this method.

Active open-loop control uses external energy input to apply a repetitive time-varying actuation, such as the periodic suction-and-blowing perturbations of a backward-facing step (BFS) flow by Hasan (1992). Active closed-loop control (more commonly known as feedback control) uses the response of the flow to continually modify the periodic perturbations, as in the studies of Henning and King (2007). For a bluff body that is considered two-dimensional (i.e. can be approximated as infinitely long in one coordinate direction), any of these control techniques can be spatially invariant ("2D") or can vary in space ("3D") over the bluff body.

## 1.1 Objectives

The research presented in this thesis had three main objectives. The first was to construct a device that would implement an active open-loop control scheme on a backward-facing step flow, based on the design and prototyping of a suction-and-blowing hydraulic actuator completed by Gilbert (2007). This robotically controlled actuation system was designed to be able to produce spanwise uniform and spanwise-varying forcing patterns that were periodic in time. These spanwise-varying forcing patterns were to be the physical manifestations of some of the numerical simulations of Kang and Choi (2002).

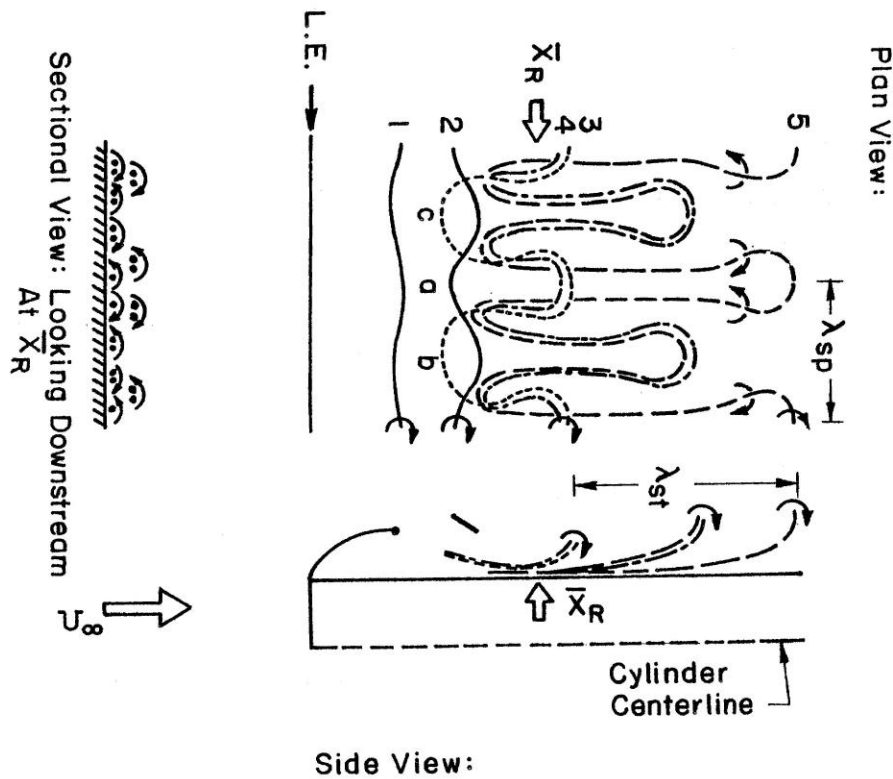


**Figure 1.1** The 3D vortex structures found in the reattaching shear layer for flow over a blunt-faced cylinder. Taken from Sigurdson [Bull. Am. Phys. Soc. 26, 1275 (1984)], and reproduced here with the express written consent of the author.

The second objective of this thesis was to make a comparison between two- and three-dimensional actuation techniques, and to ascertain whether or not 3D forcing was any more effective than 2D forcing in terms of the reduction in reattachment lengths that both techniques produced. 2D forcing is quite prominent in literature, but it has long been known that the vortical structures found in these flows (both immediately after separation and at reattachment) are strongly 3D in nature (Figure 1.1). This inherent three-dimensionality of the flow indicates that perhaps 3D forcing techniques would be more effective in reducing the

reattachment length than the customary 2D techniques. However, at present 3D experimental studies have not received as much attention as 2D studies; prior to our experiments, only Chun et al. (1999) and Henning and King (2007) had incorporated spanwise variations in forcing into their experimental studies.

We used two diagnostic techniques, discussed here and in the next paragraph. As a qualitative flow visualization tool, we aimed to use a dye insertion system to track the evolution of vorticity in the flow. This would allow us to examine the large-scale structures (LSS) present in the flow, and observe their interactions both with and without flow actuation.

Thirdly, in order to quantify our ability to control the flow, we aimed to develop a novel type of aqueous tuft to visualize the reattachment locations. An array of these tufts were developed, along with a tuft based image processing system which averaged multiple images of said array to obtain time-averaged flow-field information.

## **1.2 Thesis Outline**

This thesis has a literature review in Section 2. Previous work on the standard backward-facing step geometry is outlined briefly in Section 2.1, with a focus on the key parameters as they pertain to previous studies. We move on to discuss flow control methods tested on the backward-facing step in Section 2.2, with focus on previous numerical and experimental studies. We then discuss vorticity as it pertains to the backward-facing step geometry in Section 2.3, by examining the LSS that we would expect to see in our flow visualizations.

In Section 3 we present the details of our experimental apparatus; a robotically controlled backward-facing step that we have termed the “RoboStep”. The geometric characteristics of the RoboStep are presented in Section 3.2. Our actuation technology is discussed at length in Section 3.3, beginning with a summary of the prototyping work completed by Gilbert (2007) from Sections 3.3.1 to 3.3.3. We summarize the process of adapting the prototype into an array system (Sections 3.3.4 and 3.3.5), subsequently focusing on aspects such as power (3.3.6) and control (3.3.7) considerations. Section 3.4 provides details of the hydraulic system which connects the actuation array to the backward-facing step module inside the water tunnel. Section 3.4.1 summarizes the single-actuator hydraulic connection scheme proposed by Gilbert (2007), and Section 3.4.2 outlines the implementation of said proposed scheme into our current hydraulic configuration. Section 3.5 provides details of a separate system that introduces dye into the flow to track the evolution of vorticity.

Section 4 focuses on our method of experimentation, beginning with a discussion of the actuation characteristics (Section 4.2) as prescribed by Gilbert (2007). We then summarize the experiments that were undertaken for this thesis in Section 4.3. An unforced test for Reynolds number independence of the backward-facing step flow is outlined in Section 4.3.2. Sections 4.3.3 and 4.3.4 give details of our spanwise-invariant and spanwise-varying forcing experiments, respectively, which comprise the bulk of the data presented. We then review a brief series of dye visualization exercises in Section 4.3.5. After, we move to discuss our method of reattachment location measurement in Section 4.4. A detailed overview is given at the beginning of this section, and will not be included here.

Our results are presented and discussed at length in Section 5. The order in which they are presented is the same as the order in which they are outlined in Section 4.3, beginning with the unforced tests (Section 5.2) and moving on to the two- and 3D forcing experiments (Sections 5.3 and 5.4, respectively). Section 5.6 begins with sample photos from our dye visualization experiments in 5.6.1, and ends in 5.6.2 with a discussion of the effects of forcing from the standpoint of the LSS outlined in the literature review.

Our concluding remarks are contained in Section 6. We divide this section into two parts: Section 6.1 summarizes the key aspects of the thesis and draws major conclusions, while Section 6.2 looks ahead to possible future research involving the RoboStep. Proposed upgrades to our experimental apparatus are made in Section 6.2.1, while 6.2.2 suggests a sequence of possible future experiments, arranged in order of pertinence and feasibility.

## 2 Literature Review

### 2.1 The Backward-Facing Step (BFS)

Researchers have frequently used the geometry of a backward-facing step to study separation and reattachment. Contrary to other more complex geometries (e.g. airfoils or other three-dimensional shapes), the geometric simplicity of a backward-facing step flow ensures that the precise point of separation is known. In fact, the BFS represents the simplest 2D geometry which guarantees both separation and reattachment (Lai et al., 2002), thereby enabling straightforward comparisons to be made between studies with proper non-dimensionalization of key parameters. These parameters are:

The Reynolds number based on step height,  $Re_h = \frac{U_\infty h}{\nu}$

The Reynolds number based on momentum thickness,  $Re_\theta = \frac{U_\infty \theta}{\nu}$

The Strouhal number based on step height,  $St_h = \frac{fh}{U_\infty}$

The Strouhal number based on momentum thickness,  $St_\theta = \frac{f\theta}{U_\infty}$

The step aspect ratio,  $AR = \frac{W}{h}$

The geometric expansion ratio,  $ER = \frac{H}{(H-h)}$

The values of  $H$ ,  $h$ , and  $W$  are defined in Figure 2.1, which represents a standard depiction of a backward-facing step flow. Here, and in the rest of the thesis, we break from the left-to-right flow convention for reasons that will be explained later. The global coordinate system in the image applies to our flow geometry.

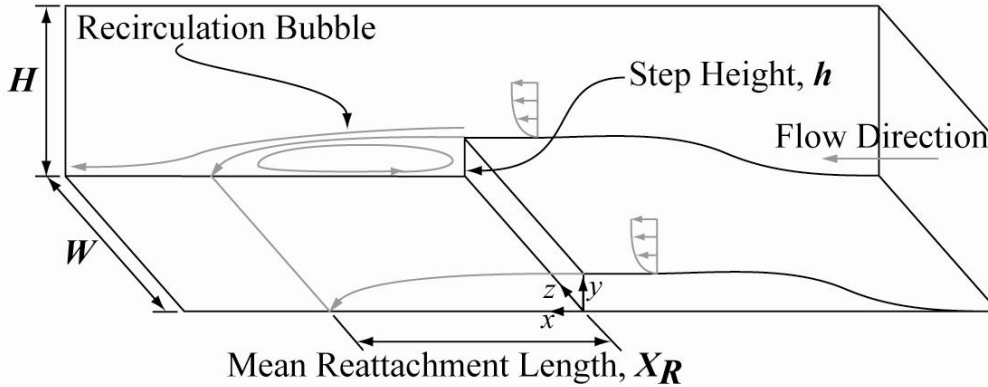


**Figure 2.1** A general schematic of an unforced backward-facing step flow. The coordinates are noted, and inlet and time-averaged flow qualities are represented in grey.

In backward-facing step geometries, flow separates at the edge of the step and reattaches to the wall at a distance  $X_R$  downstream of the step. This distance is known as the reattachment length, which bounds the region of the reattaching shear layer; a region which is also referred to as the “recirculation bubble” (Schäfer et al., 2009). Figure 2.1 depicts the time-averaged reattachment line as a spanwise-invariant, stationary line; however, it has long been known that the reattachment point fluctuates both in time (Adams et al., 1984; Le et al., 1997) and space (de Brederode and Bradshaw, 1972) in the spanwise direction. Lee and Sung (2002) suggested that these fluctuations, along with the periodic formation of LSS, accounted for the characteristic unsteadiness of the separation bubble. Lee and Sung (2002) also noted that the “flapping” frequencies were typically 6 to 8 times smaller than the vortex roll up frequencies in previous studies. The reattachment line, therefore, is better described as  $X_R(z,t)$ ; although for the remainder of this thesis we will focus on the time-averaged quantity  $X_R$ .

The BFS flow has been the subject of many studies (both with and without flow forcing) in the past; early experiments endeavored to document flow characteristics in the near-wall region at reattachment, and determine the relationships between these quantities and those of the boundary layer at separation. Adams and Johnston (1988a) made detailed near-wall pressure measurements and related them to turbulence quantities and boundary layer thickness  $\delta/h$  at the inlet. They then correlated the pressure and turbulence data to near-wall shear stress information, enabling them to draw conclusions about the reattachment lengths for laminar, transitional, and turbulent Reynolds numbers. They discovered that the maximum mean reattachment length for a laminar boundary layer was only 30% of that for a turbulent boundary layer (Adams and Johnston, 1988b). The vortex dynamics within the unforced backward-facing step geometry has also been investigated numerically by Schäfer et al. (2009) for laminar, transitional, and turbulent regimes.

For backward-facing step studies, the reattachment length (time-averaged or instantaneous) is generally accepted as the key parameter in describing the flow. To accurately measure this quantity, Mabey (1972) noted that the wall pressure fluctuations of a turbulent separation bubble achieve a clearly defined maximum just prior to the point of reattachment. Lee and Sung (2001) were able to verify that this result also held true for BFS geometries. In addition to the wall pressure fluctuations, researchers have used a wide variety of flow visualization techniques to measure the time-mean reattachment locations in backward-facing step flows. Standard time-averaged visualization methods have been implemented along the reattachment wall, such as the oil droplet techniques of Wengle et al. (2001) and Hasan (1992). In addition to surface oil techniques, Roos and Kegelmann (1986) used tufts to verify the two-dimensionality of their reattachment line. Laser-based photonic schemes have also been implemented; such as the adapted particle image velocimetry (PIV) techniques of Yoshioka et al. (2001a and 2001b) as well as the laser Doppler anemometry (LDA) technique of Armaly et al. (1983).

## **2.2 Previous BFS Flow Control**

In addition to the studies on the classical unforced configuration of the backward-facing step, various control methods have been implemented to influence the reattaching shear layer downstream of the BFS. These control methods were generally tested on their ability to reduce the size of the recirculation bubble; as reduction in reattachment length is associated with enhanced mixing in the reattaching shear layer through vortex interactions (Bhattacharjee et al., 1986), and also drag reduction experienced by the backward-facing step (Beaudoin et al., 2006).

The control techniques applied to this geometry have been varied, and can be classified into passive, active open-loop, and active closed-loop methods as outlined in Section 1.

It was previously mentioned that Isomoto and Honami (1989) used boundary layer-tripping cylinders to promote inlet turbulence intensity, thereby decreasing the reattachment length. Neumann and Wengle (2003) applied the same idea, instead using a structure that they termed a “control fence”. More recently, Park et al. (2007) have applied this idea to turbulent backward-facing step flows. They used small tabs on the step’s surface to create a counter-rotating vortex pair in the streamwise direction to enhance mixing in the reattaching shear layer. Although these examples of passive flow control on BFS geometries were successful in promoting some reduction of the reattachment lengths, they failed to produce  $X_R$  reductions as effectively as active control methods (Neumann & Wengle, 2003).

Active control techniques involve the continual addition of energy into the flow in the form of time-periodic actuation at a set (or possibly varying, for feedback control) frequency. In the literature, a debate exists concerning the appropriate dimensionless frequency to use for forcing:  $St_h$  or  $St_\theta$ . Hasan (1992) performed spectral analyses of velocity fields in reattaching shear layers downstream of a BFS for various perturbation frequencies. In so doing, he identified two distinct modes of instability: the “shear layer mode” corresponding to an optimal  $St_\theta = 0.012$  based on the momentum thickness of the boundary layer at separation, and the “step mode” which corresponded to the step height Strouhal number with an optimal value at  $St_h = 0.185$ . Hasan (1992) also demonstrated that the shear layer frequency eventually reduced to that of step mode via a multi-stage process of vortex merging of the LSS present in the shear layer.

These two spanwise instability modes were also studied by Sigurdson (1995), who referred to them as the well-known Kelvin-Helmholtz (KH) or “shear layer” instability, and proposed the presence of another “shedding” type of instability. The KH instability corresponded to that of the free shear layer, where the vorticity primarily interacted with itself. The shedding mode, on the other hand, was related to the interactions of shed vortices with their image vortices required in potential flow theory to account for the presence of the lower boundary. Sigurdson (1995) gave a comprehensive review of these two instabilities, as well as a discussion on periodic forcing for various flow geometries.

Bhattacharjee et al. (1986), Yoshioka et al. (2001b), Henning and King (2007), Kang and Choi (2002), and Roos and Kegelman (1986) all listed the step height Strouhal numbers of roughly 0.2 to 0.4 to be the optimal forcing frequencies which produced the maximum reduction in reattachment length. Conversely; Chun and Sung (1996), Wengle et al. (2001), and Kim et al. (2007) stated that the momentum thickness  $\theta$  (corresponding to the KH mode of instability) should be used as the scaling parameter.

In flow geometries where the algebraic radius of curvature is of opposite sign to the vorticity (such as the curved section of the BFS in Figure 2.1), there exists a third instability termed the “centrifugal instability” (Beaudoin et al., 2004). This instability, also called the Görtler instability, can occur in the form of streamwise pairs of counter-rotating vortices. 3D aspects of the flow over a backward-facing step are often attributed to this instability (Rani et al., 2007).

Numerous active flow control methods have been implemented on the backward-facing step geometry. Most involve some form of spanwise-invariant actuation applied periodically over time. “Flapping” type oscillations have been applied by Roos and Kegelman (1986) and Lai et al. (2002), with forcing displacement

amplitudes typically on the order of 1% of the momentum thickness at separation. Although neither of these studies attempted it, Gilbert (2007) suggested that arrays of actuators based on the micro-electro mechanical systems (MEMS) of Löfdahl (1999) could duplicate the 1% amplitudes of these studies.

Of all of the active control techniques applied to the BFS geometry, blowing-and-suction types of actuation are by far the most widely used in literature. Open-loop experimental studies of this type have been performed by Bhattacharjee et al. (1986), Hasan (1992), Chun and Sung (1996 and 1998), Chun et al. (1999), Wengle et al. (2001), Yoshioka et al. (2001a and 2001b), and Kim et al. (2007). Suction-and-blowing techniques have also been experimentally implemented in the feedback control experiments of Becker et al. (2005) and Henning and King (2007), who used the spike in wall pressure fluctuations as a rapid method for determining the reattachment point. Numerical simulations of blowing and suction forcing configurations have been explored by Choi (1999) and Kang and Choi (2002) to varying degrees of success.

As was previously mentioned, most of these active control schemes used spanwise-invariant forcing at a specific frequency to reduce the reattachment length. However, it is widely accepted that the LSS exhibit strongly 3D behaviour at reattachment, so it is somewhat intuitive to attempt to force these LSS with a spanwise-varying forcing pattern. Spanwise variations in forcing patterns are very rarely used in experimental studies and numerical simulations.

Chun et al. (1999) created spanwise variations in their forcing profile by covering some actuating sections of their 2D forcing rig, although they stated that doing so produced no additional reductions in the reattachment length. Henning and King (2007) resolved their spanwise forcing into four separate velocity types, and showed that the spanwise reattachment line varied according to the perturbation magnitudes across the span of the step.

In their numerical simulations, Kang and Choi (2002) discovered that they were able to implement an open-loop forcing pattern that produced the same reductions in reattachment as their suboptimal feedback control algorithm. Their open-loop forcing was modeled as a sine function in the spanwise direction:

$$\phi(z,t) = A_o \sin \left[ \frac{2\pi}{L_z} (z + z_p(t)) \right] \quad (2.1)$$

Where  $\phi(z,t)$  denoted the actuation at a specific point,  $A_o$  was 10% of the free stream velocity,  $L_z$  denoted the spanwise wavelength of actuation, and  $z$  and  $z_p(t)$  were the initial phase offset and time-varying phase quantity. Their optimal

spanwise wavelength of actuation was  $L_z = 4h$ ; and they tested time-varying phase quantities of zero phase velocity, a constant phase velocity in  $z$ , and a quasi-randomly generated phase velocity. The symbols for the parameters provided in this paragraph are taken verbatim from Kang and Choi (2002); it should be noted that these symbols are not necessarily adopted for the remainder of this thesis (only those found in the nomenclature section are adopted).

## 2.3 Vorticity and the BFS

In this section we outline the various vortical structures commonly observed in the wake of a BFS flow. These structures are formed by the interaction of the vorticity contained in the boundary layer at separation with several instability modes that correspond to the formation of different vortex structures. All of the passive and active flow control techniques summarized in the previous section aimed to influence these vortices in one way or another; enhanced mixing and reduction in reattachment length are correlated to increased vortex interactions such as pairing.

### 2.3.1 Spanwise and Sidewall Vortices

Perhaps the most readily identifiable (but by no means the simplest) vortical structures that are present in backward-facing step flows are the spanwise vortices. These are the LSS that are primarily discussed in 2D step studies, but recent research by Sheu and Rani (2006) indicated that these structures exhibit 3D behaviour immediately after forming. Sigurdson and Roshko (1984) and Sigurdson (1986) had also observed this phenomenon for a blunt-faced plate (Figure 1.1).

Sheu and Rani (2006) hypothesized that after flow separation occurred at the step edge, a natural “roll-up” process corresponding to the KH instability instantly resulted in the formation of a spanwise vortex. The same shedding type instability proposed by Sigurdson (1995) was credited with the subsequent 3D evolution of the original KH vortices. The evolution developed as follows: The original KH vortices would undergo tilting and stretching to form lambda shaped vortices in the  $x$ - $z$  plane, which would then “impinge” on the step wall and elongate into hairpin-like vortices. As usual, the ends of the hairpin vortices would curl up from self-induction due to curvature.

It was also inferred that the shedding instability (which was induced by the KH vortices interacting with their images from the bounding walls) was responsible for the periodic variation of the reattachment length. Sheu and Rani (2006) termed this the “flapping” behaviour of the recirculation region (the same flapping

behaviour outlined in the previous section), and noted that it occurred with the formation of vertical sidewall vortices. Sidewall-related vortical interactions to produce vertical sidewall vortices were also observed by Armaly et al. (1983) and Williams and Baker (1997), but neither provided any insight into the exact generation mechanism of the structures.

It should be noted that the simulations conducted by Sheu and Rani (2006) were for flows at transitional Reynolds numbers ( $Re_h = 900 \sim 2000$ ); whether or not any of the aforementioned vortical structures appeared in our fully turbulent flows will be discussed in Section 5.6. The same is true for types of vortices outlined in the following two subsections.

### **2.3.2 Corner Vortices**

During their simulations, Rani et al. (2007) confirmed the presence of what they called a “corner vortex” immediately downstream of the backward-facing step on the lower boundary surface. This vortex was present only at sufficiently high Reynolds numbers ( $Re_h \geq 2000$ ), and formed as a result of the positive pressure gradient along the reattachment wall immediately downstream of the BFS. Kang and Choi (2002) observed a similar structure for turbulent Reynolds numbers ( $Re_h = 5100$ ), which they termed a “secondary recirculation bubble”.

### **2.3.3 Taylor-Görtler Vortices**

It was previously mentioned that there exists a region of Görtler instability in some backward-facing step flows, which can lead to the formation of longitudinal (streamwise) counter-rotating vortex pairs often called Taylor-Görtler vortices. Beaudoin et al. (2004) tested for the formation of these vortices downstream of a backward-facing step for various step heights. They observed mushroom-like structures that indicated the presence of said streamwise vortices. They verified that these vortices occurred in the presence of centrifugal instability by confirming that the criteria of the Rayleigh discriminant and the Görtler number were met. These streamwise vortices are very similar to the interlocking hairpin vortices (Figure 1.1) observed by Sigurdson and Roshko (1984) and Sigurdson (1986).

It is interesting to note that Beaudoin et al. (2004) observed these structures only for the largest expansion ratio ( $ER$ ) of 1.11, but over the entire range of Reynolds numbers ( $Re_h = 10 - 300$ ) that they tested. The absence of a threshold for this phenomenon indicates that these vortices could be present in turbulent backward-facing step flows, provided that the  $ER$  is large enough.

Rani et al. (2007) also observed what they termed “Taylor-Görtler-like” vortices, although their location was limited to a secondary recirculation on the upper boundary surface. They called this secondary region the “roof eddy”, and noted that its existence was much more unstable than the KH recirculation region. Yanase et al. (2001) also visualized streamwise vortices that they called “rib structures”; the formation of these vortices was also attributed to Görtler instability.

## 3 Experimental Apparatus

### 3.1 Overview

This section provides a detailed description of our experimental setup through component-specific sections. The apparatus is located in the High-Speed Water Tunnel Laboratory in the Mechanical Engineering Building at the University of Alberta. First, the backward-facing step itself is discussed in Section 3.2. Section 3.3 gives a complete account of the actuators, beginning with a summary of the work done by Stuart Gilbert on the prototype in 3.3.2. Section 3.3.5 gives details of how we adapted the prototype actuator to become part of a complete actuation system, including the power and logic grid connections. Section 3.4 outlines the hydraulic system which connects the actuators to the backward-facing step. Finally, the design and construction of a dye injection system for flow visualization is discussed in Section 3.5. It should be noted that an important part of our apparatus, the ‘tuft plate’, is not described in this section. This piece of equipment is presented in Section 4.4.2.3, as it is an integral part of our image processing system. Detailed engineered drawings of the step and actuator components are provided by Gilbert (2007) in his thesis, and are not included here.

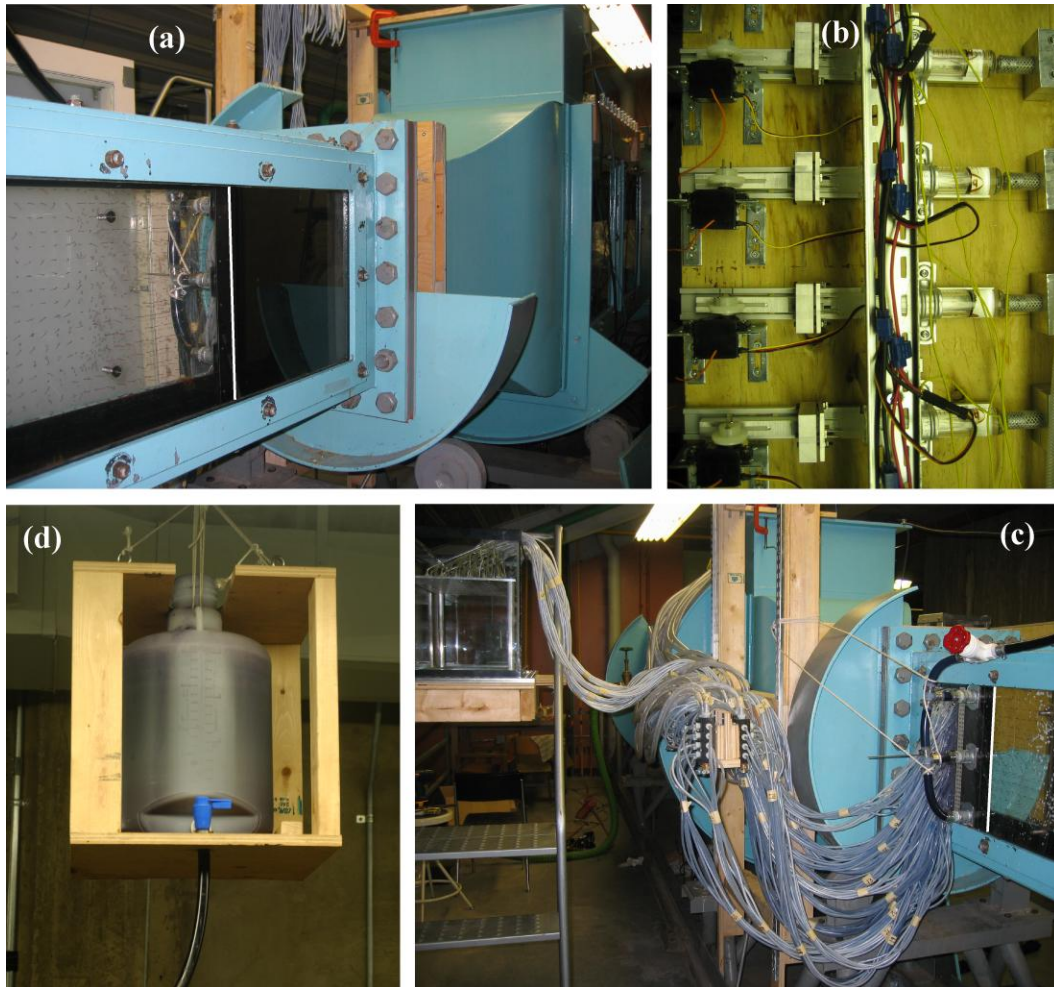
Figure 3.1 is included here to provide the reader with an initial sense of the experimental setup. Each photograph in the figure corresponds to a subsection of this apparatus section.

Figure 3.1 (a) shows the vertical orientation of the anodized black backward-facing step module (Section 3.2) in the water tunnel, with its separation edge highlighted by a white line. Flow is right to left, viewing from the front of the water tunnel.

Figure 3.1 (b) shows 4 of our 22 total actuators, which consist of servo-driven syringes that can produce periodic suction-and-blowing actuation of various waveforms (Section 3.3).

Figure 3.1 (c) shows our hydraulic system (Section 3.4), as viewed from the back of the water tunnel. The step’s separation edge is again highlighted in white, as in Figure 3.1 (a). Figure 3.1 (c) illustrates how the main actuation lines originate from the actuators on top of the water tunnel, with each main actuation line connecting to a distribution manifold that divides the flow into 8 equal branches. Each of these 8 branches connects to either a single actuation port (out of a total of 128) located across the span of the step along its separation edge, or to a

separate back pressure reservoir; the back pressure reservoir is the tank on the left side of Figure 3.1 (c).



**Figure 3.1** An overview of various components of the experimental apparatus. (a) The black, anodized backward-facing step module situated vertically in the test section of the water tunnel, looking from the front of the test section. The separation edge of the step is shown in white, and flow is right to left. (b) Four individual actuators from our actuator array. (c) The system of hydraulic connections, looking from behind the test section. Actuation flow comes from the actuator array on the top of the water, into the distribution manifolds, and then out of the ports at the separation edge of the backward-facing step (again denoted by a white line, flow left to right this time). (d) The storage reservoir for the dye that is used in flow visualization experiments.

Finally, Figure 3.1 (d) displays our dye reservoir, which we use to store dye that will be injected into the flow from a slit directly underneath the actuation ports. The dye is then entrained by the LSS during separation at the step's edge, which allows us to visualize the propagation of the LSS downstream on the step. The dye tube emanating from the bottom of the reservoir in Figure 3.1 (d) is the same tube as the one on the right side of Figure 3.1 (c) connecting into the BFS. As was previously mentioned, the dye injection system is explained further in Section 3.5.

### 3.2 The “RoboStep”

Although we generally use the term “RoboStep” to refer to our entire apparatus, in this section (3.2 only) we also use the term interchangeably to refer to the backward-facing step module that is inserted into the water tunnel’s test section. Figure 3.2 illustrates the key differences between the RoboStep and the classical unforced backward-facing step geometry (Figure 2.1). Figure 3.2 is not drawn to scale, although the shape of the BFS is consistent with that of the actual RoboStep. The inset of Figure 3.2 was adapted from a Solidworks wireframe screen image of the RoboStep, and is included to illustrate the relative locations of the actuation ports and the dye injection slit. Note that the flow is forced at an angle of  $45^\circ$  relative to the free stream, in keeping with the experiments of Chun and Sung (1996) and Henning and King (2007). The same global coordinates shown in Figure 2.1 should be assumed for Figure 3.2, although they are not shown in Figure 3.2.

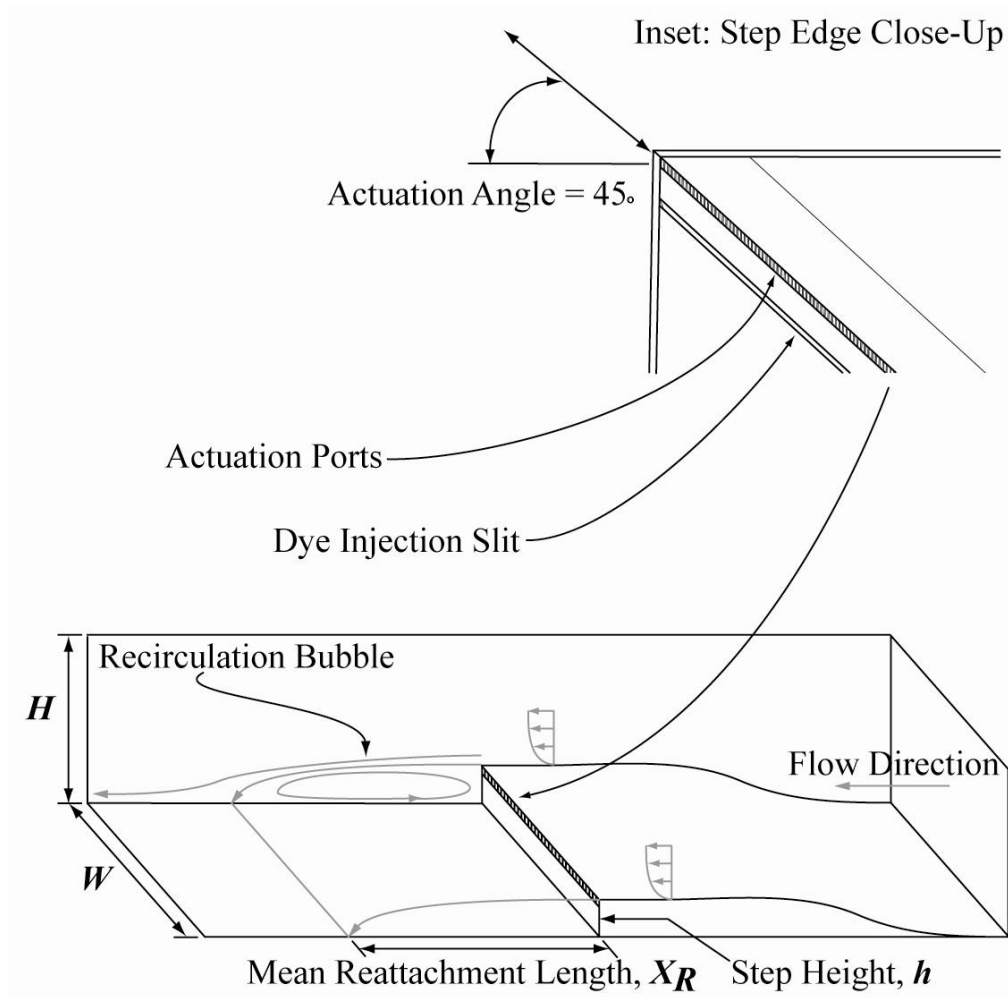


Figure 3.2 A representation of the RoboStep geometry, with key lengths and features noted. Inset: The locations of the dye injection slit and the actuation ports relative to the separation edge of the backward-facing step. The global coordinates are identical to those shown in Figure 2.1.

Below, in Table 3.1, we list the some pertinent values and experimental parameters for our BFS geometry. The original values, as reported by Gilbert (2007), are included in the Original Value column. Due to the insertion of a flow visualization apparatus called the tuft plate (Section 4.4.2.3) downstream of the RoboStep, many of the Gilbert's (2007) original values had to be modified to account for the 1/8 inch thickness of the plate. These values are reported in the Adjusted Value column.

**Table 3.1** Some pertinent backward-facing step and test section experimental parameters. Original values are shown in the second column, while effective values (which account for the thickness of the tuft plate when it is in place) are displayed in the third column.

Parameter	Original Value	Adjusted Value
Effective Step Height, $h$ (cm)	5.54	5.23
Step Width, $W$ (cm)	45.72	45.72
Aspect Ratio, $AR = W/h$	8.25	8.75
Actuated Span With, $W_a$ (cm)	44.45	44.45
Actuation Aspect Ratio, $AR_a = W_a/h$	8.02	8.51
Test Section Height, $H$ (cm)	25.4	25.08
Inflow Section Height, $H_i = H - h$ (cm)	19.86	19.86
Expansion Ratio, $ER = H/H_i$	1.28	1.26

Taking into account the thickness of the tuft plate, the RoboStep has an effective height  $h = \text{original step height} - \text{tuft plate thickness} = 5.23$  cm. The step spans the entire width  $W = 45.72$  cm of the water tunnel test section. Due to the configuration of the water tunnel, this width corresponds to the vertical dimension in Figure 3.4, as evidenced by the rotation in coordinate systems between Figure 2.1 and Figure 3.4. These values of effective step height and width give an adjusted aspect ratio  $AR = W/h = 8.75$ . This is slightly lower than widely accepted value of  $AR = 10$  (de Brederode and Bradshaw, 1972) necessary for a BFS flow to be considered fully 2D. As such, any unexpected 3D flow characteristics contained in our results could be in part explained by this fact. The full height of the test section after the expansion (Figure 3.2),  $H$ , is 25.08 cm when the width of the tuft plate is taken into account. Again, note that  $H$  corresponds to the horizontal depth dimension in Figure 3.4, due to the  $90^\circ$  rotation of the  $y - z$  coordinate plane about the  $x$  axis. These dimensions give an adjusted expansion ratio of  $ER = H/H_i = 1.26$ , where  $H_i$  is the inflow, or ‘throat’, test section height ( $H_i = H - h$ ).

We refer to the RoboStep module as the machined BFS that is inserted into the test section of the water tunnel; however, the RoboStep module itself is composed of three modular components (Figure 3.3). Figure 3.3 (b) displays an exploded view of the three RoboStep modules, with (1) entitled the dye reservoir, (2) the actuation slots, and (3) the main portion of the BFS as per Gilbert (2007).

The dye module, shown in Figure 3.3 (b) as component (1), is the part of the step that seals against the inner wall of the water tunnel’s test section. A thin (3/16 inch thick) sheet of soft rubber gasketing was inserted between the BFS and the test section wall, with the appropriate gasket hole pattern to allow fastening screws, actuation tubes, and dye to pass through. The dye is introduced into the module as outlined in Section 3.5; once in the module, the dye emanates from a thin slot that is formed between parts (1) and (2) provided that there is sufficient

head to push the dye into the free stream. The width of the dye slot ( $\sim 0.4$  mm) can be adjusted via 6 set screws along the base of the dye module, although this must be done before the RoboStep is sealed in the test section. This feature was a modification made by the author, and came about indirectly due to some initial leakage problems. During the initial testing of the RoboStep's seals, existing gaskets within part (2) and between parts (2) and (3) failed due to the pressure difference between the interior and exterior of the test section during tunnel operation. It was determined that the original gasket adhesive was unable to withstand this pressure difference; partly because the adhesive's resistance to applied shear stresses was insufficient, and also because there was not enough sealing pressure applied to secure the internal gaskets in the original RoboStep configuration. This problem was remedied by using a stronger adhesive, and by introducing the aforementioned 6 set screws to apply pressure to the sealing plates of the internal gaskets. Applying increased pressure to the sealing plates also increases size of the dye injection slit.

The actuator module is shown as part (2) in Figure 3.3 (b). This is the component of the RoboStep that enables the hydraulic connections between the actuation ports at the step's edge and the tubes situated outside the test section. These connections will be explained in detail in Section 3.4; for now, it should be mentioned that the connections between the smallest diameter tubes and the RoboStep actuation slots (2) are made through the rectangular slot in the base of part (1) in Figure 3.3 (b). It should also be note that the actuator slot could conceivably be used by itself as a forcing mechanism for other flow geometries (Gilbert, 2007).

The main step module of the RoboStep is shown by part (3) in Figure 3.3 (b). This section was machined from a single piece of aluminum, and was designed to ensure that flow separation would not occur until the BFS edge (Gilbert, 2007). The profile of this module in the  $x - y$  plane is comprised of three sections: a fillet, an ellipse, and a flat section. The fillet begins at the leading edge of the step, and continues until it smoothly joins an elliptical section where the profile changes curvature. This 3:1 ellipse then joins a flat section which is  $2h$  in length. The slope of the step module profile does not exceed the maximum slope of the contraction between the settling tank and the test section at any point. The detailed criteria and design processes for the fillet and elliptical sections are given by Gilbert (2007) in his master's thesis.

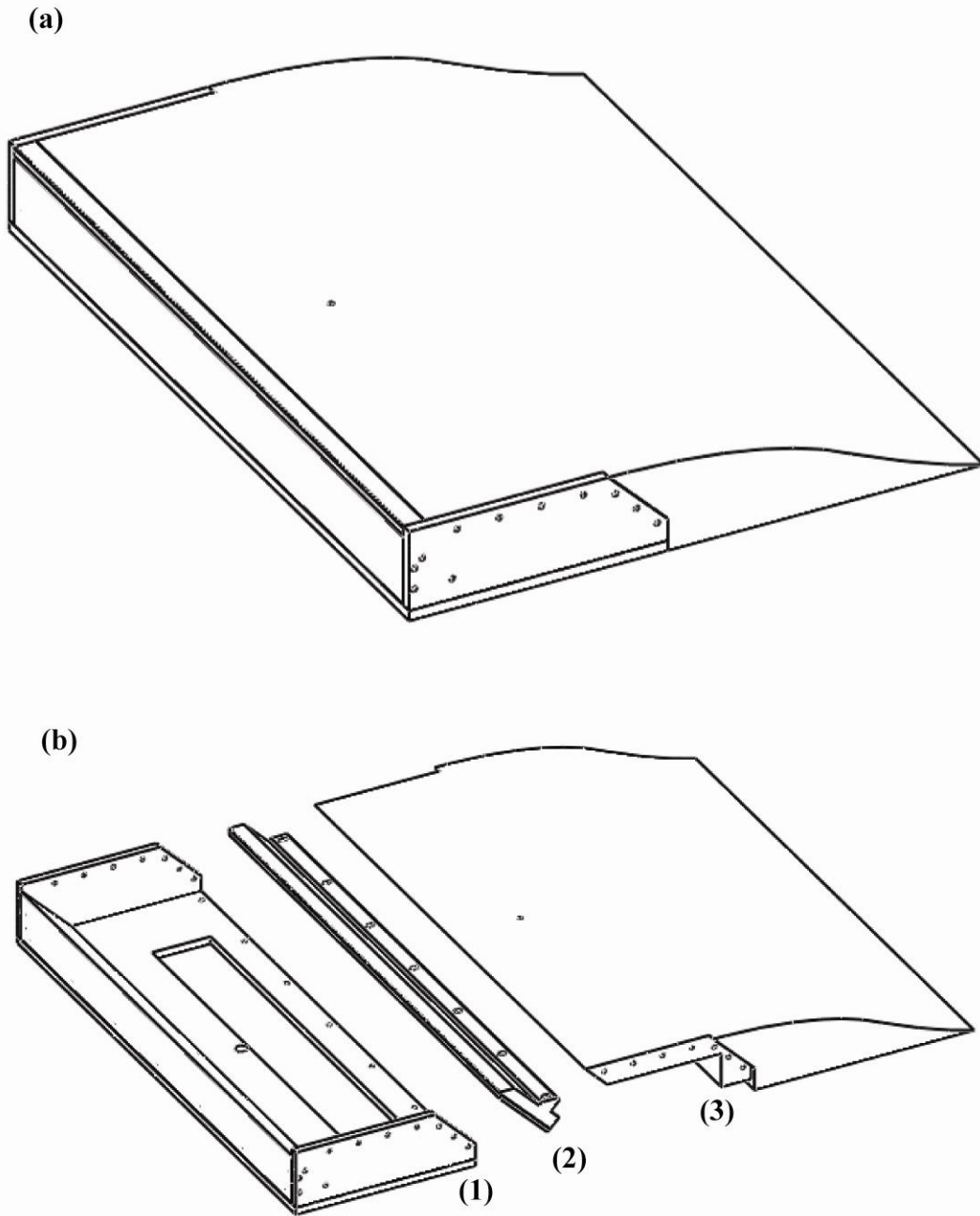


**Figure 3.3** The RoboStep module. (a) A fully assembled view. (b) An exploded view, showing the dye module (1), the actuator module (2), and the step module (3).

In Section 2.1, we noted that the boundary layer quantities  $\delta/h$  and  $\theta$  at the point of separation were identified as key parameters by several BFS studies. In order to measure these quantities, the RoboStep can be upgraded to include a hydrogen bubble wire for flow visualization with the fabrication of an additional fitting. The fitting would have to be constructed out of a non-conductive material in order to electrically isolate the RoboStep from the hydrogen bubble wire electrically-

floating circuit. When in place, the hydrogen bubble wire would be normal to the flat surface of the RoboStep, and would pass through the hole shown in Figure 3.3 (a) and through the test section windows as well. The clearance hole through the RoboStep is located 1.3 step heights upstream of the separation edge. This upgrade would allow employment of the image correlation velocimetry (ICV) techniques developed by Apps (2001) and Apps et al. (2003) to calculate  $\delta/h$  and  $\theta$  using images of the hydrogen bubbles.

Figure 3.4 is included here to illustrate the vertical orientation of the RoboStep in the water tunnel. The global  $x$ ,  $y$ , and  $z$  coordinates are the same as those in Figure 2.1, rotated  $90^\circ$  about the  $x$  axis. This image provides a view from in front of the water tunnel, which is also the location from which we collected our raw data image files. Due to this fact, the flow direction ( $U_\infty$  in Figure 3.4) in all of our raw images is right-to-left. This was an oversight in the development of our image processing software (explained later in Section 4.4.4), which operates assuming this flow direction convention. For this reason, we break the left-to-right flow direction convention throughout this thesis.

The backward-facing step module is represented by (1) in Figure 3.4, with the global coordinates and separation edge highlighted as in previous images. The water tunnel's test section (2) and settling tank (3) are also labeled for future reference.

The entire RoboStep module was anodized black, as shown in Figure 3.4. This hardened the leading edge of filleted section of the RoboStep, which was extremely thin and would have otherwise been prone to denting and chipping. The anodization process also protected against corrosion, and minimized light reflection from the BFS surface during image capturing and flow visualization. Incidentally, the entire inner wall of the test section was repainted with a flat black marine epoxy for much the same reason, and also because severe corrosion problems had to be remedied before the step insertion could occur.

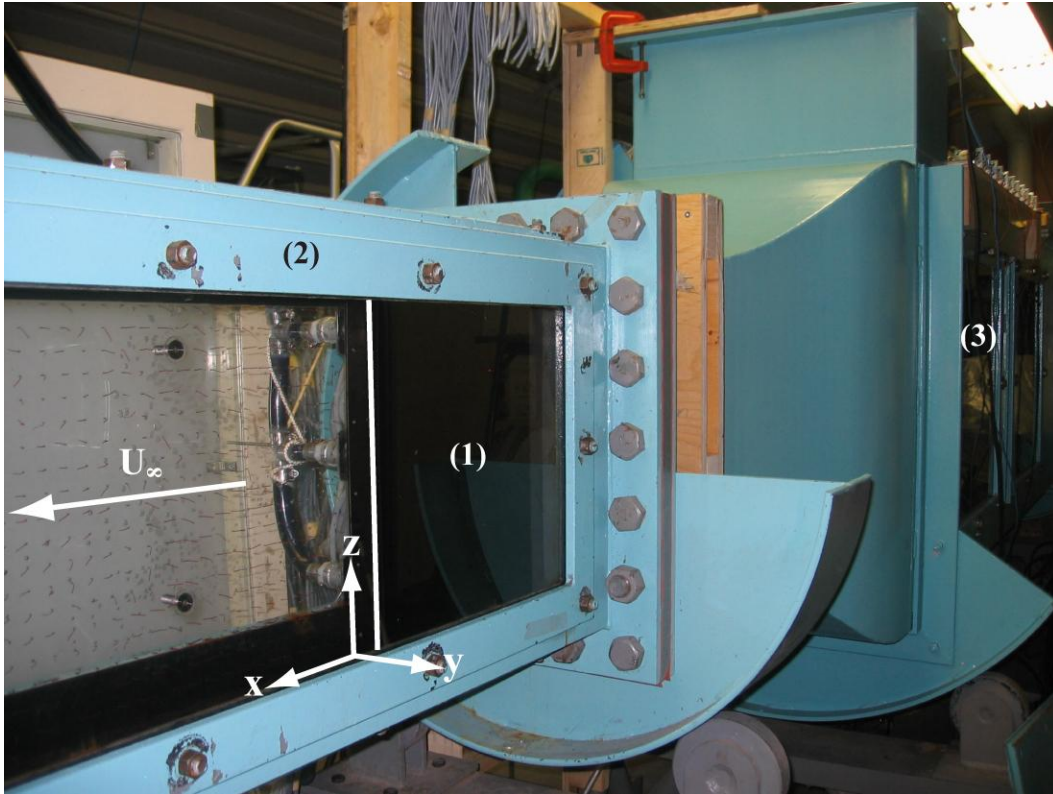


**Figure 3.4** A photograph of the vertical orientation of the backward-facing step (1) in the water tunnel test section (2). The settling tank is labeled as component (3), and the global coordinates are shown. Flow direction  $U_\infty$  is indicated, and as before, the separation edge of the RoboStep is indicated by a white line.

One additional upgrade to the RoboStep, made by the author, is shown in Figure 3.5 below. Due to slight non-uniformities in the water tunnel's cross sectional area, there was a gap of approximately 1 cm between the leading edge of the step and the water tunnel wall. A small extension of corrosion resistant 0.01 inch thick sheet metal was fastened to the underside of the leading edge as a joiner between the leading edge and the test section wall. This extension was effective in bridging the gap, and was made to match the radius of curvature of the sheet metal bend to that of the polynomial fillet section on the RoboStep. Figure 3.5 provides a sectioned-view representation of this component. The thin gauge sheet metal was held in place by 6 metal screws evenly spaced over the span of the RoboStep's underside, with holes set approximately 1 inch downstream of the leading edge. The joints between the sheet metal and the RoboStep module, and also between the sheet metal and the settling tank wall, were smoothed using vacuum grease. Figure 3.5 also shows the placement of the flange joint between the settling tank and test section of the water tunnel, which the gap-bridging connector also extends across.

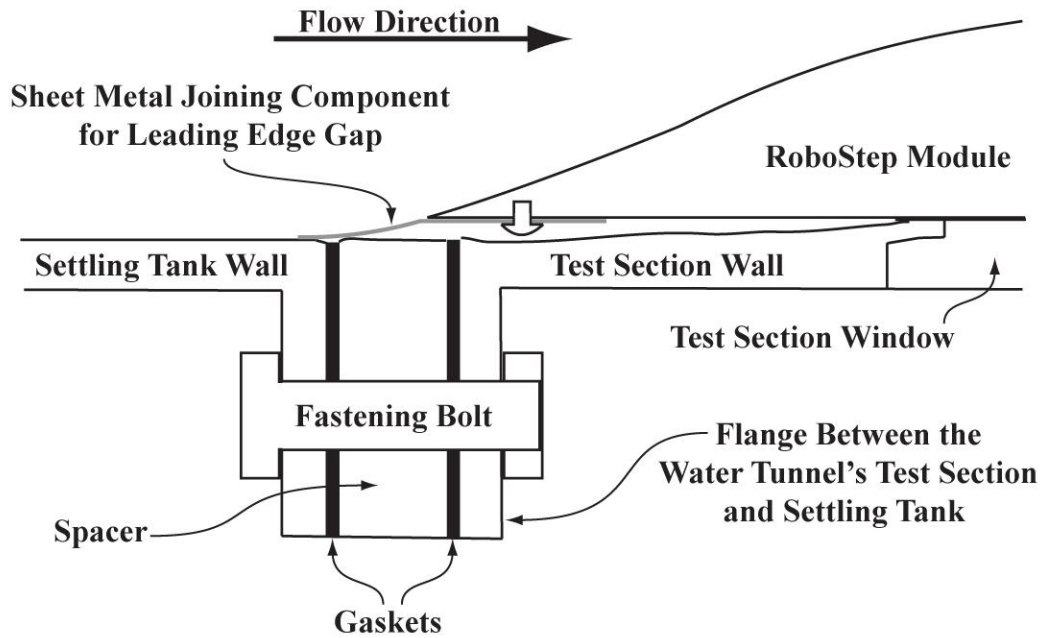


Figure 3.5 A section view sketch of the leading edge gap-bridging connector (shown in grey), and its associated fastening screws. The connector also extends over the flange joint at the connection of the settling tank and test section of the water tunnel.

### 3.3 The Gilbert Prototype Actuator (2007)

#### 3.3.1 Technology Selection Review

In order to select a suitable actuation technique, Gilbert (2007) considered all of the actuation techniques outlined in the literature review. However, due to the fact that water had already been selected as the working fluid, several types of actuators were eliminated based on that criterion: MEMS actuators, plasma actuators, actuators with piezoelectric components, and shape memory actuators. MEMS actuators were rejected because of the inevitable oxidation of silicon components in water, while actuators containing piezoelectric materials were not considered because of the relatively high voltages needed to operate them. In addition, piezoelectric actuators generally operated at frequencies too high to be useful for our experiments. Plasma actuators would not be able to create electric winds in water, and the temperature variations of the Edmonton's water supply due to the changing of the seasons would be problematic for shape memory actuators. The operating frequencies of shape memory actuators were also deemed too low to produce our desired  $St_h$  range. As a result, Gilbert (2007) elected to focus on flapping and blowing-and-suction techniques.

After narrowing the possible actuation technologies down to flapping and blowing-and-suction, Gilbert (2007) scored each technology in a decision matrix

that rated them on quality of actuation, operational ease, and fabrication concerns. He found that suction-and-blowing configurations tended to score higher in the areas of operation and fabrication, due to the fact that flapping actuators were more difficult to manufacture and offered fewer possibilities for upgrades. As a compromise between fabrication cost and quality of actuation, Gilbert (2007) chose to use blowing-and-suction type actuators along with 8-branch distribution manifolds to hydraulically force the 128 actuation ports across the span of the step.

### **3.3.2 The Selected Prototype**

Figure 3.6 shows four of the 22 array actuators that the author constructed based on the specifications of the prototype produced by Gilbert (2007). These actuators were nearly identical to the prototype produced by Gilbert (2007), save for a few modifications that are outlined later in Section 3.3.4.

Components (1) and (2) in Figure 3.6 illustrate the rack-and-pinion force transmission system that we use to actuate the flow. The servos are high performance HS-225MG analog servos from Hitec Incorporated. Gilbert (2007) noted that these servos performed well enough during his single prototype testing that a higher quality digital servo was deemed unnecessary. Had the digital servos been selected (at approximately twice the cost of the analog servos), they would have been able to force at higher amplitudes and frequencies while temporally resolving periodic waveforms more accurately. This point will become more important when discussing possible future experiments in Section 6.2.2. Each servo drives a pinion gear over a maximum possible rotation of  $60^\circ$ . The one inch pitch diameter pinion gears in turn drive the racks, which are labeled (2) in Figure 3.6 and are mounted atop low friction sliders.

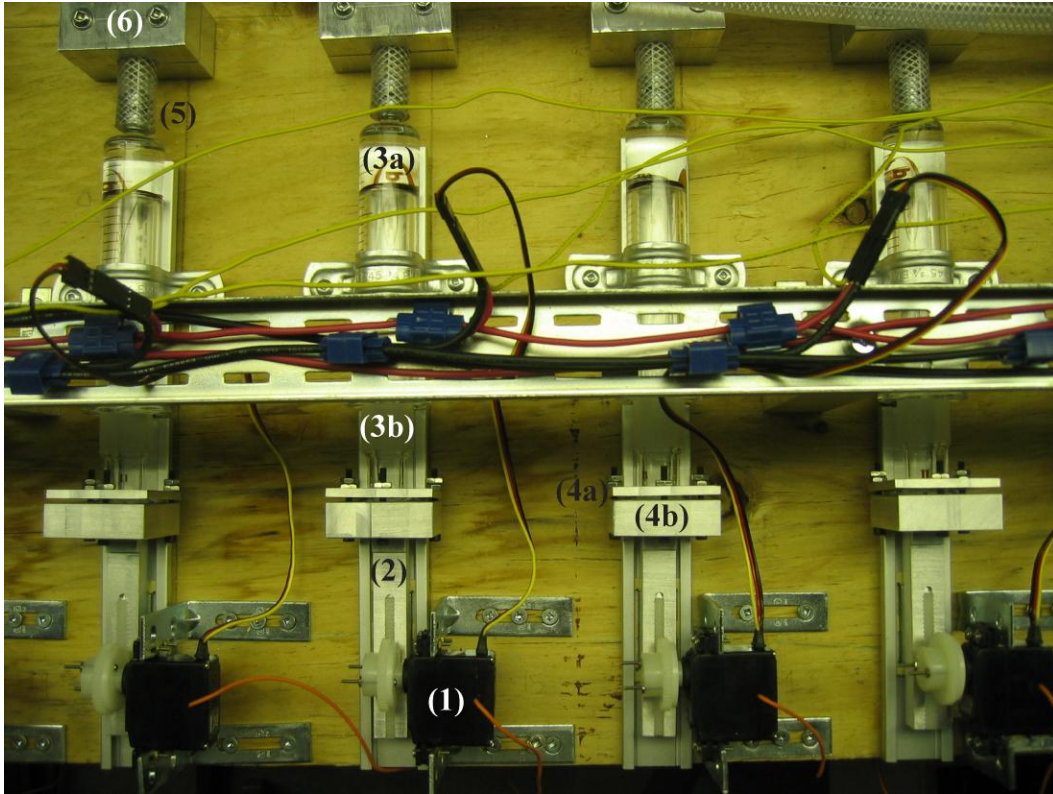


**Figure 3.6** Four array actuators constructed from the prototype specifications of Gilbert (2007). The pinion gears attached to the servo motors (1) drive the racks (2), which are connected to the syringe plungers (3b) via the syringe housing (4b) and plate (4a) systems. At the end of each syringe (3a), there is a luer lock fitting (5) which is press fit into a 3/8 inch inner diameter reinforced hose. The hoses are held in place by rectangular tube clamps (6).

We use 20 mL, low friction syringes (3a) from Popper and Sons in our actuators. At the end of each rack, a housing block (4b) and face plate (4a) holds the syringe plunger (3b) in place while it actuates back and forth (forcing water into and out of the syringe) at the tangential velocity of the pinion gear. The plunger diameters of the syringes are 1.958 cm. At the end of each syringe there is a luer lock fitting (5), onto which we press fit a 3/8 inch inner diameter reinforced hose to begin the system of hydraulic connections outlined in Section 3.4. These hoses are held in place by rectangular tube clamps (6) which are explained in Section 3.3.4.

Because the slider and syringe were mounted on different support structures, we developed a special tool which ensured that the syringes and the rack-and-pinion systems were perfectly aligned with one another. This alignment guaranteed that there were no radial forces exerted on the syringe casing by its plunger, which eliminated binding of the syringes during operation.

### 3.3.3 Initial Performance Testing

Following his successful construction of a prototype actuator, Gilbert (2007) tested the prototype's ability to reproduce sinusoidal time-varying forcing waveforms. He sampled data directly from the servo's potentiometer using an ad hoc wire connection that the potentiometer was not explicitly designed for, and performed a harmonic analysis on the acquired signals to characterize the servo's performance. In terms of frequency response, the actuator forced to within 10% of the desired frequency values over the entire range of frequencies tested (0 to 6 Hz). At frequencies below 3.5 Hz, the error in frequency was reduced to almost nothing. The measured peak actuation velocities agreed with the desired values to within 8%, although only up until forcing frequencies of roughly 2.5 Hz. For frequencies greater than 2.5 Hz, the actuator's performance worsened until it reached a maximum error in peak velocity of 20% when forcing at 6 Hz. The total harmonic distortion (THD) of the signal was also calculated as a means of determining the noisiness of the servo signals. The lowest value of THD that was obtained during prototype testing was 5% at 0.5 Hz, which increased to values of 35% to 40% when forcing between 4.5 and 6 Hz.

In light of these results, Gilbert (2007) concluded that a conservative upper bound for high-quality forcing was 3 Hz, with the best quality forcing occurring for frequencies below 1.5 Hz. Based on the optimal step and shear layer mode Strouhal numbers ( $St_\theta \approx 0.012$  and  $St_h \approx 0.19$ , respectively), suggested by Hasan (1992) and estimated from the results of Sigurdson (1995), Gilbert (2007) calculated maximum possible Reynolds numbers of  $Re_\theta = 16750$  and  $Re_h = 46100$  when the actuator was operating at 3 Hz.

### 3.3.4 Alterations Made to the Prototype

It was discovered fairly quickly that the actuators had several inherent flaws that made them prone to problems with long term usage. Although Gilbert (2007) was able to construct a prototype actuator that performed successfully during testing, he tested the prototype only for a short period of time and needed to make multiple adjustments before success was achieved. This constant need for tuning was a fairly substantial problem, especially considering an array of 22 actuators rather than a single prototype.

The continual need for tuning arose in part from the servos' tendency to rattle during operation. The housing and faceplate combination (Figure 3.6) which held the plunger to the force transmission rack was the principle area in which this was a problem. In order to prevent binding of the servos, the three faceplate nuts could only be finger-tight; this avoided the creation of radial forces on the plunger

which led to the binding problems. As a result, the nuts tended to loosen over time owing to the vibrations of the plunder head in its housing. As a solution to this problem, a second nut was added to each of the faceplate bolts to serve as a locking mechanism. In order to lessen the overall vibration experienced by each actuator, a hard rubber gasket was placed in the housing at the rack/plunger interface. This was an upgrade that proved effective in damping the vibrations.

Even with the aforementioned upgrades, binding within the syringes between the plunger and cylinder still occurred (albeit infrequently). It was discovered that this was a result of the tube clamps that held each syringe to its alignment rail (Figure 3.6). Even under light tightening these tube clamps provided forces sufficient to cause radial deformations of the outer cylinder of the syringe, thereby causing the syringe to bind. Fortunately, it was discovered that the syringes would stay in position without the use of the tube clamps. Therefore, all syringe-holding tube clamps were either loosened off or removed completely.

In order to purge the air bubbles from the hydraulic lines, the author developed an air bleed procedure that is outlined in Appendix C1. The air bleed procedure must be performed for every manifold pair in the system whenever the test section is emptied, or in any situation that causes bubbles to form in the hydraulic lines. A complete system bubble purge typically takes 4 hours, although more than one iteration of the procedure may be necessary. This procedure involves moving the actuator array vertically over a distance of roughly 2 m. Because the press fit connections between the luer lock syringe heads and the 3/8 inch reinforced tubes (Figure 3.6) were extremely tight, large amounts of radial or axial stresses applied to the tubes would cause the syringe heads to snap off rather than the tubes to be pulled off. As a result, a rectangular tube clamp (Figure 3.6) was designed to hold the tubes (and consequently, the syringes) and absorb any stresses that would otherwise be experienced by the luer lock fitting on the syringe.

After the data pertaining to this thesis was collected, a detailed characterization of the servos' performance was undertaken by Mr. Marc Schostek – a follow-on M.Sc. student with the Vortex Fluid Dynamics Lab. His calibration (Appendix G3) indicated that further improvements to the servos were necessary; some of which have already been implemented. These changes are outlined in Section 6.2.1.

### **3.3.5 The Actuator Board**

As was previously mentioned, we configured our 22 actuators in an array on a 3/4 inch thick plywood board. The actuators were spaced approximately 4 inches apart, in order to allow for the installation of additional components such as

LVDTs. During water tunnel operation, this board was situated on the top of the water tunnel's settling tank, with the free surface in the snorkel of the water tunnel at the same elevation as the centerline of the syringes. The snorkel of the water tunnel is labeled (1) in Figure 3.7, and is a small (1 ft by 2 ft) opening that represents the only free surface in the entire high-speed water tunnel loop.

Figure 3.7 shows the actuator board in its operating position on top of the water tunnel settling tank, looking down toward the test section of the water tunnel. The servo controller card (Section 3.3.7) is shown on its elevated post (2) in the immediate foreground of the image; the rail system (3) which elevates the individual servo power connections (Section 3.3.6) is also labeled. Point (4) shows the positioning in which an LVDT can be connected to a given servo for this actuator spacing configuration.

The servo controller card and power connections were elevated because of the perpetual presence of wetness on the surface of the board. Syringe leakage during movement of the actuator board and spilled water during the air bleed procedure were the most significant contributing factors to the wetness problem; realizing that these factors would never be completely solved, we opted instead to elevate any component with electrical connections (Figure 3.7).

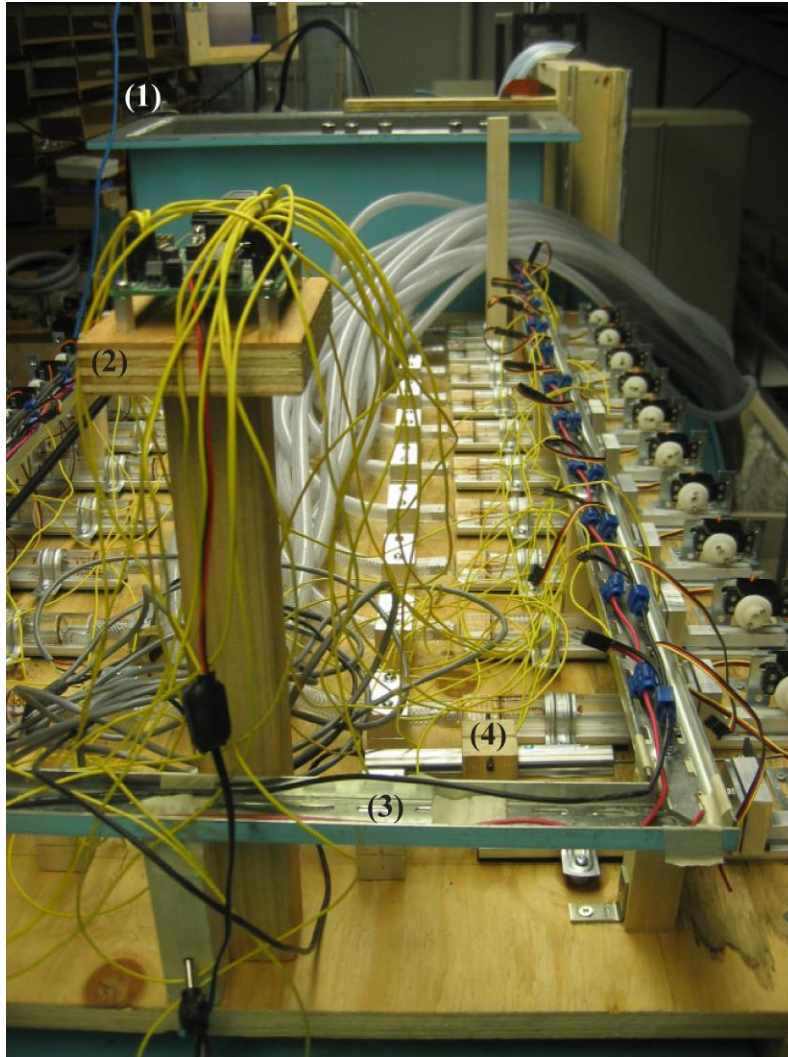


**Figure 3.7** The overview of the actuator board situated on top of the water tunnel's settling tank, looking down toward the test section. Point (1) denotes the water tunnel's snorkel, (2) shows the elevated structure for the servo controller card, (3) labels the rail which supports the power wires, and (4) labels an LVDT mounted to the bottom-right servo as used by Marc Schostek in his calibrations (Appendices G1 and G3).

### **3.3.6 Power Connections**

Figure 3.8 displays the same photograph as Figure 3.6, this time with key components of the servos' power and logic grid connections highlighted. The servo motors are powered by a Kepco JQE 6-22M DC box power supply (not shown), which provides between 4.8 and 6 V (the allowable operating voltage range of our servos) at up to 22 amperes. The power supply connects to the larger diameter positive (1a) and negative (1b) wires that encircle the actuator board on the elevated rail system (Figure 3.7).

From Figure 3.8, we see that each individual servo is connected into the main power lines using a crimp terminal connection (2), with main line branches for each servo being created by T-connectors (1a) and (1b). This creates a large parallel circuit, with each servo motor as a separate loop. Wires (3) and (4) will be explained in the following section.

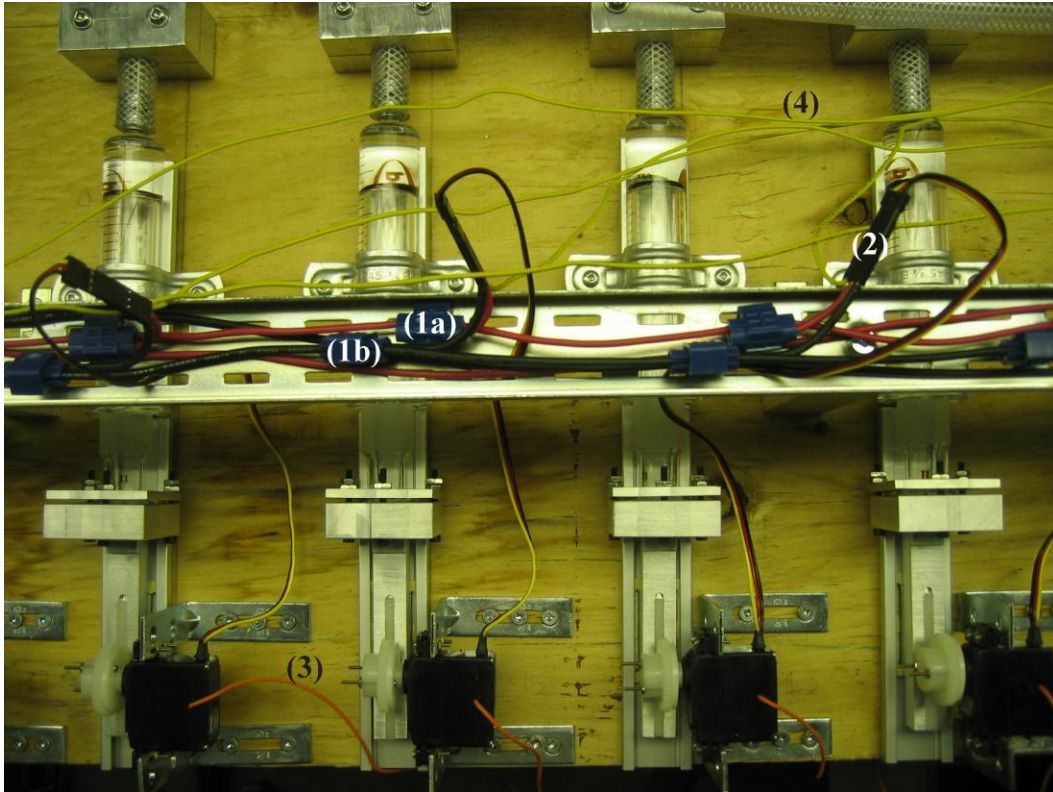


**Figure 3.8** The power and logic connections for the servos. The large positive (1a) and negative (1b) wires are connected to a power supply providing 6 VDC. Each individual servo has a crimp terminal connection (2) that connects to the main lines using T-connectors (1a) and (1b). Wires (3) and (4) represent the servo potentiometer and servo signal wires, respectively (Section 3.3.7).

It was noted that when operating the servos at DC voltages approaching the maximum of 6 V, the servos would begin to flutter and overheat if left idling for too long. For this reason, a safe working voltage of no more than 5.5 VDC was maintained during testing. A diode was also installed into the circuit between the positive power supply terminal and the main wire. This prevented the accidental application of reversed voltage-polarity to the circuit, which would have destroyed the internal circuitry of the servos.

### 3.3.7 Actuator Control

Control of the actuation system was achieved using a LabVIEW program which sent formatted ASCII text strings to the Lynxmotion SSC-32 servo controller

card, which converted the text strings into pulse width signals using its internal firmware. These text strings were formatted in LabVIEW, and were discretizations of various sinusoidal waveforms sent over a 9-pin serial cable. The complete LabVIEW control program was designed and coded by the author in conjunction with Mr. David Breakey, who was an NSERC funded Undergraduate Summer Research Assistant in 2009. A more detailed explanation of the function of the LabVIEW program is provided in Appendix D1. The servos sampled the pulse width signals at 50 Hz, which is termed the “servo refresh rate” by Hitec Incorporated. Servo movement for one of our analog servos was based on a feedback loop, where a given servo would calculate the difference between its current position and the applied pulse width signal.

The actuators are numbered according to which channel slot they occupy on the servo controller card, from 0 to 21. These numbers also correspond to the channel numbers outlined in the LabVIEW control program (Appendix D1). In Figure 3.7, the servos on the right-hand side are even numbered (i.e. 0, 2, 4, etc. up to 20 numbering from foreground to background) and the servos on the left are odd numbered (i.e. 1, 3, 5, etc. up to 21 numbering again from the front to the back of the figure).

Figure 3.7 shows the location of the SSC-32 servo controller card (2) with respect to the actuator array. The small wires inserted into the screw terminals on the controller card are its power supply wires, as it is on a circuit that is isolated from the servo power to protect against surges. An AC to DC converter providing 8 VDC was used to power the SSC-32 card. Figure 3.8 illustrates how the pulse width wires (4) from the servo controller card connect to each individual servo through its associated crimp terminal.

The wires labeled (3) in Figure 3.8 were manually soldered onto the servos’ potentiometers in an attempt to extract performance data from the servos. These wires were connected to a National Instruments USB-6229 data acquisition box. However, after we observed unexpected voltage outputs and unusual signal noise in the acquired potentiometer signals, we concluded that we could not be sure of the data that this technique provided. The details of the internal workings of the servos and their feedback algorithms are kept proprietary by the servo manufacturer. For this reason, no data was acquired from the potentiometer wires during experimentation and they were left disconnected. In the future, however, these wires could be used to measure phase differences between different servos.

## 3.4 Hydraulic Connections

### 3.4.1 Actuator-to-RoboStep Connection Overview

In this section we outline the tubing network of hydraulic lines that connect the actuators to the actuation module of our backward-facing step. The single-actuator hydraulic connections are the same as those proposed by Gilbert (2007); the adaptation of these connections into a complete system, the establishment of system component locations, and the design and construction of the associated support structures were undertaken by the author. Figure 3.9 (a) shows the complete system of hydraulic lines (as viewed from behind the water tunnel test section), while Figure 3.9 (b) shows a close up of several of the distribution manifolds.

For a given actuator, the hydraulic connection system begins with the press fit connection between the reinforced 3/8 inch inner diameter tubing and the luer lock fitting on the syringe, as shown in Figure 3.6. The reinforced tubing is labeled as component (4) in Figure 3.9 (b), with each tube covering a distance of 243.8 cm where they connect to the barbed fittings of the manifolds. The distribution manifolds (5) are commercially available, and split the flow from the actuators into 8 branches of 1/8 inner diameter tubing sections. These tubes are indicated by the (6) label in Figure 3.9 (b), and are 121.9 cm in length. The 1/8 inch tubes are then connected to diameter-reducing barbed fittings at location (7) in Figure 3.9 (b). These reducing fittings were originally designed to be embedded in the test section window and held in place by a sealing plate (Gilbert, 2007) to seal off the RoboStep module. However, it was determined that the RoboStep module remained watertight without the seal plate in place, so these connections were left in the configuration of Figure 3.9 (a). The fittings at location (7) in Figure 3.9 (b) reduce the inner tubing diameter from 1/8 inch to 3/32 inch. The 3/32 inch tubes are 30.5 cm long, and pass through holes in the test section window as well as the rectangular slot in the bottom of the BFS (Figure 3.3). These tubes are press fit onto stainless steel fittings which connect directly to the 3.81 cm long actuation slots of the RoboStep. The actuation slots are rectangular, with areas of approximately 2.5 mm by 1 mm.

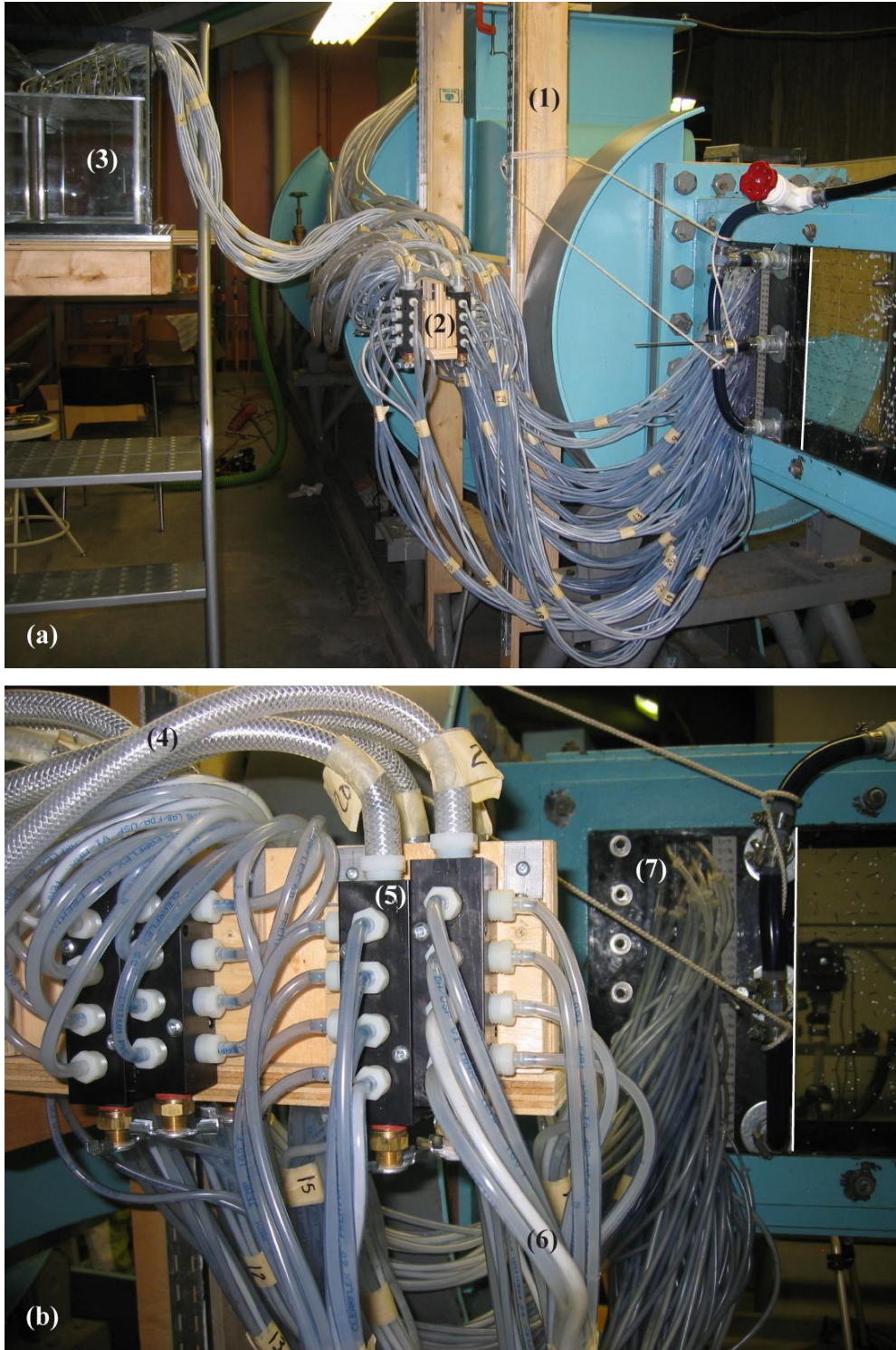


**Figure 3.9** The hydraulic connection system for the RoboStep. (a) An overview of the hydraulic system, looking from the behind the water tunnel. The manifold support frame (1), height-adjustable manifold rack (2), and additional tube reservoir (3) are highlighted. (b) A close up photograph of two manifold pairs (5), with the three major tube diameters noted (4), (6), and (7). In both images, the separation edges of the RoboStep are highlighted by white lines.

Figure 3.9 (a) indicates that manifold tubes can either connect to actuation ports through a series of reducing fittings, or they can be routed into an additional back pressure reservoir (3) that is necessary for various non-symmetric spanwise wavelengths of forcing (outlined later in Section 4.2.2). It should be noted that both routes of tubing were designed to be fluid dynamically similar; i.e. the same friction and fitting losses are associated with each path. The back pressure reservoir was designed by the author, and complies with the criteria for fluid dynamic similarity as given by Gilbert (2007). The back pressure reservoir consists of an isolated 2.67 ft<sup>3</sup> capacity glass tank, elevated to a level that allows the free surface of the reservoir to equal that of the water tunnel. Tubes from the manifolds to the reservoir undergo the same diameter reduction sequence as the manifold-to-RoboStep tubes. The reservoir-tube connections are made with barbed fittings that are anchored to an aluminum frame which holds the tubes in place below the reservoir's free surface.

In his thesis, Gilbert (2007) tabulates and presents complete length and diameter values for all of the components in the hydraulic system, including tubing, fittings, and slots.

### **3.4.2 Experimental Connections**

The hydraulic connections we made were for a spanwise wavelength of  $4h$ ; the concept of spanwise wavelength will be explained in greater detail in Section 4.2.2. For now it is sufficient to note that at this specific spanwise wavelength, for our resolution of 8 velocity types per wavelength, adjacent actuation ports force at the same perturbation amplitudes in groups of 8. Also, because our spanwise wavelength can be symmetrically resolved about the span for our total desired number of forcing groups (16), we only need 16 of the 22 actuators to produce this wavelength (16 actuators x 8 adjacent ports/actuator = 128 total ports).

This meant that we were able to disconnect actuators 0 to 5, connecting only actuators 6 to 21 to the RoboStep. Because a single actuator controls a single 8-branch distribution manifold, a given manifold (and therefore a given actuator) would force a single velocity type (i.e. 8 adjacent actuation ports). The 8 manifold branch tubes were connected at random within the velocity type, meaning that adjacent branches on the manifolds were not necessarily connected to adjacent actuation ports. Table 3.2 lists which actuation slots are controlled by each individual actuator. The actuators are numbered according to the system outlined in Section 3.3.7, and the actuation slots are numbered starting at 1 from the top of the test section ( $z = 45.72$  cm) to the bottom ( $z = 0$ ). For this wavelength, the additional tube reservoir (Figure 3.9) was also not needed, and so no manifold connections were made to it; i.e. actuators 0 to 5 were completely disconnected

(hydraulically and electrically), and were not operated during the experiments outlined in this thesis.

**Table 3.2** The hydraulic actuation slots that each actuator is connected to. Actuators are numbered according to Section 3.3.7, and actuation slots are numbered starting at 1 from the top of the test section ( $z = 45.72$  cm) to the bottom ( $z = 0$ ).

Actuator Number	Actuation Slots Controlled
6	1 – 8
7	9 – 16
8	17 – 24
9	25 – 32
10	33 – 40
11	41 – 48
12	49 – 56
13	57 – 64
14	65 – 72
15	73 – 80
16	81 – 88
17	89 – 96
18	97 – 104
19	105 – 112
20	113 – 120
21	121 – 128

### 3.5 Dye Injection System

In order to perform the dye visualization exercises outlined in Section 4.3.5, we required a large reservoir to house the dye that we would be injecting into the flow. We designed the reservoir with fine and coarse levels of dye flow control in order to ensure that we would be able to properly adjust the amount of dye that was introduced into the test section. Parts of the dye reservoir were constructed by Mr. Dory Parsonage who worked with the Vortex Fluid Dynamics Lab (VfDL) in 2008. Dory Parsonage began his VfDL tenure with a spring undergraduate Dean’s Research Award project on tuft material selection (Section 4.4.2.2), which continued the following summer on an NSERC Research Scholarship.

Figure 3.10 illustrates the dye reservoir and its corresponding support frame. To provide the reader with a frame of reference for the location of this reservoir, note that it can be seen in the top left-hand corner of the actuator board image (Figure 3.7). The dye reservoir frame is supported by three ropes which are connected to a wall-mounted cable winch system at location (1), which allows the reservoir to be raised or lowered as desired. The possible range of motion extends from floor level (if the dye in the reservoir is to be diluted with water from the test section),

to approximately 1.5 m above the top of the test section (for maximum dye expulsion head).

This variability in height is what provided the coarse adjustment setting for the dye flow rate, as slight changes in the height of the reservoir produced large changes in dye flow rate. For a given set of visualization experiments, the elevation of the dye reservoir was typically held constant until a substantial amount of dye had leaked into the tunnel.



**Figure 3.10** The dye reservoir, and dye reservoir support frame. The frame connects to a cable winch at location (1), and the flow can be controlled by the valve at (2).

Figure 3.10 also shows a control valve (2) which was used largely as a redundant flow control method when the dye reservoir was not in operation. During experiments, it was completely opened and flow control was achieved using the fine adjustment method discussed presently. When visualization experiments were not occurring and the dye reservoir was being used as a storage unit, this

valve was closed; although not completely necessary, we felt that this provided an added measure of safety in case of catastrophic failure of the other valve.

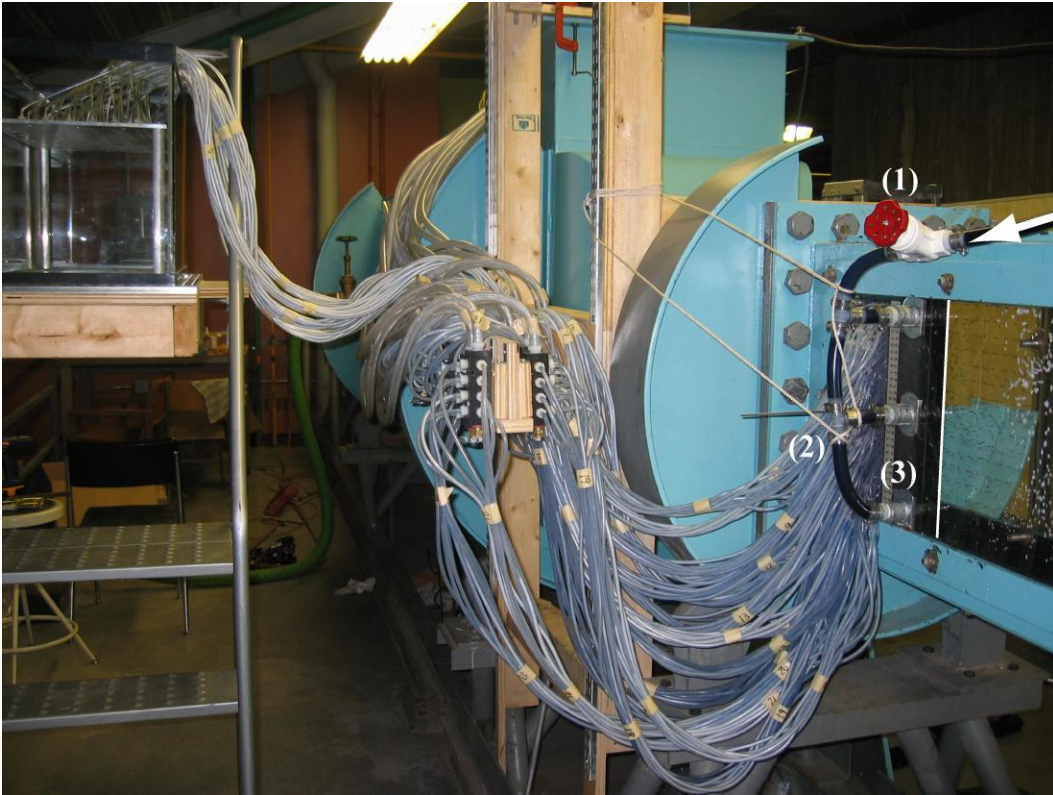


**Figure 3.11** The dye injection system, as it connects into the back of the RoboStep module (viewed from behind the test section). The inflow direction is indicated by the white arrow. The gate valve, dye manifold, and port holes are labeled by (1), (2), and (3), respectively. The separation edge of the BFS is highlighted with a white line.

Figure 3.11 illustrates how the dye is fed through the back of the test section window into the RoboStep’s dye reservoir module. The inflow arrow on the right-hand side of the image corresponds to the same 5/8 inch line labeled “To RoboStep Module” in Figure 3.10. The gate valve is labeled as part (1) in Figure 3.11, which allows fine adjustments to be made to the dye flow rate. Part (2) in Figure 3.11 shows the distribution manifold, which supplies the inflow dye to the RoboStep’s dye module through 3 entrance ports at location (3). The manifold hoses are connected using barbed fittings, with all barbed fitting connections secured by hose clamps. Once the dye is supplied to the RoboStep, it emanates from a thin slit 6 mm below the separation edge of the of the BFS (the separation edge is highlighted by the white line in Figure 3.11)

## 4 Methodology

### 4.1 Overview

This section outlines the method of experimentation, focusing on three major areas: a characterization of our forcing technique, a complete account of the initial experiments undertaken for this thesis, and our method for measuring the reattachment location. We begin with a discussion of the capabilities of the actuators in Section 4.2; focusing on forcing amplitudes in Section 4.2.1, and then possible spanwise-varying forcing wavelengths in Section 4.2.2.

We present the overviews for the following sections at the beginning of each associated section, i.e. the overview for Section 4.3 is contained in Section 4.3.1, and the overview for 4.4 is in 4.4.1. This is done because the concepts presented in these sections are not closely related to those in 4.2, and also because the large number of subsections in 4.3 and 4.4 may be confusing without a fresh idea of the section order in the reader's mind.

### 4.2 Actuation Characteristics

#### 4.2.1 Forcing Amplitudes

Our actuators are designed to produce single frequency actuations (in time) of the following form (as described by Gilbert, 2007):

$$V_A(t) = V_{A,peak} \cos(2\pi ft) \quad (4.1)$$

Where  $V_A(t)$  denotes the time-varying tangential velocity of the rack and pinion system. The peak tangential velocity is defined as  $V_{A,peak} = rA_v$ ;  $A_v$  is the peak angular velocity of the pinion, which is calculated by multiplying the amplitude and frequency of angular oscillations. Gilbert (2007) then used the tangential velocity relation  $V_{A,peak} = rA_v$  to simplify equation 4.1 to:

$$V_A(t) = rA_v \cos(2\pi ft) \quad (4.2)$$

Knowing the value of the pinion gear's radius (1/2 inch), and having an estimate for the maximum peak angular velocity (which was obtained during his prototype testing), Gilbert (2007) was able to estimate a maximum value for the actuation velocity of the syringe (5.54 cm/s). Using the conservation of mass between the syringe area and the combined areas of 8 actuation ports (which a given syringe controlled), Gilbert (2007) calculated that the ideal actuation slot exit velocity  $u'$  would be 83.5 cm/s. He then calculated that in order to keep actuation frequencies

below his maximum desirable forcing frequency of 3 Hz, our range of operational Reynolds numbers would be between  $7000 \leq Re_h \leq 46100$ .

In practice, this ideal slot exit velocity value was never reached, as the servos were rarely running at their maximum possible speeds. Typical peak actuation slot velocities for normal operating (moderate amplitudes at around 3 Hz forcing) were usually on the order of 15 ~ 20 cm/s, not 83 cm/s (Appendix G2). These slot exit velocities (and any other actuation velocities mentioned in Appendix G) were estimated using LVDT-output syringe plunger velocities; as of yet, no direct measure of the actual port exit velocities had been attempted. It would be useful to perform this calibration before any additional experiments, although the ports appear to be perturbing the flow well enough to produce results that are comparable to other studies.

#### 4.2.2 Spanwise Wavelengths

The most unique characteristic of our actuation system is the wide range of spanwise waveforms that we are able to produce. An actuation waveform does not necessarily have to follow a sinusoidal spatial spanwise distribution; it can be any waveform that can be resolved into 8 or 16 different velocity types across the span of the RoboStep (Gilbert, 2007).

Gilbert (2007) provides a detailed explanation of the possible sinusoidal spanwise wavelengths  $\lambda_z$  in his thesis. He denotes the shortest possible wavelength of  $0.5h$   $\lambda_{z,o}$ . For this wavelength, there are 16 complete sine waves across the span of the step, and each actuation slot (with width  $w_a \approx 3.5$  mm) forces at a different velocity type (with 8 velocity types comprising a wavelength). A visual representation of the velocity type concept is shown in Figure 4.1, where each step in the solid black line represents a different velocity type. This value of  $\lambda_{z,o}$  represents the “fundamental wavelength” (Gilbert, 2007) of any wavelength which can be resolved into 8 velocity types.

Gilbert (2007) also outlines a method for calculating the discretized spanwise velocities based on the midpoint equation, where each velocity level  $i$  is calculated using:

$$V_A(z, t) = \sin\left(\frac{2\pi}{\lambda_z} \left[ \frac{z + z_{i+1}}{2} + z_p(t) \right]\right) \text{ For } i = 1, 2, 3 \dots 8 \quad (4.3)$$

Where  $z = w_a \times [0 \ n \ 2n \ 3n \ 4n \ 5n \ 6n \ 7n \ 8n]$ , and  $n$  denotes the wave number  $\lambda_z/\lambda_{z,o}$ ; alternately, the number of waves that occur across the span of the step for a given configuration.

In equation 4.3 we can also prescribe one of the time-varying phase velocities  $z_p(t)$  outlined in the numerical simulations of Kang and Choi (2002). We outline our selected spanwise experimental wavelength and its associated velocity type amplitudes in Section 4.3.4.1 and Figure 4.1.

Figure 3.9 (a) illustrates an additional tube reservoir that is needed for some spanwise wavelengths of actuation to satisfy the continuity equation. In his master's thesis, Gilbert (2007) provides a detailed explanation of when this occurs; for the sake of brevity, this explanation will not be repeated here. Instead, we will provide only the criterion that determines whether or not the additional tube reservoir is necessary. The width of the actuated span,  $W_a = 44.45$  cm, can also be written  $W_a = 8h$ . In order to determine whether connections to the additional tube reservoir are necessary,  $W_a$  should be divided by the spanwise wavelength  $\lambda_z$ . If  $W_a/\lambda_z$  is an integer, the back pressure reservoir is not necessary; if  $W_a/\lambda_z$  is not an integer, then additional hydraulic connections must be made into the tube reservoir. For instance, our current experimental spanwise wavelength is  $\lambda_z = 4h$ .  $W_a/\lambda_z = 8h/4h = 2$ , which is an integer value equal to the wave number, so we did not require the additional tube reservoir for any of the experiments in this thesis.

## 4.3 Experiments Visited

### 4.3.1 Overview

All experiments were performed in the High-Speed Water Tunnel laboratory in the Mechanical Engineering building at the University of Alberta. It should be noted that prior to any of the following experiments, a complete re-calibration of the water tunnel velocity vs. pump RPM relationship was performed to account for any changes in the test section velocity due to the additional head loss from the insertion of the backward-facing step module. Details of the velocity calibration and the associated calibration curve are presented in Appendix A.

We begin this section by outlining an initial experiment to test for Reynolds number independence of the unforced reattachment length in Section 4.3.2. Section 4.3.3 outlines our spanwise-invariant forcing, which is also interchangeably referred to as 2D forcing throughout the remainder of this thesis. Section 4.3.3.1 explains our experiment to determine our optimum perturbation amplitude, followed by an outline of our reattachment length vs. Strouhal number experiments for 2D forcing in Section 4.3.3.2.

Our spanwise-varying (also referred to as 3D) forcing experiments are summarized in Section 4.3.4; beginning with a brief explanation on how the

different 3D forcing amplitudes were calculated in Section 4.3.4.1. We then outline the reattachment length vs. Strouhal number experiments for our spanwise-varying forcing in Section 4.3.4.2.

We end the Section in 4.3.5 with an explanation of several flow visualization experiments in which we used dye to track the development of large-scale structures in the reattaching shear layer.

### 4.3.2 Reattachment Length vs. Reynolds Number

Before we could perform any forcing experiments, we had to first determine whether or not our unforced reattachment length ( $X_{Ro}$ ) was independent of Reynolds number for our ‘high’ and ‘low’ experimental Reynolds numbers. The selection of our high and low Reynolds numbers is explained in greater detail in Section 5.3. For now, note that when we refer to ‘high’, ‘low’, and ‘transitional’ Reynolds numbers,  $Re_h = 12540$  is the ‘low’ Reynolds number,  $Re_h = 24500$  is the ‘high’ Reynolds number, and  $Re_h = 2140$  is the ‘transitional’ Reynolds number.

In this experiment we tested step-height Reynolds numbers ranging from  $Re_h = U_\infty h/\nu = 3770$  to  $Re_h = 46100$ , where  $U_\infty$  was the free stream velocity at the separation edge of the backward-facing step; sometimes called the ‘throat velocity’ or the ‘inlet velocity’. We used the throat velocity to maintain a measure of consistency with the spanwise forcing experiments of Chun, Lee, and Sung (1999) and Henning and King (2007); although in many unforced backward-facing step experiments, the mean free stream velocity downstream of the step is used. Because the bulk of our experiments involved some type of forcing, we felt it was more intuitive to use  $U_\infty$  at separation, because this was the velocity that was used to scale the perturbation velocity  $u'$  (explained in Section 4.3.3.1). When we make any mention of the free stream velocity  $U_\infty$  (and indirectly, any  $Re_h$ ) in this thesis, we are henceforth referring to said separation velocity.

The transitional  $Re_h = 2140$  from the dye experiments was not included in the Reynolds-independence test range, because at the point of testing we were uncertain that the tufts would function at such a low tunnel velocity. Therefore, the baseline  $Re_h = 3770$  represented the lowest  $Re_h$  value of which we could be reasonably certain the tuft plate was working properly (based on a visual inspection of the tufts at  $Re_h = 3770$ ). At lower  $Re_h$  values, such as our transitional  $Re_h$  of 2140, it was possible that the free stream velocity in the test section would not be high enough to cause the tufts to lean over enough to be imaged. These tufts would then be deleted as a result of the criterion outlined in Section 4.4.4.4. It should be noted that an estimation of the minimum tunnel velocity to ensure functionality of the tuft plate was recently completed by Mr. David Sutton, a

Dean's Research Award student who worked with the VfdL in the spring of 2010. David Sutton found that a downstream test section Reynolds number of  $Re_h = 3280$  (corresponding to a separation  $Re_h = 4130$ ) was required for proper functioning of the tuft plate. This value agrees within reason to the separation  $Re_h$  value of 3770 obtained by the author's visual inspection.

### 4.3.3 Two-Dimensional Forcing

#### 4.3.3.1 Reattachment Length vs. Perturbation Amplitude

After we had determined that our high and low  $Re_h$  values were in the fully turbulent regime based on the results from the previous experiment, we tested the dependence of  $X_R/h$  on the forcing amplitude for our high  $Re_h$  value. This experiment was designed to determine the perturbation amplitude at which our forcing became saturated; i.e. the 'base' value of  $u'/U_\infty$ , where further increases in  $u'/U_\infty$  produced no further reduction in reattachment length. We reported the values of  $X_R$  reduction as a fraction of the unforced reattachment length from Section 4.3.2, i.e.  $X_R/X_{R0}$ . In keeping with previous studies (e.g. Kang and Choi, 2002; Henning and King, 2007), we used the maximum slot exit velocity  $u'$  normalized by the average free stream velocity at the inlet  $U_\infty$  to characterize our perturbation amplitude ( $u'/U_\infty$ ).

In his review, Gilbert (2007) noted that perturbation amplitudes in previous suction-and-blowing type actuation studies ranged from 2% to 30% of the free stream velocity, or  $u'/U_\infty = 0.02$  to  $u'/U_\infty = 0.3$ . We tested several perturbation amplitudes ranging from 4% to 108% of the free stream velocity. Amplitudes less than  $u'/U_\infty = 0.04$  were avoided because at the time of testing poor servo frequency response was reported in those regions (Schostek, 2009). The highest amplitude of  $u'/U_\infty = 1.08$  was selected to verify that even at extremely high perturbation amplitudes, increasing perturbation amplitudes after forcing saturation had occurred would produce no further reductions in  $X_R/h$ . We tested these different perturbation amplitudes at a predicted optimal Strouhal number of  $St_h = 0.3$ . This prediction was based on the result obtained by Henning and King (2007) for the same experiment, with nearly identical  $ER$  and  $Re_h$  values. This value of  $St_h$  was also within the optimal range ( $0.16 \leq St_h \leq 0.4$ ) observed by Sigurdson (1995), although his was related to a different separation bubble flow configuration.

Section 5.3.1 presents the results and discussion pertaining to this experiment.

### 4.3.3.2 Reattachment Length vs. Strouhal Number

Following the  $X_R/X_{Ro}$  vs.  $u'/U_\infty$  experiments, we tested the effects of spanwise-invariant actuation on  $X_R/X_{Ro}$  to determine our actual optimal forcing frequency (compared to the predicted value of  $St_h = 0.3$ ). We forced with all ports across the span of the step providing uniform suction-and-blowing actuation, which varied in time following a sinusoidal pattern as per Section 4.2.1. Initially, we tested four different perturbation amplitudes ( $u'/U_\infty = 0.1, 0.2, 0.35, \text{ and } 1.08$ ) for Strouhal numbers ranging from 0 to roughly 0.5. We performed these experiments at the high Reynolds number from before ( $Re_h = 24500$ ) to ensure that we were able to reasonably compare our results to those of similar experiments; in this case, primarily Henning and King (2007).

For reasons explained in Section 5.3.2.2, it was also necessary to perform an experiment at the low Reynolds number ( $Re_h = 12540$ ) to obtain a wider range of  $St_h$  values. In this experiment we tested only our saturation perturbation velocity ( $u'/U_\infty = 0.35$ ) over Strouhal numbers ranging from 0 to 0.93.

Section 5.3.2.1 presents the results and discussion from the high  $Re_h$  case, while Section 5.3.2.2 does the same for the low  $Re_h$  case.

## 4.3.4 Three-Dimensional Forcing

### 4.3.4.1 Spanwise Wavelength and Amplitude Calculations

Of the possible spanwise wavelengths outlined in Section 4.2.2, we selected  $\lambda_z/h = 4$ , which was the optimum value specified by Kang and Choi (2002). This wavelength meant that 8 adjacent actuation ports forced at the same perturbation amplitude, as outlined in Figure 4.1. These 8 adjacent forcing amplitudes make up what we will refer to as a single “velocity type”.

In order to characterize our 3D forcing amplitudes, we set the spatial RMS value of our ideal cosine wave (Section 4.2) to equal the peak amplitude from the corresponding 2D forcing experiment. For instance, for 2D forcing with a peak amplitude of  $u'/U_\infty = 0.1$ , to have an equivalent amplitude for our 3D forcing we would set the RMS value of our ideal cosine wave to be  $u'_{rms}/U_\infty = 0.1$ . The peak perturbation velocity of the ideal cosine wave would then be  $\sqrt{2}(0.1) \approx 0.14U_\infty$ . Knowing the peak velocity and period of our spatial forcing profile, we calculated the appropriate values of each discrete element of our forcing amplitude approximation (the stepped black line in Figure 4.1) by simply integrating the cosine function over the relevant domain.

Figure 4.1 illustrates the above idea for an arbitrary  $u'/U_\infty$  value of 1, for the 3D forcing profile outlined in Section 4.2 and used throughout Section 5.4. In Figure 4.1, the high and low perturbation velocity values for the cosine wave (calculated using the above integration average) are 0.903 and 0.37 (and their corresponding negative values).

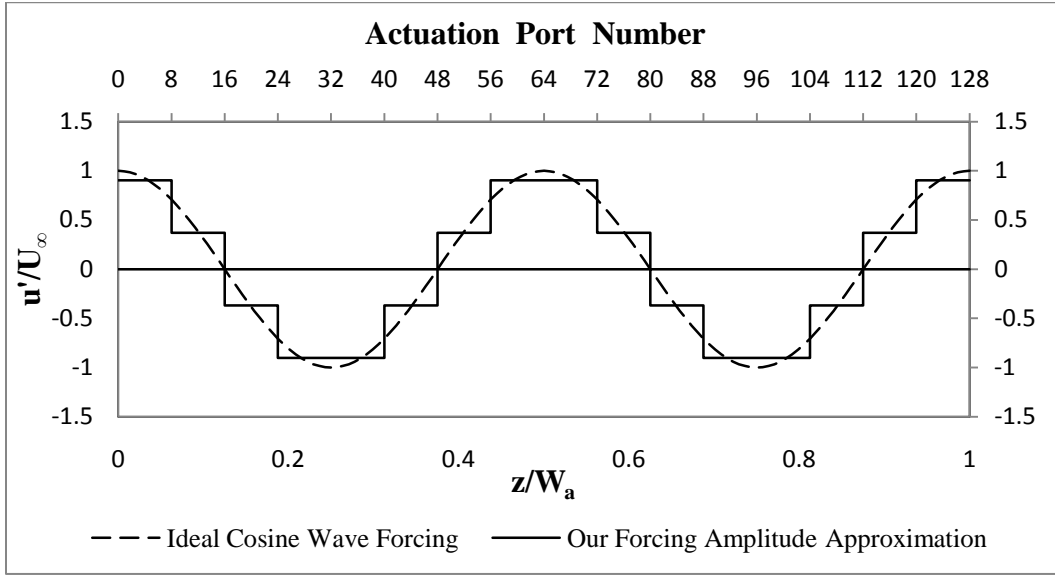


**Figure 4.1** Our cosine forcing approximation for a spanwise wavelength of  $4h$ , with an arbitrary perturbation amplitude of 1. The upper horizontal axis indicates that for this wavelength, 8 adjacent tubes force at a given velocity type. The bottom horizontal axis indicates the spanwise location normalized by the actuated span.

#### 4.3.4.2 Reattachment vs. Strouhal Number

To test our spanwise-varying forcing, we employed one of the open-loop forcing strategies from the numerical simulations of Kang and Choi (2002). Their forcing varied in a sinusoidal pattern across the span or the step, and we mimicked this using the spatial approximation of Section 4.3.4.1. This meant that our forcing was both temporally and spatially varying in sinusoidal patterns, although the spatial variance was only an approximation of a cosine wave. We also forced using their recommended spanwise wavelength of  $\lambda_z/h = 4$ . Due to the fact that our aspect ratio was twice as large as theirs, in our experiments  $\lambda_z/h = 4$  resulted in two full waves across the span versus only one for Kang and Choi (2002). The selection of this wavelength meant that the back pressure reservoir for additional hydraulic tubes was not necessary, as per the criterion outlined in Section 4.2.2.

In their experiments, Kang and Choi (2002) also tested three types of time-varying phase values, which altered the location of the spatial sine wave on the step's span. The first was zero phase velocity, which produced a stationary actuation profile varying only in time across the span of the step. Second, they

used what they termed a quasi-random phase (QRP), which moved the forcing pattern semi-randomly across the step's span in an attempt to reproduce some of the results from their suboptimal feedback control simulations. Finally, they tested a constant phase velocity, which continually moved the sinusoidal forcing pattern across the span of the step at a constant speed. Kang and Choi (2002) found that both the standing sine wave (zero phase velocity) and the sine wave moving in  $z$  at a constant phase velocity promoted further reductions in  $X_R$ , while the QRP did not.

In light of these results, we elected to force with zero phase velocity for our initial experiments, although our control system would have also been capable of implementing the constant phase velocity simulations as well. We centered the cosine wave over the span of the step, primarily to ensure that the forcing was symmetric about the RoboStep's centerline, but also to ensure that one of the predicted regions of maximum  $X_R$  reduction would be in the center of the test section window for image processing purposes. Also, the centered cosine wave more closely approximates the one used by Kang and Choi (2002) in their zero-phase velocity experiments.

To enable comparisons with our 2D forcing experiments, we performed both high and low  $Re_h$  tests for our 3D forcing experiments. At  $Re_h = 24500$ , we tested only the three lower perturbation amplitudes ( $u'_{rms}/U_\infty = 0.1, 0.2,$  and  $0.35$ ) to avoid the problems with servo overworking that we observed in our 2D experiments for  $u'/U_\infty = 1.08$  (Section 5.3.2.1). At  $Re_h = 12450$ , we again tested at our optimal perturbation amplitude of  $u'_{rms}/U_\infty = 0.35$ .

Section 5.4.1 presents the results and discussion from the high  $Re_h$  case, while Section 5.4.2 does the same for the low  $Re_h$  case.

### 4.3.5 Dye Visualization

Up until this point, the experiments that we have undertaken have focused mostly on obtaining time-averaged data pertaining to the reattachment length (or reduction thereof). In order to learn more about the flow itself (the LSS present, the evolution of vorticity, and the effect of forcing on said structures), we performed a series of experiments using backlit dye as a flow visualization tool. Images and videos of the flow were captured over two sets of experiments; one at our low  $Re_h = 12450$ , and one when the recirculation bubble was transitioning to turbulent ( $Re_h = 2140$ ). At each Reynolds number, images and videos of the flow were taken for zero-excitation, 2D forcing, and 3D forcing cases. For the transitional Reynolds numbers, we forced at both the optimal  $St_h = 0.35$  and also at one half the optimal frequency.

Prior to image or video capturing, the dye reservoir's gate valve (Figure 3.11) would be opened for a very short time to allow a mass of dye to accumulate at the dye ejection slit. The valve would then be shut, and the dye that was introduced into the flow would be entrained and convected downstream in the LSS that developed during separation. At this point, image or video capture would occur, and the process would be repeated as necessary.

It would have been much easier to leave the gate valve open and continually add dye into the flow, but the Gentian Violet dye (Hexamethyl Pararosaniline Chloride) that we used was particularly powerful. The water tunnel, being a closed-loop system, would have become quickly saturated with dye thereby destroying backlit image contrast (for both dye and tuft plate images). Draining and refilling the water tunnel was also an option, but this would have required the air bleed procedure (Appendix C1) to be redone in order to re-expel any air bubbles that may have worked themselves into the hydraulic forcing lines during tunnel draining. For this reason, the dye visualization experiments were the last experiments performed involving image capturing.

A final challenge with the dye visualization experiments occurred due to density inequalities between the dye contained in the dye reservoir and the water in the water tunnel. By the time of the dye experiments, a small failure of the mechanical seal in the water tunnel's pump had occurred. The tunnel could still hold water and run without any major problems, but the resulting leak was substantial enough that a near-continuous addition of water was necessary during experimentation. This meant that during long periods with the tunnel running, the mean water temperature would drop due to the constant addition of cold water. This was a problem for all of the experiments from Sections 5.2 to 5.4, and it required that we constantly monitor the water temperature in order to match kinematic viscosities (and therefore Reynolds numbers) between experimental runs. In the case of the dye experiments, the solution to the challenge was to add cold water to the dye reservoir prior to visualization. Doing so minimized the buoyancy effects that the dye would have experienced had it been left warmer than the tunnel water.

## **4.4 Reattachment Location Measurement**

### **4.4.1 Overview**

Although the dye injection system described in Section 3.5 served as an effective method to track vorticity in the flow, we required a different method to effectively measure  $X_R$ . Section 4.4.2 outlines our development of a novel type of aqueous tuft array to do so.

Sections 4.4.3 and 4.4.4 (respectively) explain how we collected multiple images of this tuft plate, and then processed them using a MATLAB program to obtain time-averaged flow field and reattachment location data. Save for the dye photos, all of the results presented in Section 5 were obtained using this data collection and processing scheme.

#### **4.4.2 Tufts**

Tufts, also called telltales, are common flow visualization tools used primarily in aerodynamic studies. When used in air, tufts are typically bits of thread fastened to a surface to serve as a method for determining air flow direction at the surface and/or the location where the flow separates from, or reattaches to, the surface.

We decided to develop a tuft to work in water at low velocities to serve as a method for determining  $X_R$ . The reattachment line could be determined by placing an array of tufts downstream of the backward facing on the reattachment wall. Any tufts in the recirculation region would be pointing upstream toward the step, while the tufts past the reattachment line would be pointing downstream. For an unsteady separation bubble, the reattachment line would be defined when a tuft spends equal amounts of time pointing both upstream and downstream.

##### ***4.4.2.1 Aqueous Tuft Requirements***

In order to minimize buoyancy effects, the selected tuft material's density was matched as closely as possible to that of water. The material also had to be as close to infinitely flexible as possible, so that the tufts were responsive to rapid fluctuations in velocity and low tunnel velocities as well.

The tuft material thickness and cross sectional areas were kept as small as possible to keep disruptions to the flow field to a minimum; however, because the images for processing were backlit, the tufts had to be opaque and wide enough that they would not allow light to pass through.

##### ***4.4.2.2 Tuft Development***

Initial testing and research toward a suitable tuft material and configuration was conducted in conjunction with Dory Parsonage. We tested a number of different materials, including (but not limited to): Dacron braided fly-fishing line, sewing thread, thin strips of both high and low density polyethylene, polyvinylidene chloride strips, and latex strips.

As was true for Ferrell (1991), our initial experiments identified latex as the most suitable candidate material. However, Ferrell used his tufts at substantially higher flow velocities. He was able to use larger tufts in both surface area and thickness,

because the hydrodynamic forces acting on his tufts were sufficient to overcome the material stiffness. Because our minimum flow velocity was much less than Ferrell's, and because we were more constrained in allowable tuft size, Ferrell's tufts would not have worked in our experiments.

In addition, problems with material porosity arose during our long term testing of the latex tufts. When the tufts were immersed for periods longer than a few days, small pores and roughness on the surface of the tuft would lead to the formation of bubbles which would cling to the tuft. These bubbles were of sufficient size to make the tufts buoyant enough that they had a strong vertical bias.

The remainder of the tuft material selection process was completed by Marc Schostek, who developed an effective tuft with none of the problems outlined above. He also developed a construction method which allowed identical tufts 19.05 mm long by 0.635 mm wide by 0.1016 mm thick to be produced consistently. The selected tuft material and the complete construction method will be discussed in full in Marc Schostek's M.Sc. thesis.

#### ***4.4.2.3 The Tuft Plate***

After experimenting with various tuft attachment methods, it became evident that the best way to affix the tufts to the reattachment wall was to 'plant' the tufts individually in 1 mm diameter holes in a transparent plate. Doing so ensured that the tufts protruded perpendicularly into the flow, which eliminated the upstream/downstream bias that would have occurred had the tufts been taped or glued flat as in aerodynamic studies.

The tuft plate, designed by NSERC Undergraduate Summer Research Assistant Dory Parsonage, was machined out of a 3.175 mm thick clear polycarbonate sheet, with tuft grid spacing at 20 mm by 20 mm. The tuft plate was affixed to the test section window by four specially machined bolts, as seen in Figure 4.2.

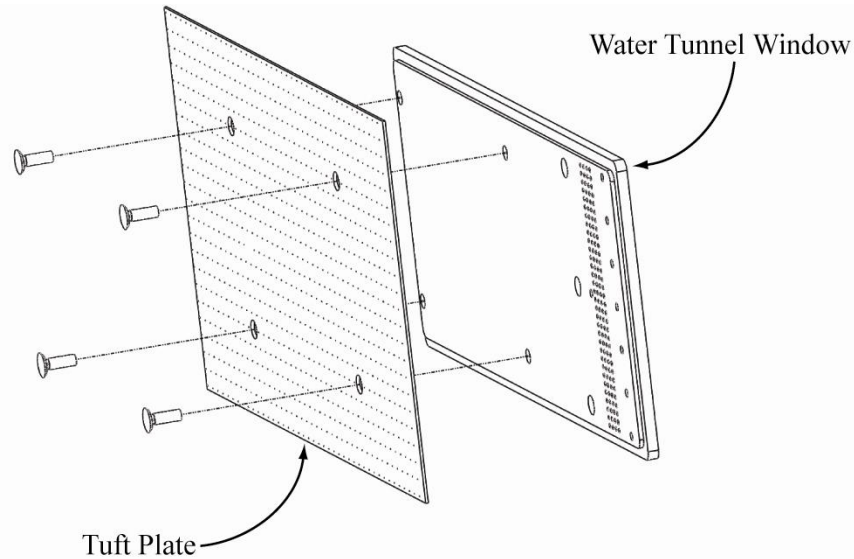


**Figure 4.2** The method in which the tuft plate was fastened to the interior side of the water tunnel test section window.

The tuft plate was designed to cover more than an entire test section window, so dimensions of 453 mm by 870 mm were selected. These dimensions and the aforementioned grid spacing meant that 989 tuft holes were drilled into the plate. Our data collection and image processing method (explained later in Section 4.4.3) required that images of the tuft plate be backlit. Because of this fact, and also the fact that the transparent test section window was smaller than the tuft plate dimensions, a maximum of 544 of the 989 total tufts were used per image in digital data processing. The tufts that were not illuminated for image processing were still used as qualitative flow visualization tools and also for determining  $X_R$  by eye.

Indeed, the entire tuft array could have been used by itself as a real-time method for determining  $X_R$  by eye, but the measured value would have only been accurate to within 2 cm – the spacing between the tufts. This problem in accuracy was compounded by the fact that the reattachment line itself fluctuated in time, due to the periodic “flapping” of the shear layer as described by Hasan (1992). Any instantaneous reading of  $X_R$ , by eye or by an analysis of a single tuft array image, would have failed to account for these temporal fluctuations. These problems led to the development of a data collection/image processing scheme discussed presently.

#### **4.4.3 Data Collection**

Once experimental run characteristics had been defined and the water tunnel was operating steadily (with or without forcing), data collection could occur. As was

previously mentioned, data collection involved taking a series of backlit images using a Nikon D1x digital SLR camera. The images were backlit by a drafting table which was modified to provide uniform white light while in a vertical position. The camera had a pixel resolution of 3008 by 1960, and all data was collected with the camera situated approximately 2 meters away from the tuft plate. This working distance was necessary in order to fit all four tuft plate fastening bolts in frame, which was a general criterion that was followed for all tuft plate images. The four bolt criterion is explained later in Section 4.4.4.1.

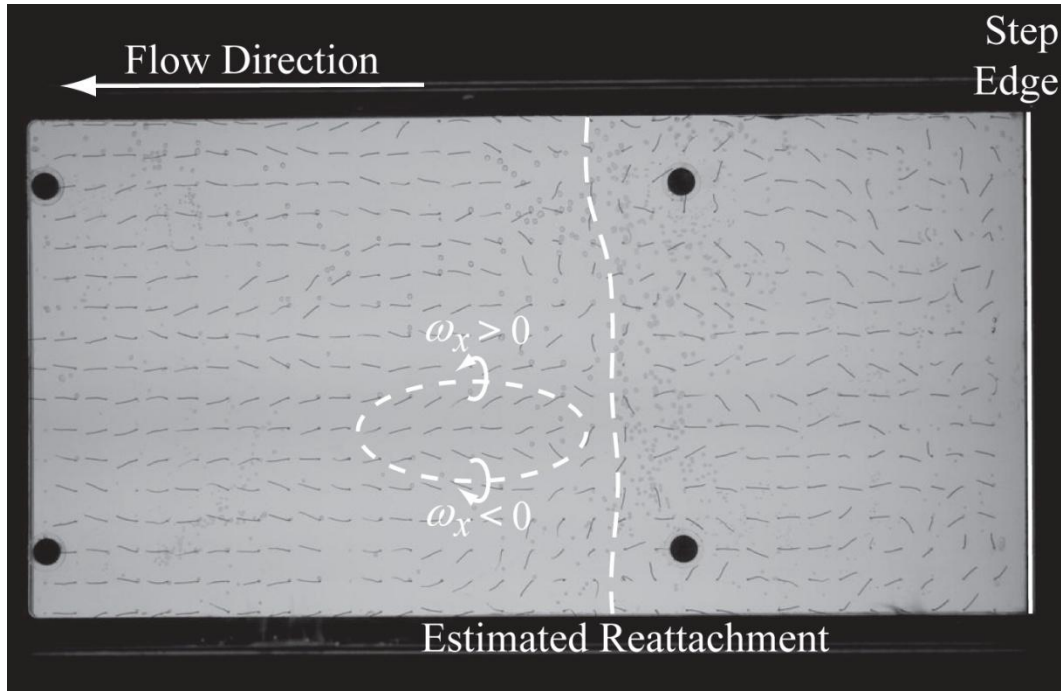


**Figure 4.3** An example of an unprocessed tuft plate image, with the backward-facing step edge and flow directions shown. The reattachment line, estimated by eye, is indicated by the vertical dashed line. A second dashed line highlights a region (NOT a vortex line) containing a possible counter rotating streamwise vortex pair, with positive  $\omega_x$  at the top of the region and negative  $\omega_x$  at the bottom.

Images were obtained in groups of approximately 20 due to the camera’s “buffer memory” wait time, which occurred when the camera was downloading from its virtual cache onto a CompactFlash digital memory card. Three 1GB CompactFlash cards were used in a rotation system, where each card was able to hold approximately 50 raw images. For any given experimental run corresponding to a single data point (i.e. one set at a specific Strouhal number, with a specific perturbation amplitude, at a specific Reynolds number), between 50 and 150 images were obtained. An example of an unprocessed image can be seen in Figure 4.3.

Although it is not directly related to the concepts of this section, here we will mention an interesting feature of the raw image from Figure 4.3 as well. Earlier in Section 1.1, we predicted the presence of interlocking counter rotating streamwise vortex pairs (Figure 1.1) in the downstream region of the backward-facing step based on the results of Sigurdson and Roshko (1984) and Sigurdson (1986 and 1995). In Figure 4.3, a region containing a possible counter rotating vortex pair is highlighted by a white dashed line; note that the line DOES NOT indicate a vortex ring – it merely highlights the region exhibiting the phenomenon. The series of downward-pointing adjacent tufts at the top of the region indicate that these tufts are in an area of downward-biased local flow; a situation which could be explained by the presence of coherent positive streamwise vorticity in the near wall region. The converse is true for the series of tufts at the bottom of the region, possibly indicating the presence of another streamwise vortex with negative  $\omega_x$ . Although this observation does not prove the presence of the aforementioned streamwise vortex pairs, the encircled region does illustrate the presence of coherent structures in the flow that merit further study.

#### **4.4.4 Image Processing**

In order to extract time-averaged data from sets of multiple tuft plate images, we used a MATLAB program called ‘tuftImgProApp.m’. This program was designed and coded by David Breakey. Although we worked as a team on the broad conceptual elements of this project, the ideas and terminologies presented in the remainder of this section were largely his. Detailed program information and usage instructions can be found in Appendix E.

##### ***4.4.4.1 Image Registration***

When raw images (such as Figure 4.3) were processed by tuftImgProApp.m, the program first registered the images. Essentially, image registration involved matching the image’s coordinates to known fiduciary markers in the step’s coordinate system. The bolts used to fasten the tuft plate to the test section sufficed, as Duda and Hart’s (1972) Generalized Hough Transform was applied to recognize them.

With these markers in place, the program then determined if any rotation was necessary. Although it was possible for the program to perform the rotation calculation with only two fiduciary markers showing, if four markers were showing the program was able to perform the rotation calculation twice and then average the results. This gave more accurately registered images, and was the reason for adherence to the four bolt criterion.

#### ***4.4.4.2 Tuft Isolation***

Once the images were registered, tuftImgProApp.m ran them through a series of built-in MATLAB image processing functions to isolate the tufts as separate parts of the images. Binary images of the tufts, which were determined by the Sobel edge detection method, underwent sequential hole-filling and connecting algorithms which produced unbroken white tufts one pixel thick on inverted black backgrounds.

Next, any white pixels within a ten pixel radius of the tuft's origins (the holes in which they were fastened into the tuft plate) were omitted. This was done to ensure that the flow was accurately represented by the furthest 80% of the tufts from their origins, in case any of the tufts had slight biases at their origins. These biases most often occurred due to glue seeping up the tuft's anchor points and hardening at angles non-normal to the tuft plate. This deletion threshold also handled pixel remnants from the hard edges of the tuft holes that may have escaped the tuft isolation phase.

A second type of deletion was used if an object's size in pixels was greater or less than sixty percent of the acceptable tuft size. This threshold deleted objects such as large, isolated bubbles in the tuft plate images.

#### ***4.4.4.3 Tuft Direction Determination: The Centroid Method***

Initially, the tuft directions were determined by digitally drawing vectors from the tuft's origins through their centroids and then normalizing the magnitudes of each vector to unity. The centroids were computed based on pixel area calculations of the tufts. A major assumption of this method was that the tuft's origins were infinitesimally small points in space, when in reality, the tuft's origins could have been anywhere within the 1 mm diameter drilled holes in which they were affixed. The directions of the output vectors were often slightly altered if the actual and predicted tuft origins were not coincident.

#### ***4.4.4.4 Tuft Direction Determination: The Regression Method***

A least squares linear regression method was used to remedy the problems of the centroid method. In the regression method, each component pixel of a given tuft was treated as a separate point in a data set. A linear regression was then performed on each tuft, and the slope and intercept for said tuft were returned as outputs. The regression method did not impose predicted origins on the tufts, thereby eliminating the problems of the centroid method. Much more accurate vector slopes were consistently calculated using this method, as was verified during the program de-bugging process (Breakey, 2009).

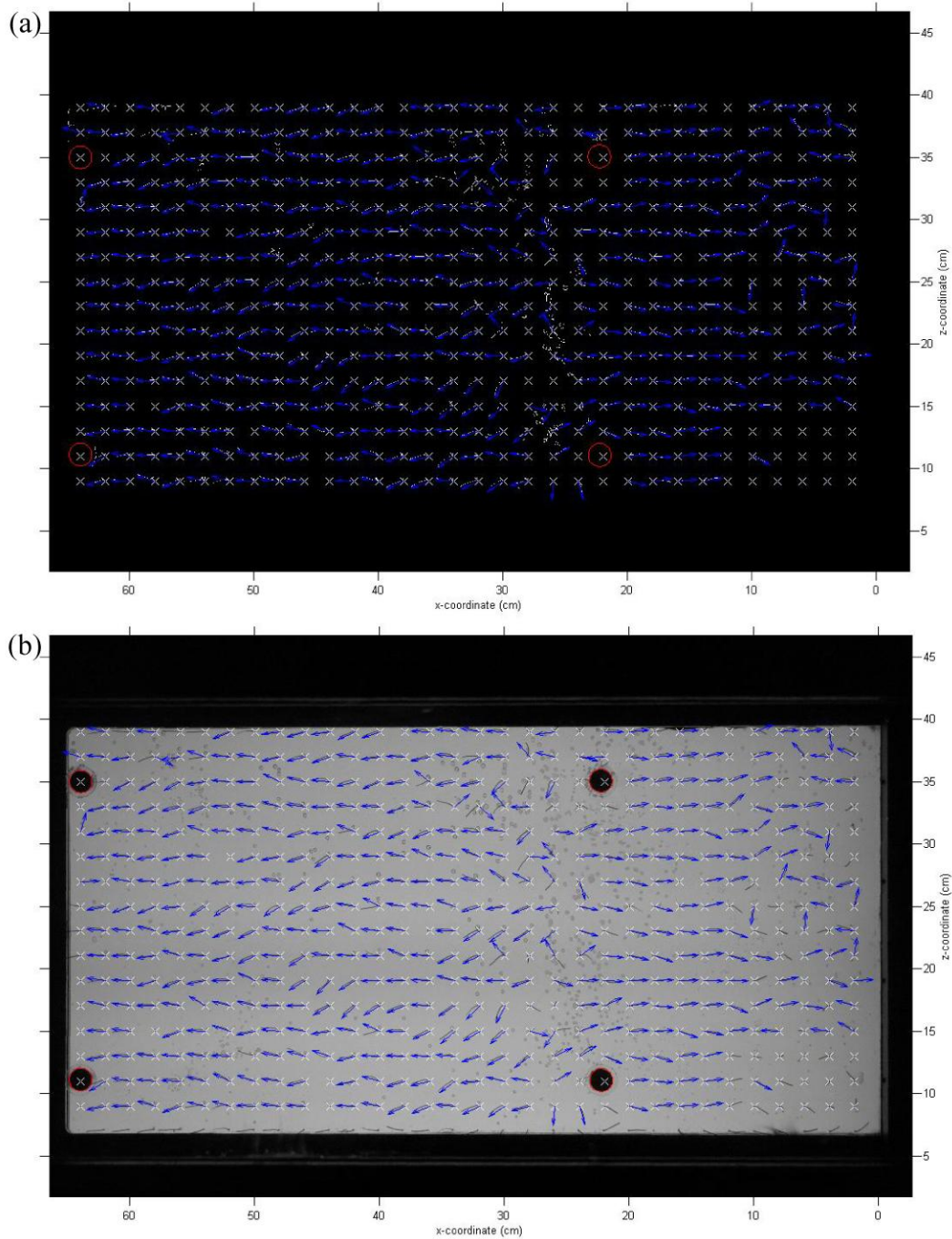


**Figure 4.4** Single-image vector field calculation plots. (a) A sample single tuft plate image (vector field superimposed) after image registration. (b) The resulting output vector field image from the image registration process. Top and bottom water tunnel walls are at  $z = 46$  cm and  $z = 0$  cm, respectively, and the step edge is at  $x = 0$  cm.

The regression method outperformed the centroid method in nearly all cases; the only exceptions occurred when tufts were perpendicular to the free stream flow in the  $x - z$  plane, i.e. when tufts were pointed directly toward the camera. In these cases, there would be too little of a given tuft showing in the image to perform

any meaningful calculations. This problem was solved by implementing another threshold which deleted tufts that were perpendicular in this way  $\pm 5\%$ .

A sample vector field calculated using the least squares regression method is presented in Figure 4.4 (b). Its corresponding registered image is presented in Figure 4.4 (a). Note that not all tufts in the images were assigned vectors due to some of the deletion and omission methods outlined above.

The processing time for each raw image was approximately one minute. Processing time included registering the image, isolating each tuft, performing regression calculations to calculate a vector field, producing an output image with the vector field superimposed, and creating an output Excel data file that contained all of the calculated vector field data. This meant that for a single data point of 50 images (at a specific Strouhal number, with a specific perturbation amplitude, at a specific Reynolds number), it took roughly one hour to process all of the images. This processing time excluded the time it took to average multiple images to obtain time-averaged data; this was done in a separate step (Section 4.4.4.6), and typically took only a minute or so.

#### ***4.4.4.5 Experiment-Specific Problems***

In addition to the aforementioned built-in deletion and omission methods, there were also several problems intrinsic to the experiment that led to further errors in the image processing scheme. These problems caused either no vectors to be calculated or erroneous vectors to be assigned.

In order to prevent water leakage through the bolt holes and some of the backward-facing step holes, a silicone sealant called vacuum grease was applied to problem areas. This sealant infrequently caused some of the tufts near the bolt holes to stick to the tuft plate in arbitrary directions. This led to incorrect vectors being calculated for obvious reasons. Whenever possible, this problem was remedied by briefly increasing the free stream velocity until the stuck tufts loosened from the surface of the plate, and then returning the water tunnel to the desired experimental run speed.

Tufts along the illuminated edges of the images were also frequently omitted if less than 80% of a given tuft was visible (Figure 4.4). Unfortunately, this problem was not easily fixed, and it accounted for any nonsense data around image edges.

The most significant experimentally-based problem occurred when small air bubbles formed between the tuft plate and water tunnel window. As cold water (present in the water tunnel after filling) warmed, dissolved air became less soluble leading to the formation of these bubbles. The bubbles were visible as

small, darker grey areas in the unprocessed images (Figure 4.3). These bubbles were problematic because they were too small to be deleted by the method outlined in Section 4.4.4.2, but large enough that they resulted in clusters of erroneous white pixels in the registered images as seen in Figure 4.4 (a). It should be noted that Figure 4.4 (a) and (b) were selected mainly to illustrate the effect of these problems on the image processing program; they are not accurate representations of typical output images from `tuftImgProApp.m`. Any zero vectors were not counted in the averaging calculations.

#### ***4.4.4.6 Averaging Velocity Field Data***

After `tuftImgProApp.m` had processed a series of images, a second graphical user interface window (Appendix E2) was opened to obtain time-averaged vector field data from all of the images in the given data set. Two methods were used to obtain averaged vector field data: vector magnitude averaging and percentage of images downstream. For all experiments using image processing, data was recorded using both methods.

Figure 4.5 (a) and (b), and Figure 4.6 (a) and (b) show output images produced by the vector magnitude averaging calculation method. The (a) plots of these figures show output data generated without normalizing all vectors to unity, while the (b) plots show data after unit normalization. The reattachment lines are shown as black lines in Figure 4.5.

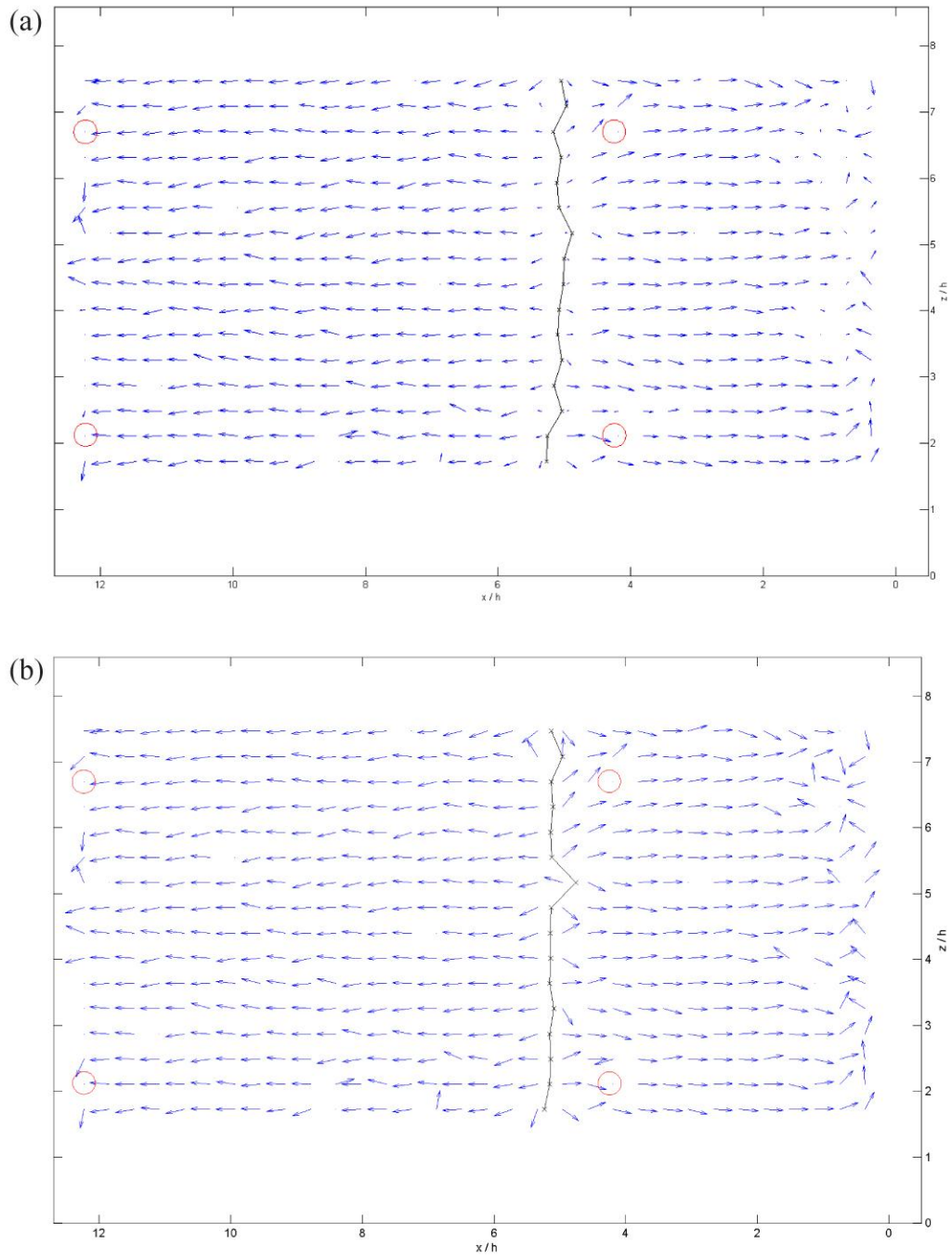


**Figure 4.5 Time-averaged vector fields generated by the vector magnitude averaging calculation method. (a) Without unit normalizing. (b) With unit normalizing.**

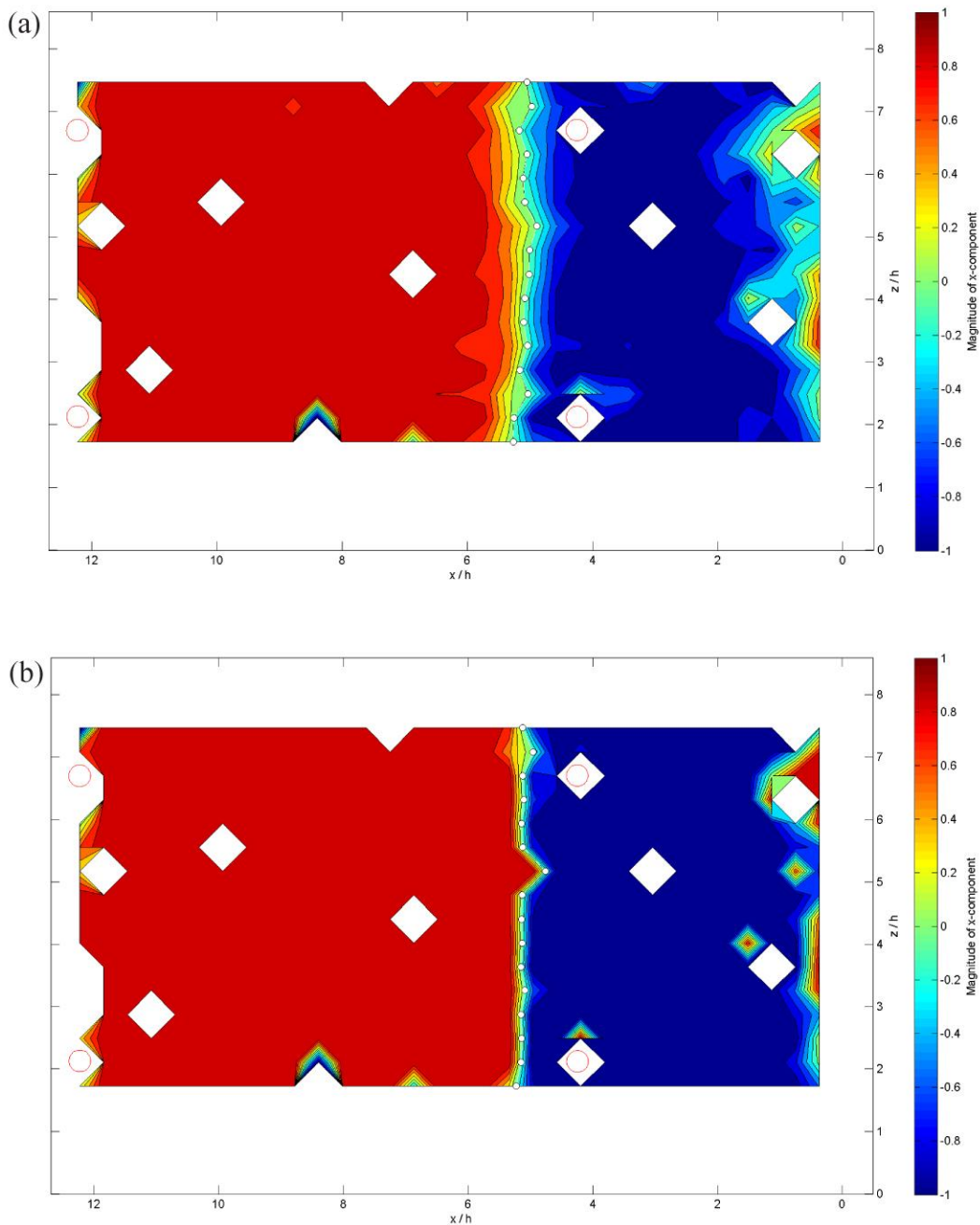


**Figure 4.6 Time-averaged contour plots generated by the vector magnitude averaging calculation method. (a) Without unit normalizing. (b) With unit normalizing.**

As before, the attachment bolts are indicated by red circles in the plots. In Figure 4.6, red regions indicate downstream pointing tufts and blue regions indicate upstream pointing tufts; tufts that were destroyed during experimentation are represented by white diamonds. The reattachment lines are shown by white dotted lines in Figure 4.6. Nonsensical data immediately downstream of the step can be

attributed to the fact that the tufts were not moving in this region, so incorrect vectors were calculated based on any slight bias that the tuft had. The differences between the average  $X_R$  values produced by the non normalized and normalized unit vector averages will not be discussed here, due to the fact that the remainder of this thesis focuses on data produced by the second method of time averaging.

The second method of obtaining time-averaged flow field data involved a purely statistical approach. In this method, termed the ‘percent of images downstream’ method, the number of images in which a tuft appeared to be pointing downstream was divided by its number of nonzero instances for a given experimental run. We chose to focus on this method because it did not rely on any component magnitudes of the vectors, of which we could not be completely certain. Also, the image processing program as a whole was used more as a tool to track changes in the reattachment lengths due to forcing, not so much the absolute reattachment lengths. Because we used the percent downstream method to calculate our reported results consistently, the differences between the averaging methods was not seen as a problem. As was previously mentioned, we still used the other averaging methods as coherence checks; calculated  $X_R$  values from each of the three methods differed from each other by a maximum of 0.5%. Due to the consistency in results produced by the different reattachment calculation methods, we will focus only on the percent of images downstream method for the remainder of this thesis.

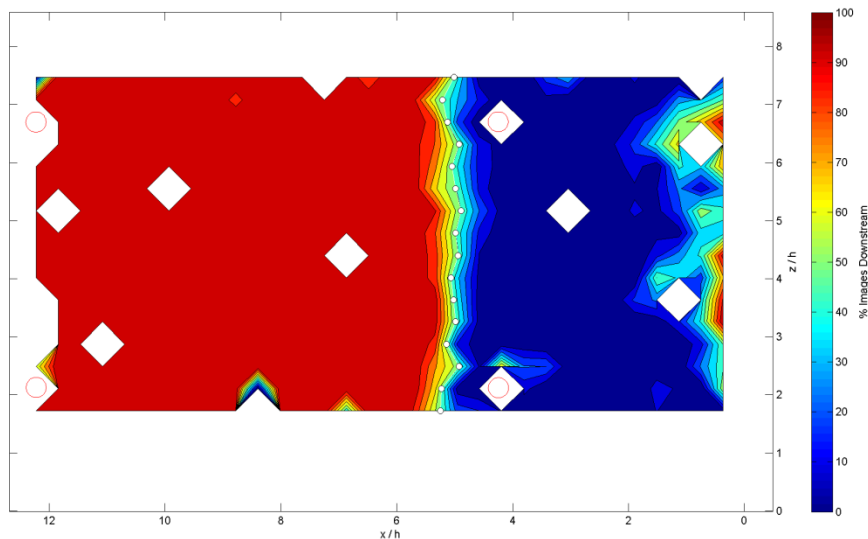


**Figure 4.7** An output contour plot from the percentage of images downstream averaging method. The bolts, missing tufts, and reattachment line are shown in the same way as with the magnitude averaging method.

Figure 4.7 shows a sample output plot from the percentage of images downstream method. All time-averaged contour plots and vector magnitude plots of this nature were produced using the output data in the automatically generated Excel data files. It should be noted that all of the sample vector and contour plots in this section were taken from an experimental run (3D forcing,  $Re_h = 24500$ ,  $St_h = 0.06$ ,  $u'/U_\infty = 0.1$ ) in which the forcing was ineffective in producing any notable change in reattachment. In cases with more effective forcing, it was possible for the reattachment line to fall across the two bolts closest to the step edge. When this occurred, tuftImgProApp.m interpolated between neighboring tufts to fill in the reattachment data.

## 5 Results and Discussion

### 5.1 Overview

In this section we summarize and discuss the significant results obtained from the experiments outlined in Section 4.3. Complete experimental results are presented in their entirety in Appendix B. We begin the remainder of this Section in 5.2 with the results from an initial reattachment length vs. Reynolds number test for the case of no hydraulic actuation.

Section 5.3 outlines the results of the 2D forcing experiments undertaken to determine optimal perturbation amplitudes (Section 5.3.1) and Strouhal numbers (Section 5.3.2) for said forcing. This experimental order is the same as the one used by Henning and King (2007) as a precursor to their 3D forcing experiments.

The 2D optimum values were then used to design a series of 3D reattachment vs. Strouhal number experiments; the results from these 3D forcing experiments are presented in Section 5.4, for both high (Section 5.4.1) and low (Section 5.4.2) turbulent Reynolds numbers.

A comparison of 2D and 3D forcing techniques is undertaken in Section 5.5, based on the results obtained in Sections 5.3 and 5.4. Section 5.6 contains results from a separate set of experiments in which we used dye to track the evolution of vorticity in the flow. In 5.6.2 we present a short discussion on the effect of 3D forcing on the LSS present in the reattaching shear layer.

### 5.2 Reattachment Length vs. Reynolds Number

We first conducted a reattachment length vs. Reynolds number experiment to determine whether or not our average reattachment lengths were independent of step height Reynolds numbers for turbulent flow. We ensured that the range of Reynolds numbers contained our ‘high’ ( $Re_h = 24500$ ) and ‘low’ ( $Re_h = 12540$ ) values from our 2D and 3D forcing experiments.

Figure 5.1 plots the results of this experiment. We tested step-height Reynolds numbers ranging from  $Re_h = 3770$  to  $Re_h = 46100$  – a wide range of Reynolds numbers that encompassed the vast majority of  $Re_h$  values from other backward-facing step studies. Again, note that these Reynolds numbers were based on the free stream velocities ( $U_\infty = 6.7$  cm/s and  $U_\infty = 81.5$  cm/s, respectively) at the separation edge of the backward-facing step. Note also that each data point represents a time-average of at least 50 images. This criterion is also true for the data presented in Sections 5.3, 5.4, and 5.5.

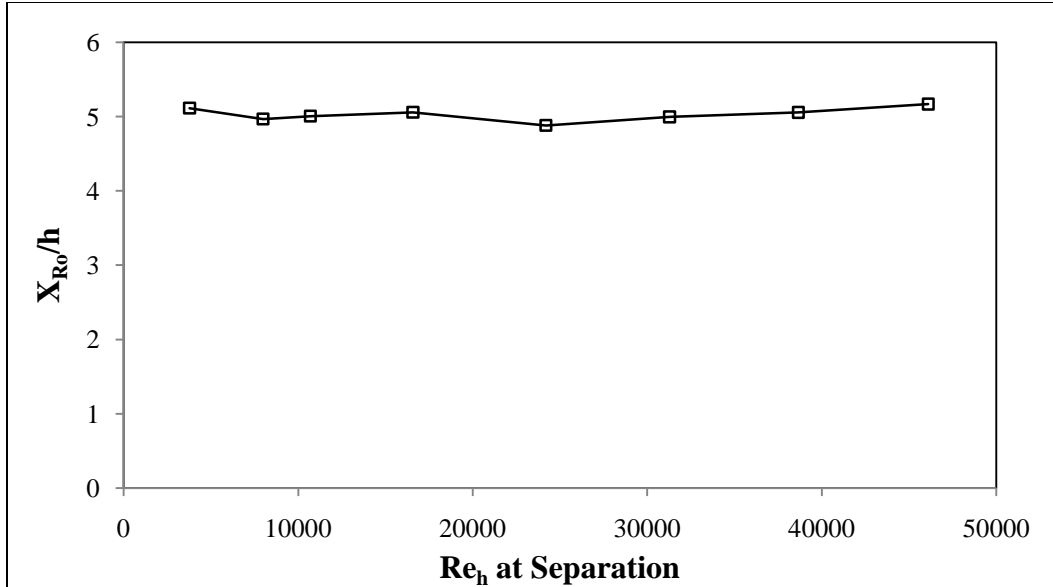


**Figure 5.1** A plot of the average unforced reattachment lengths for various step-height Reynolds numbers. As will be common practice from the remainder of this thesis, only data from the percent of images downstream calculation method is presented.

The average unforced reattachment location occurred at  $X_{Ro} = 26.3$  cm, or  $X_{Ro}/h = 5.0$  with the value normalized by the step height. This was calculated using the percent of images downstream method (Section 4.4.4.6), with the standard deviation between  $X_{Ro}/h$  values measured at 0.09 step heights. We therefore use  $\pm 0.1h$  as an initial conservative estimate of the uncertainty in our  $X_R/h$  measurements; a more detailed error estimate can be found in Appendix F. The other three  $X_R$  calculation methods (unit normalized vector magnitude averaging, non-normalized vector magnitude averaging, and estimation by eye) provided results that agreed with the percent of images downstream method to within 0.5% consistently.

Our consistent baseline reattachment length of five step heights proved that our high and low  $Re_h$  experiments were fully turbulent and Reynolds number independent. However, our average  $X_{Ro}/h$  value was unexpected in that it was significantly shorter than the widely accepted standard of approximately seven step heights. In their review of previous studies, Chun and Sung (1996) reported unforced  $X_R/h$  values between 6.0 and 8.2 for turbulent experiments with  $Re_h$  values ranging from 11000 to 42000 and aspect ratios from 12 to 30.5.

To explain the variations in  $X_{Ro}/h$  values between different experiments, Adams and Johnston (1988b) stated that reattachment locations were functions dependent on  $ER$ ,  $Re_h$ , inlet  $\delta/h$ , and the inlet boundary layer quality (laminar or turbulent). We examined these effects as possible explanations for our unusual  $X_{Ro}/h$  value; but having already verified that our experiments occurred in  $Re_h$  independent

regimes,  $Re_h$  was not considered as a possible contributing factor. Although  $ER$ ,  $Re_h$ , and the inlet flow conditions (i.e.  $\delta/h$ ,  $\theta$ , boundary layer quality, turbulence intensity, and velocity profile) were identified by other studies (discussed presently) as the primary factors in determining baseline  $X_R/h$ , there were two additional factors specific to our experiment that we also considered: a large screen downstream of the backward-facing step and our non-2D aspect ratio.

Armaly et al. (1983) noted that as expansion ratios ( $ER = H/H_i$ ) decreased,  $X_R/h$  values seemed to lessen as well. This idea was echoed by Eaton and Johnston (1981) and later confirmed by Ötügen (1991), who showed that the shear layer tended to grow faster as  $ER$  lessened, which led to shorter reattachment lengths. Ötügen (1991), however, also noted that the changes in  $X_R/h$  caused by altering  $ER$  were typically very small; usually on the order of 5% when  $ER$  was decreased to 50% of its original value.

Considering that our value of  $ER = 1.26$  was very close to other  $ER$  values of 1.25 (Adams and Johnston, 1988a and 1988b) and 1.27 (Henning and King, 2007) for similar Reynolds numbers, we expected our  $X_{Ro}/h$  value to be much closer to theirs ( $X_{Ro}/h \approx 6.5$  and  $X_{Ro}/h = 7.2$ , respectively). Because they were not, we concluded that  $ER$  was most likely not a significant contributing factor toward our atypical  $X_{Ro}/h$  value.

Approximately 1.8 m downstream of the backward-facing step, we placed a large screen inside the end of the test section to catch any RoboStep components that became accidentally detached during an experimental run. The blockage from to the screen was about 35% of the total test section area, due to the fact that the screen mesh had to be thick enough that it could withstand collisions with heavy metal pieces at potentially high velocities. Yao et al. (2007) ascertained that a filter placed downstream of a backward-facing step made a significant contribution to the adverse pressure gradient in that area, thereby causing the baseline reattachment location to occur earlier than it would have with no filter in place. However, Yao et al. (2007) placed their filters at downstream locations within  $(4.25h)$  and just beyond  $(6.75h)$  their baseline reattachment length  $(6h)$ ; both of these locations were considerably closer to the BFS than our downstream screen location of over  $30h$ . Due to this difference in downstream screen locations, we concluded that ours was not close enough to the BFS to make a significant contribution to the downstream adverse pressure gradient. For this reason, we concluded that the presence of the screen did not make any significant contributions to the baseline reattachment location.

We mentioned earlier that in their review, Chun and Sung (1996) reported normal unforced  $X_R/h$  values between 6.0 and 8.2 for aspect ratios ranging from 12 to

30.5. All of these aspect ratio values were higher than the accepted value of 10 (de Brederode and Bradshaw, 1972) to ensure two-dimensionality, but our value of  $AR = 8.25$  was not. Therefore, we suspect that our aspect ratio could have contributed to our unusual baseline reattachment length. It should be noted that Kang and Choi (2002) observed a value of  $X_{Ro}/h = 6.2$  in their numerical studies for an  $AR = 4$ , which is within the previously stated normal range. However, there remains no experimental evidence to refute our idea of aspect ratio influence.

As was previously mentioned, inlet conditions were also identified as a major contributing factor to variations in  $X_R/h$  values; particularly the inlet  $\delta/h$  and  $\theta$  values, and the inlet boundary layer quality. Unfortunately, no measurements of the inlet conditions (i.e. velocity profile, turbulence intensities, or boundary layer qualities) were made for the preliminary results presented in this section. However, we have tentatively discounted turbulence intensity of the free stream as a major contributing factor based on the measurement (without the step in the tunnel) made by Gilbert (2007). Although it is known that increasing free stream turbulence for a given flow tends to shorten the separation bubbles (Hillier and Cherry, 1981), our value of free stream turbulence intensity was measured by Gilbert (2007) to be less than 1%. Hillier and Cherry (1981) tested turbulence intensities ranging from 1.8% to 7.2%, and did not observe reductions in negative coefficient of pressure values significant enough to explain our  $X_{Ro}/h$  value for their low turbulence intensities. Further, Isomoto and Honami (1989) tested the effects of inlet turbulence intensity on the reattachment length of a backward-facing step flow, and found that an increase in turbulence intensity from 0.25% to 1.3% only produced a  $0.1h$  change in  $X_R$  (which was also the value of their experimental error in  $X_R$  measurement). We can therefore discount inlet turbulence intensity as a contributing factor to our unusual  $X_{Ro}$  value, leaving only our non-2D aspect ratio and inlet boundary layer conditions as possible explaining factors.

The current experimental system could be adapted to use a hydrogen bubble wire to measure inflow boundary layer qualities, but this flow visualization tool was not available for any of the initial experiments discussed in this thesis. Therefore, we can neither confirm nor refute that our boundary layer qualities (laminar/turbulent,  $\theta$ ,  $\delta/h$ ) had any impact on the baseline reattachment length. However, it is interesting to note that Adams and Johnston (1988b) found that BFS flows with laminar upstream boundary layers had  $X_{Ro}$  values that were 30% shorter than those of turbulent flows. It is possible that our boundary layer was laminar for our values of  $Re_h$ , and that the widely accepted  $X_{Ro} \approx 7h$  value is only true for flows with turbulent boundary layers at the inlet. Future experiments using hydrogen bubble wire or laser particle techniques to determine flow

characteristics at the inlet would be useful in further understanding the relationship between these qualities and the other factors outlined above.

### 5.3 Two-Dimensional Forcing

#### 5.3.1 Reattachment vs. Perturbation Amplitude

The results from the reattachment length vs. perturbation amplitude experiments (Section 4.3.3.1) are shown in Figure 5.2. This figure plots the effects of perturbation velocity variation (for 2D forcing, at our predicted optimal  $St_h$ ) on the reductions in reattachment length as a fraction of the unforced value ( $X_R/X_{R0}$ ). The chart includes unforced data ( $u'/U_\infty = 0$ ) from the Reynolds number dependence test as well. Note, again, that this experiment occurred at  $Re_h = 24500$ .

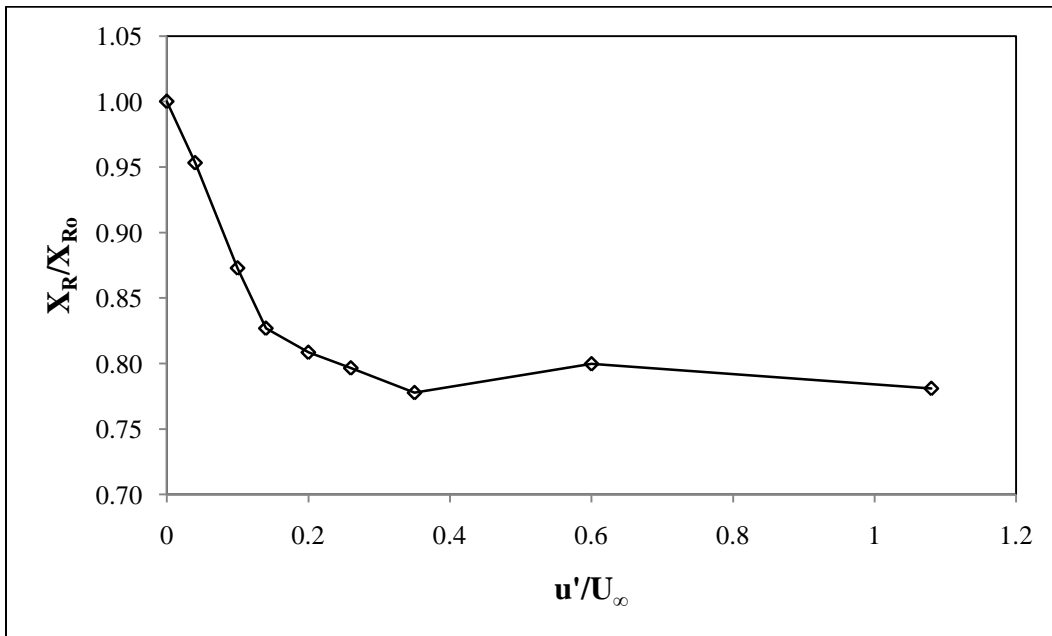


**Figure 5.2** The effect of forcing amplitude on the reattachment length, for 2D forcing at our predicted optimal  $St_h = 0.3$ .

Our time-averaged reattachment length was most sensitive to amplitude changes in the range of  $u'/U_\infty = 0$  to  $u'/U_\infty = 0.14$ . By approximately  $u'/U_\infty = 0.35$ , the forcing had become completely saturated for  $St_h = 0.3$ ; i.e. additional increases in  $u'/U_\infty$  did not further reduce the reattachment length. At this forcing amplitude, the time-averaged reattachment length was reduced to 77% of the unforced value. The slight increase at  $u'/U_\infty = 0.6$  was deemed to be within experimental error ( $\pm 0.1h$ ), and was not considered a significant result.

The only other results for an experiment of this nature available in literature were those of Henning and King (2007). Our results differed from theirs in terms of the perturbation velocities required to produce saturation. Henning and King's maximum reduction in reattachment length was achieved by  $u'/U_\infty = 0.1$  (with values up to  $u'/U_\infty = 0.15$  tested), with their zone of maximum sensitivity occurring between  $u'/U_\infty = 0$  and  $u'/U_\infty = 0.05$ . Their maximum reduction in reattachment length (30%) was also slightly higher than ours (23%) for this case, although the results were certainly in the same realm keeping in mind that Henning and King (2007) had a longer  $X_{R0}/h$  to begin with. We also produced higher reductions in both average reattachment length and local reattachment length in other experiments; these results will be outlined in subsequent sections.

### 5.3.2 Reattachment vs. Strouhal Number

#### 5.3.2.1 High Reynolds Number

Figure 5.3 plots the time-averaged results of our reattachment length vs. Strouhal number experiments outlined in Section 4.3.3.2. Again, these experiments were performed at our high Reynolds number  $Re_h = 24500$ , forcing uniformly across the span of the step. The results for the four perturbation amplitudes from Section 5.3.1 are plotted.

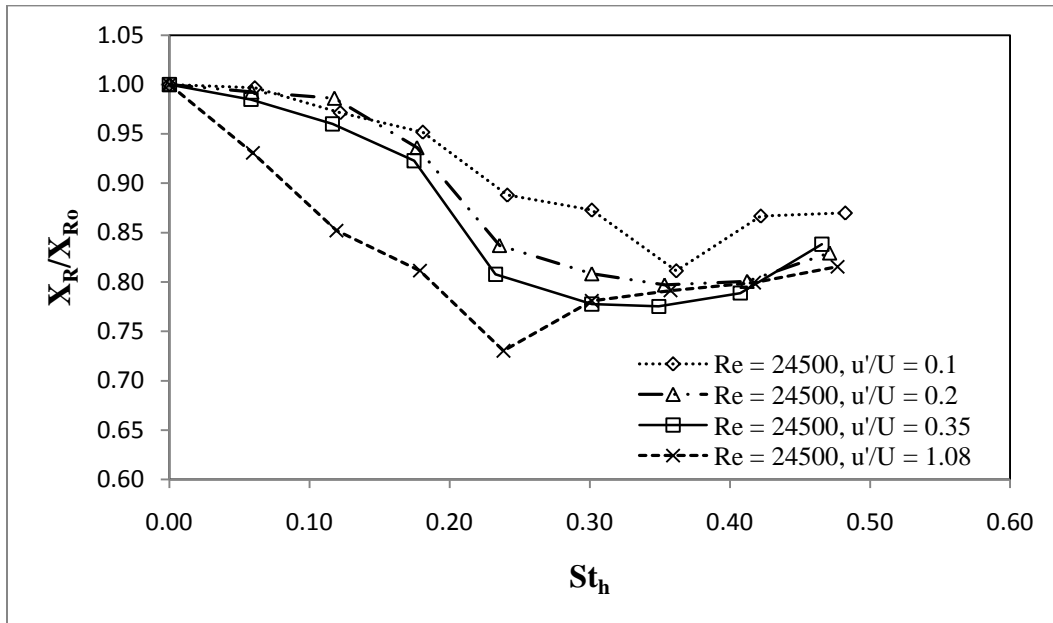


**Figure 5.3** The normalized reattachment length plotted as a function of the step height Strouhal number, for four values of 2D perturbation velocity at  $Re_h = 24500$ .

In general, each of the four curves behaved in a manner consistent with previous studies; as the forcing frequency was increased, reduction in reattachment

occurred until the optimal  $St_h$  number (or range thereof) was reached. Any subsequent increase in forcing frequency after this value resulted in less reattachment reduction. There were, however, some unusual results obtained from this experiment.

When we forced the flow with an amplitude of  $u'/U_\infty = 0.1$ , a minimum in  $X_R/X_{Ro}$  occurred at  $St_h = 0.36$ . The same curve shape occurred for  $u'/U_\infty = 1.08$ , although  $St_h = 0.24$  was the optimal Strouhal number in this case. When compared to the  $u'/U_\infty = 0.2$  and  $u'/U_\infty = 0.35$  curves, the ranges of maximum reattachment reduction for the  $u'/U_\infty = 0.1$  and  $u'/U_\infty = 1.08$  curves seem small. It could be that reductions in reattachment length are more sensitive to changes in Strouhal number when forcing at amplitudes lower ( $u'/U_\infty = 0.1$ ) or much higher ( $u'/U_\infty = 1.08$ ) than the saturation amplitude ( $u'/U_\infty = 0.35$ ). The appearances of these small Strouhal ranges were consistent with the results of Chun and Sung (1996), and Chun et al. (1999), although their optimal value of  $St_h = 0.27$  was consistent for all of their three amplitude curves. These results could also indicate problems with our forcing fidelity at amplitudes much higher or lower than those corresponding to optimal operating characteristics of our actuators.

Our  $u'/U_\infty = 0.2$  and  $u'/U_\infty = 0.35$  curves were more similar to the findings of Henning and King (2007); rather than the previously described narrow  $St_h$  ranges, they observed wider optimal ranges of Strouhal numbers that produced similar reductions in reattachment length. In our case, Strouhal numbers ranging from  $0.3 \leq St_h \leq 0.41$  produced maximum reductions in reattachment length for both the  $u'/U_\infty = 0.2$  and the  $u'/U_\infty = 0.35$  curves. Henning and King (2007) also reported consistent optimal  $St_h$  ranges between different amplitudes.

The results outlined in the previous two paragraphs led us to another interesting finding: our optimal Strouhal numbers seemed to be amplitude dependent. As  $u'/U_\infty$  values increased, the optimal  $St_h$  values generally decreased. The hypothesis of a consistent optimal Strouhal number (or range thereof) at different perturbation amplitudes (as observed by Chun and Sung, 1996; and Henning and King, 2007) did not hold for our 2D forcing experiments. Instead, we observed an optimal Strouhal range ( $0.3 \leq St_h \leq 0.41$ ), but only for perturbation velocity amplitudes that were close to the saturation value of  $u'/U_\infty$  from Section 5.3.1 (i.e.  $u'/U_\infty = 0.2$  and  $u'/U_\infty = 0.35$ ). Forcing amplitude dependence was also observed by Sigurdson (1995) for his cylindrical bluff body, although he observed *increasing* optimal  $St_h$  values with increasing perturbation amplitudes. This oppositeness between Sigurdson's results and ours indicates that an alternate mechanism causes this phenomenon for our geometry. For instance, in our case increasing  $u'/U_\infty$  could lead to an increase in the height of the separation bubble; whereas for Sigurdson (1995), an increase in perturbation amplitude led reduced

the height of the separation bubble. However, the fact that the only significantly different  $St_h$  value that we obtained was for the  $u'/U_\infty = 1.08$  curve could also indicate that the observed amplitude dependence was an anomaly. In order to verify that this relationship exists, more experiments at different  $u'/U_\infty$  values would be necessary.

As expected, curves with higher  $u'/U_\infty$  values produced greater reductions in reattachment lengths as well. The maximum reductions in time-averaged reattachment lengths for each curve were: 19% for  $u'/U_\infty = 0.1$ , 20% for  $u'/U_\infty = 0.2$ , 22% for  $u'/U_\infty = 0.35$  and 27% for  $u'/U_\infty = 1.08$ . When compared to values of  $X_R/X_{R0}$  from other studies, our 2D forcing slightly outperformed that of Kang & Choi (2002) but did not improve upon the results of Henning and King (2007). A direct comparison of our  $X_R/X_{R0}$  values to those of Chun and Sung (1996) and Chun et al. (1999) was not possible, due to the fact that they defined their forcing amplitude differently. Figure 5.4 summarizes the above comparisons for our  $u'/U_\infty = 0.35$  curve.

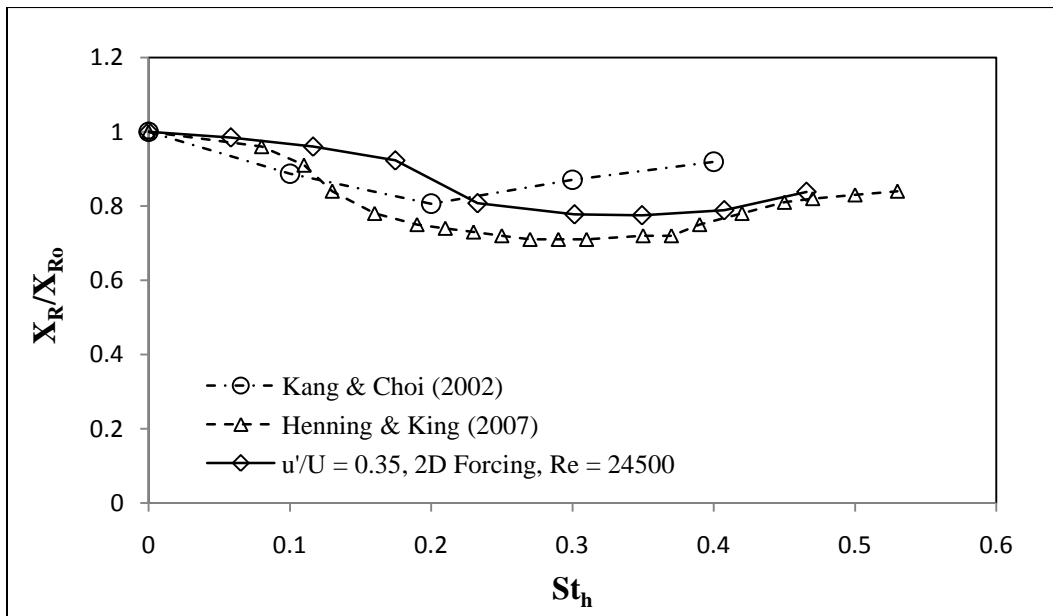


**Figure 5.4** A comparison between the 2D forcing results of Henning and King (2007), the 2D simulation results Kang and Choi (2002), and our 2D forcing at  $u'/U_\infty = 0.35$  and  $Re_h = 24500$ .

The 27% reduction in reattachment ( $X_R/X_{R0} = 0.73$  at  $St_h = 0.2$ ) for the  $u'/U_\infty = 1.08$  curve was somewhat unexpected, as it represented the largest average reduction in reattachment length for any time-averaged run. The reason for this phenomenon is not yet clear. It is possible that forcing at high amplitudes changed the geometry of our flow, although we do not yet know enough about our high amplitude forcing to confirm that this occurred. At the very least, we can say that

the mechanisms involved with high amplitude forcing are more complex and less predictable than those of the low amplitude forcing.

For this perturbation velocity it was also noted that at the highest Strouhal numbers ( $St_h = 0.42$  and  $St_h = 0.48$ ), the servos driving the actuators would overheat and lock up if they were run for too long.

### **5.3.2.2 Low Reynolds Number**

After examining the results from the previous section, it became apparent that a larger  $St_h$  range was necessary if we were to check whether or not our  $X_R/X_{R0}$  returned to unity when forcing at higher frequencies. This phenomenon is a logical consequence of the shear layer's inability to respond to excessively high forcing frequencies, and has been observed by Chun and Sung (1996) for the BFS geometry. In Section 4.3.3.2, we mentioned that a second 2D forcing experiment at  $Re_h = 12450$  was necessary to produce this range of  $St_h$ . The highest frequency that we could safely operate our servos at was 4 Hz (Gilbert, 2007), which was the frequency that produced the maximum value of  $St_h = 0.48$  for the  $Re_h = 24500$  experiments. In order to obtain a higher range of Strouhal numbers ( $St_h = fh/U_\infty$ ), we would have had to either increase the forcing frequency, which was not possible, or lower the free stream velocity, which was what we did. In order to obtain a Strouhal range that was roughly twice as large as that of the  $Re_h = 24500$  experiments, we halved the average free stream throat velocity from  $U_\infty \approx 44$  cm/s to  $U_\infty \approx 22$  cm/s. This free stream throat velocity corresponded to our 'low' Reynolds number of 12540.

Figure 5.5 shows the results of the 2D forcing experiment at  $Re_h = 12450$  (Section 4.3.3.2), with the results of the corresponding high Reynolds number 2D forcing experiment ( $u'/U_\infty = 0.35$ ,  $Re_h = 24500$ ) plotted as well. Note the wider range of Strouhal numbers ( $0 \leq St_h \leq 0.93$ ) tested for the low Reynolds number.

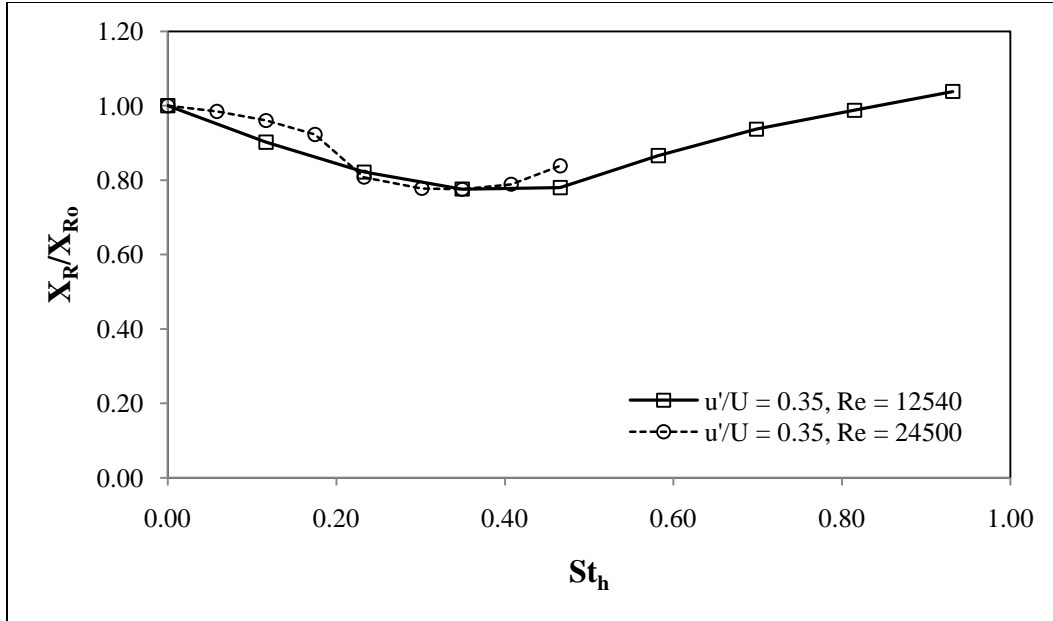


**Figure 5.5** A comparison of the results obtained from the high ( $Re_h = 24500$ ) and low ( $Re_h = 12540$ ) 2D  $X_R/X_{R0}$  vs.  $St_h$  experiments, forcing with  $u'/U_\infty = 0.35$ .

As was true for our  $u'/U_\infty = 0.2$  and  $u'/U_\infty = 0.35$  2D forcing curves from the previous section, a range of Strouhal numbers ( $0.35 \leq St_h \leq 0.47$ ) was seen to affect the maximum reduction in reattachment length ( $X_R/X_{R0} = 0.78$ ). This test produced a 22% reduction in reattachment, which was identical to the 22% reduction produced when forcing with the same amplitude ( $u'/U_\infty = 0.35$ ) at the high Reynolds number (Figure 5.5). This result indicates a certain degree of Reynolds number-independence, but only for Strouhal numbers close to the optimal values.

We also verified that forcing at frequencies greater than the optimum became less and less effective; with the value of  $X_R/X_{R0}$  eventually returning to 1, as with Chun and Sung (1996). At our maximum Strouhal number, the reattachment location overshoot its original value by about 5% ( $X_R/X_{R0} = 1.05$ ). This was also deemed normal; during their experiments, Chun and Sung (1996) tested Strouhal numbers up to 5.0. They also reported  $X_R$  overshooting its original value by 5% for Strouhal numbers greater than 0.9, which they attributed to the inhibition of vortex merging in the downstream stretched vortices.

## 5.4 Three-Dimensional Forcing

### 5.4.1 Reattachment Length vs. Strouhal Number: The High $Re_h$ Case

The results from the high  $Re_h$ , spanwise-varying forcing experiments (Section 4.3.4.2) are presented in Figure 5.6. Curves for  $u'_{rms}/U_\infty = 0.1, 0.2,$  and  $0.35$  are plotted.

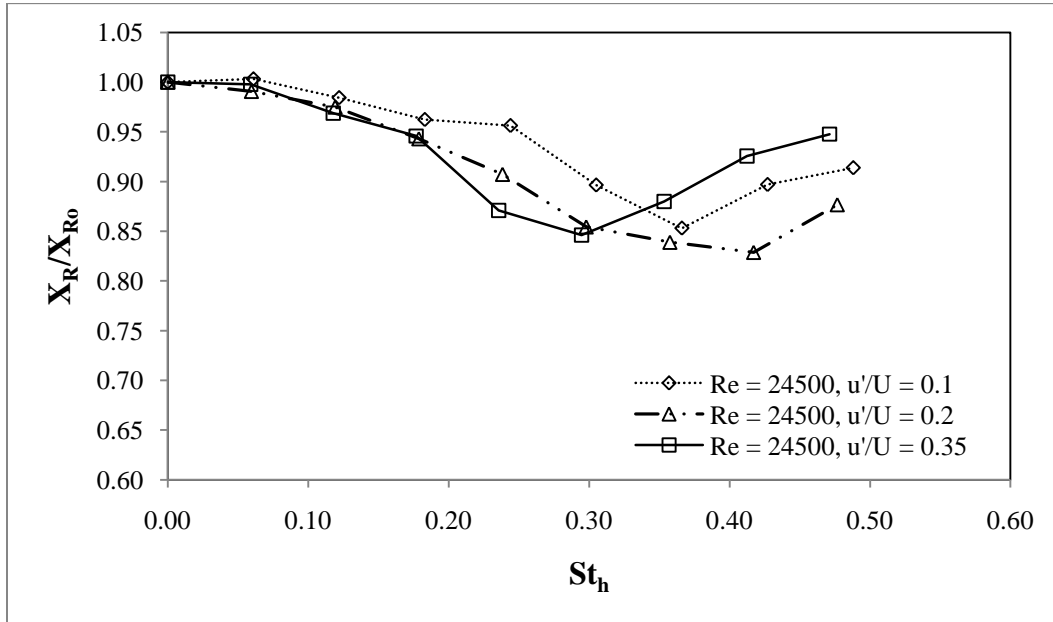


**Figure 5.6** Time-averaged reduction in reattachment length plotted as a function of the step height Strouhal number. Three different 3D perturbation velocity curves ( $u'_{rms}/U_\infty = 0.1, 0.2,$  and  $0.35$ ) are plotted for  $Re_h = 24500$ .

The results obtained from these experiments were substantially more unexpected than those from the 2D cases. In this case, we did not see a general increase in  $X_R$  reduction when perturbation velocity amplitudes were increased. All of our forcing amplitudes produced similar reductions in reattachment lengths.  $X_R$  was reduced by 17% when forcing at  $u'_{rms}/U_\infty = 0.2$ , while the  $u'_{rms}/U_\infty = 0.1$  and  $u'_{rms}/U_\infty = 0.35$  each produced reductions in  $X_R$  of 15%.

The unusual trend in data also appeared in terms of the optimum values of  $St_h$ . In our 2D forcing experiments, the optimal Strouhal numbers (or ranges thereof) were consistent at around  $0.3 \leq St_h \leq 0.41$ ; save for the  $u'/U_\infty = 1.08$  curve. For our 3D experiments we observed optimal Strouhal numbers at  $St_h = 0.37$  ( $u'_{rms}/U_\infty = 0.1$ ),  $St_h = 0.42$  ( $u'_{rms}/U_\infty = 0.2$ ), and  $St_h = 0.29$  ( $u'_{rms}/U_\infty = 0.35$ ). There was no discernible pattern to where the optimal  $St_h$  values occurred; e.g. optimal  $St_h$  values did not increase with increasing  $u'_{rms}/U_\infty$  values, although the optimal

Strouhal values from these experiments did fall within the optimal range observed in Section 5.3.2.1.

Unfortunately, no results for comparison (experimentally determined or numerically simulated) existed in literature at the time of writing. This was due to the uniqueness of the spanwise-varying forcing at a relatively high Reynolds number; the highest turbulent Reynolds number available in literature for 3D forcing was that of the numerical simulations of Kang and Choi (2002). These unusual trends in our 3D forcing results are indicative of the additional complexity of the system's response to 3D forcing. It should also be noted that we elected not to test the highest perturbation amplitude ( $u'/U_\infty = 1.08$ ) from our 2D forcing tests, due to the aforementioned servo overheat/lock up problems.

#### **5.4.2 Reattachment Length vs. Strouhal Number: The Low $Re_h$ Case**

As with our 2D forcing experiments, we opted to run a reduction in reattachment vs. Strouhal number experiment at a lower value of  $Re_h$  in order to obtain a wider range of  $St_h$ . The results from this experiment are presented in Figure 5.7, for  $u'_{rms}/U_\infty = 0.35$ . Also plotted in Figure 5.7 are the results from the corresponding  $Re_h = 24500$  experiment, with  $u'_{rms}/U_\infty = 0.35$ . As for the high  $Re_h$  experiments in the previous section,  $\lambda_z = 4h$ .

As was true for the high  $Re_h$  spanwise-varying forcing experiments from the previous section, we did not observe a wide optimal range of Strouhal numbers. Instead, a minimum of  $X_R/X_{Ro} = 0.79$  was observed at  $St_h = 0.47$ . Although this Strouhal number was outside the optimal range predicted by the high  $Re_h$  tests, it coincided with the upper bound of the optimal range from the low  $Re_h$  2D forcing test ( $0.35 \leq St_h \leq 0.47$ ).

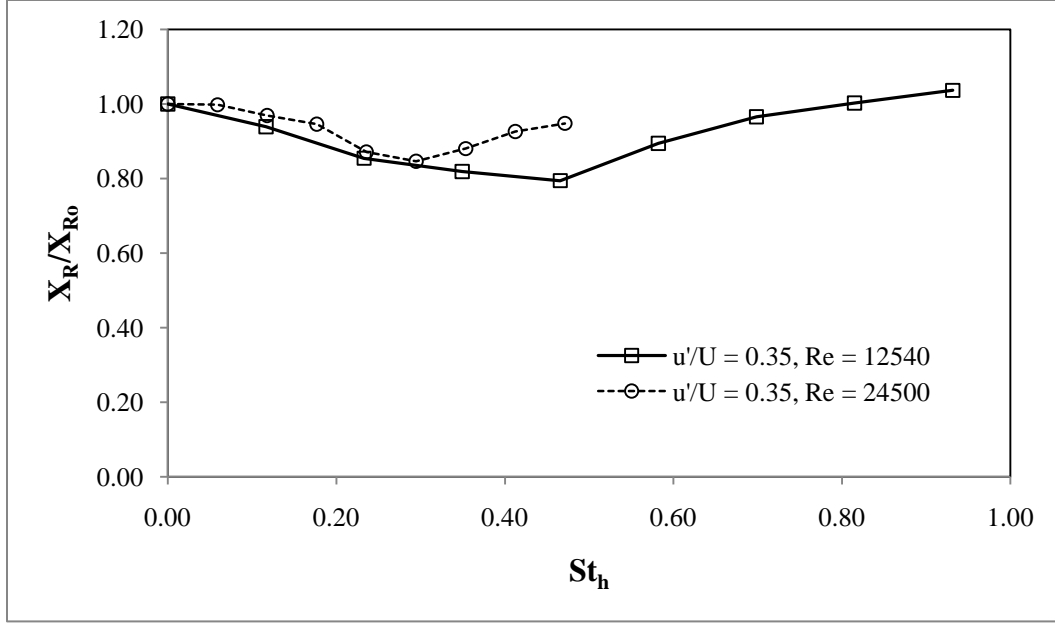


**Figure 5.7** A comparison of the results obtained from the high ( $Re_h = 24500$ ) and low ( $Re_h = 12540$ ) 3D  $X_R/X_{R0}$  vs.  $St_h$  experiments, forcing with  $u'_{rms}/U_\infty = 0.35$  at  $\lambda_z = 4h$ .

The results from this experiment were compared to the results from the numerical simulations of Kang and Choi (2002) described in Section 4.3.4.2, although there were several key differences between our study and theirs. First, our value of  $Re_h = 12450$  was roughly double that of Kang and Choi (2002), and second, our aspect ratio ( $AR \approx 8$ ) was twice their value as well.

Kang and Choi (2002) were able to obtain a maximum reduction in reattachment length of 27% for their best-case numerical spanwise forcing ( $Re_h = 5100$ ,  $St_h = 0.2$ ,  $\lambda_z = 4h$ ,  $AR = 4$ , with a standing single-wave sinusoidal forcing pattern), which represented a 7% improvement on their 2D forcing results. Our maximum reduction in  $X_R$  for our 3D low  $Re_h$  forcing was 21%, which represented no improvement over our 2D low  $Re_h$  forcing, although it was the closest that our 3D forcing came to duplicating the results of our 2D forcing.

## 5.5 Two-Dimensional vs. Three-Dimensional Forcing

### 5.5.1 Effectiveness in Average Reattachment Reduction

In order to gain further insight into the effectiveness of our spanwise-varying forcing, we compared each curve from our 3D forcing  $X_R/X_{R0}$  vs.  $St_h$  to its corresponding 2D counterpart. We performed this comparison for both our high  $Re_h$  case (Figure 5.8), and our low  $Re_h$  case (Figure 5.9). Note that Figure 5.8 does not have a comparison curve for perturbation velocities of  $u'/U_\infty = u'_{rms}/U_\infty =$

1.08, due to the fact that  $u'_{rms}/U_\infty = 1.08$  was not tested during the spanwise-varying experiments.

In terms of maximum reductions in reattachment length, our 2D forcing technique outperformed our 3D forcing technique for every perturbation amplitude at  $Re_h = 24500$ . For  $u'/U_\infty = u'_{rms}/U_\infty = 0.1$ , 2D forcing gave a maximum reduction of the time-averaged reattachment length of 19%, while 3D forcing produced a 15% reduction. A similar result occurred for  $u'/U_\infty = u'_{rms}/U_\infty = 0.2$ , with the 2D forcing yielding a 20%  $X_R$  reduction compared to 17% for 3D forcing. At  $u'/U_\infty = u'_{rms}/U_\infty = 0.35$ , 2D forcing gave a maximum reduction in  $X_R$  of 22% compared to the 15% reduction from 3D forcing.

It was an interesting result that the  $u'/U_\infty = u'_{rms}/U_\infty = 0.1$  forcing produced curves were the same shape (Figure 5.8 (a)). This result indicated that the relatively sharp minima in  $X_R/X_{R0}$  were not coincidental for either case; it could be that in order for forcing to be effective at amplitudes either much greater or much less than the optimum, forcing may need to occur at a very specific frequency. Alternately, these smaller optimal  $St_h$  ranges could indicate problems with the fidelity of our forcing at low amplitudes. Indeed, all forcing amplitudes produced similar curves in both 2D and 3D experiments, which was an encouraging result in terms of the consistency between our experiments.

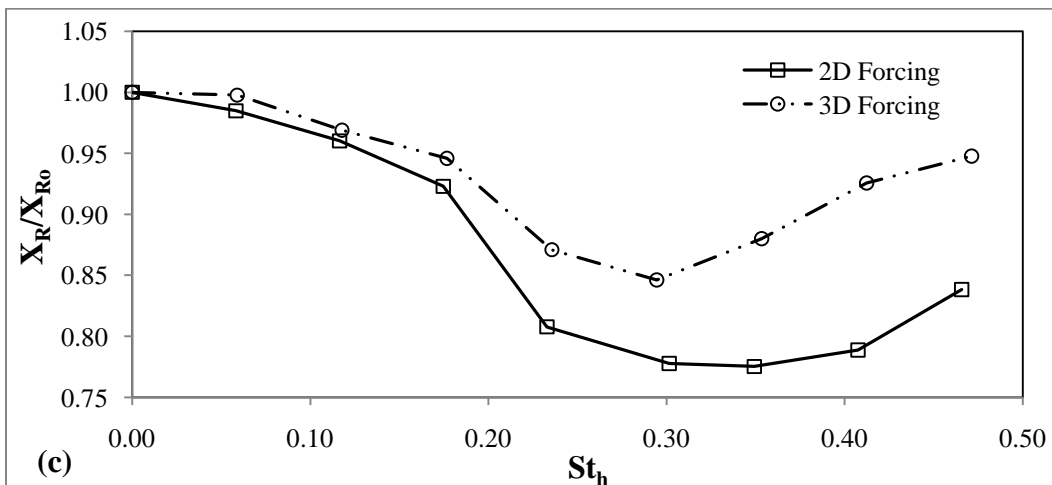
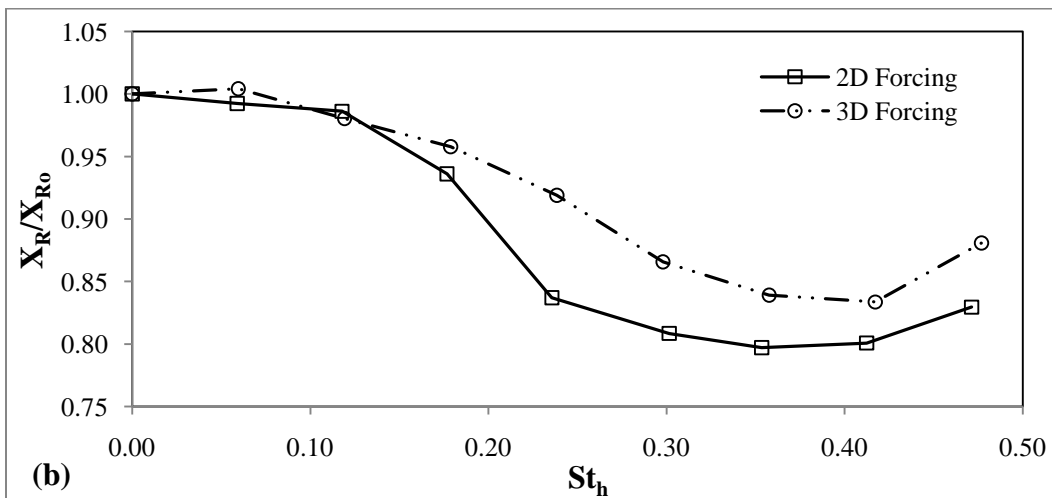
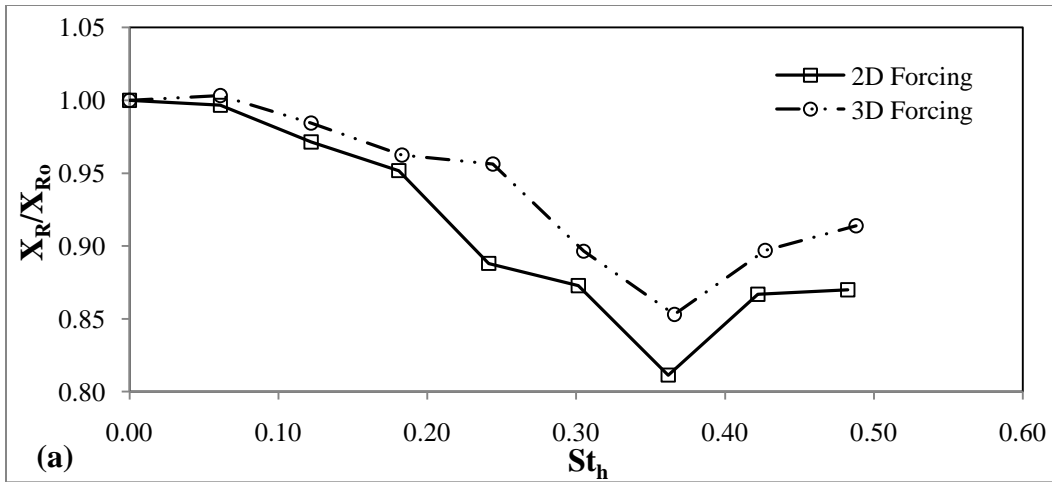
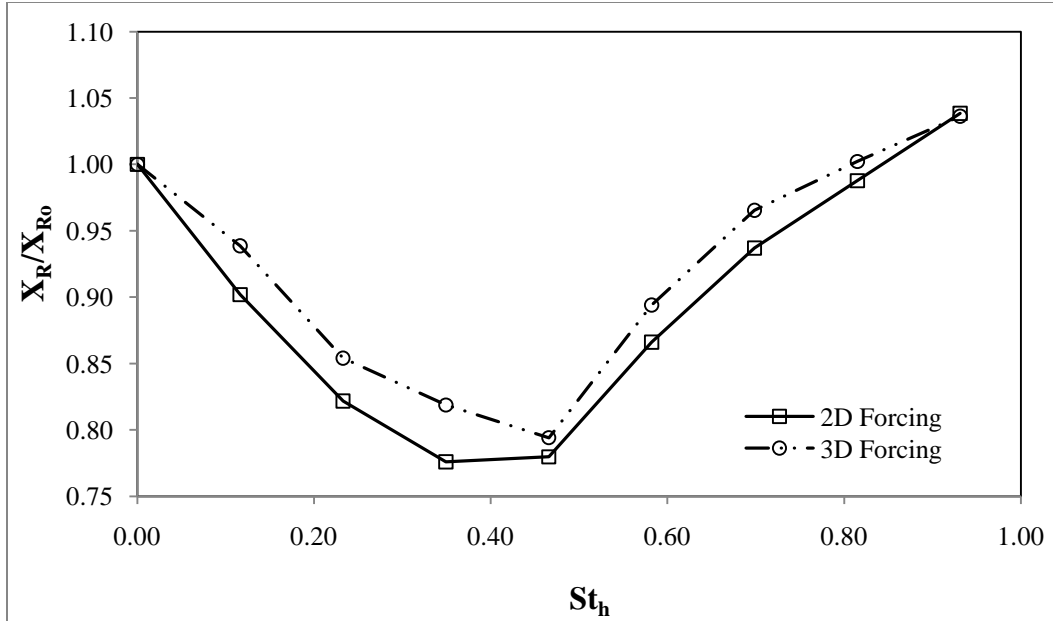


Figure 5.8 A comparison between the 2D and 3D forcing techniques, based on the results of the  $X_R/X_{R0}$  vs.  $St_h$  experiment for  $Re_h = 24500$ . (a) Perturbation amplitudes are 10% of  $U_\infty$ . (b) Perturbation amplitudes are 20% of  $U_\infty$ . (c) Perturbation amplitudes 35% of  $U_\infty$ .



**Figure 5.9** A comparison between the 2D and 3D forcing techniques, based on the results of the  $X_R/X_{R0}$  vs.  $St_h$  experiment for  $Re_h = 12450$ . Perturbation amplitudes are 35% of  $U_\infty$ .

The 2D and 3D forcing experiments at  $Re_h = 12450$  (Figure 5.9) produced the most similar results by far, in terms of both curve shape and the maximum reduction in  $X_R$ . The minima in  $X_R/X_{R0}$  differed by only 1% and the optimal Strouhal numbers were fairly close. From Figure 5.9, it appears that the specific spanwise-varying forcing we chose here worked better at lower Reynolds.

### 5.5.2 Spanwise Variation of Reattachment

A second comparison was made between the 2D and 3D forcing experiments in terms of the spanwise variations in the reattachment lines that each type of forcing produced. Each output data file (with one output data file being produced for each output image) that tuftImgProApp.m created contained coordinate data for an automatically-calculated reattachment line. As with the vector fields, multiple reattachment lines were averaged to obtain a single time-averaged spanwise image of the reattachment line.

Figure 5.10 and Figure 5.11 show these time-averaged reattachment lines for 2D and 3D forcing, respectively. For each figure, a few time-averaged lines are plotted for different experimental run characteristics; the charts would have been far too crowded if data from all experiments were included. If a specific reattachment line from one type of forcing was included in one chart, its corresponding reattachment line was included in the other chart wherever possible. Complete  $X_R/h$  vs.  $z/W_a$  results are contained in Appendix B3. The reattachment location  $X_R/h$  is plotted against the spanwise location  $z$ , normalized

by the width of the actuated span  $W_a$ . Some of the data presented in these figures are interpolated due to the bolt locations; i.e. when reattachment lengths were reduced beyond  $X_R/h \approx 4$ , the reattachment line would cross the bolt location. Because no extraction of tuft data was possible at these locations, a nearest-neighbor interpolation was used in these cases.

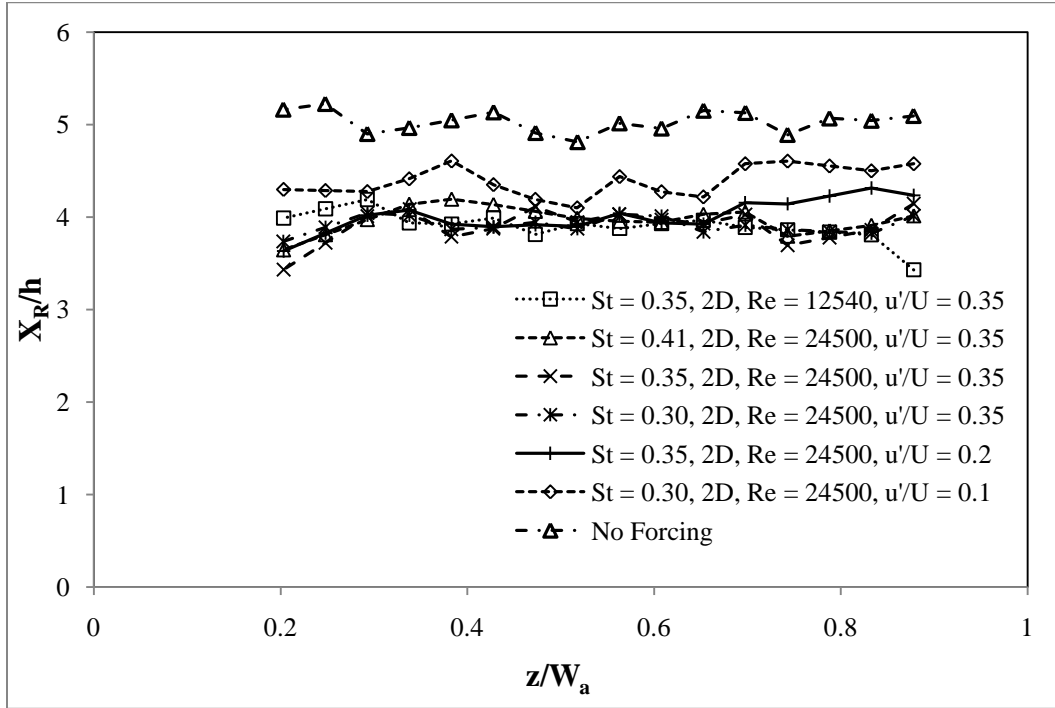


**Figure 5.10** The reattachment variation in the spanwise direction due to 2D forcing for selected experimental run characteristics.

Figure 5.10 indicates that the 3D behaviour of the shear layer at reattachment could indicate the presence of streamwise vortices in the flow, as the unforced reattachment line exhibits what appears to be a non-random periodic waveform that could correspond to some natural 3D instability.

When looking at Figure 5.10 and Figure 5.11, it appears that the reattachment lines are offset toward  $z/W_a = 1$ , or the top wall of the test section. This is an illusion created by the habitual deletion of the left-hand row of tufts by tuftImgProApp.m. Although parts of these tufts were visible in the illuminated raw images, typically not enough of the tufts were showing to perform linear regression vector assignment calculations on them. This was explained by a slight downward bias (i.e. toward  $z/W_a = 0$  in Figure 5.10 and Figure 5.11) of the tufts due to the fact that the tuft material density was very slightly greater than that of the water. Essentially, there should be another data point at  $z/W_a = 0.16$  for each reattachment line in both figures. Unfortunately, it was not possible to fix this problem in programming.

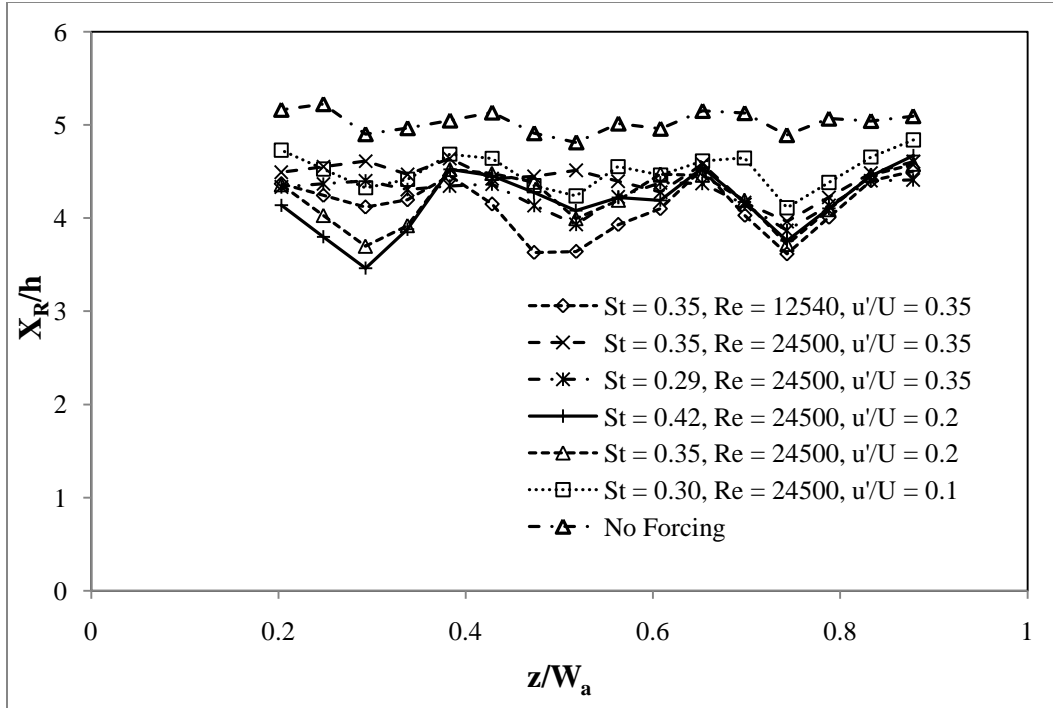


**Figure 5.11** The reattachment variation in the spanwise direction due to 3D forcing for selected experimental run characteristics.

When comparing Figure 5.11 to Figure 5.10, the effects of spanwise-varying forcing become immediately apparent. Although small spanwise fluctuations in  $X_R/h$  existed for the 2D forcing, the spanwise changes in reattachment were much more pronounced when forcing with our standing cosine wave approximation.

For our 3D forcing (Figure 5.11), points of local minima were generally observed at  $z/W_a$  values of approximately 0.25, 0.5, and 0.75 when forcing with characteristics close to the optimal ones from previous sections. For our sine wave centered across the RoboStep's span (Section 4.2), these points corresponded exactly with the locations of maximum forcing amplitude. Conversely, nodes in the forcing corresponded to points of lesser reduction in  $X_R/h$ , although slight reductions in reattachment still remained. This phenomenon was also observed by Henning and King (2007) in their spanwise-varying forcing experiments.

In Section 5.5.1, we stated that spanwise-varying forcing was not as effective as 2D forcing in its ability to reduce the average reattachment lengths. While this statement generally held true, Figure 5.11 illustrated another interesting point: although the average  $X_R/h$  values were not reduced as effectively during 3D forcing, the forcing did produce some points of local spanwise minima that were actually below those of the corresponding 2D forcing curve. For instance, spanwise-varying forcing at  $St_h = 0.35$ ,  $Re_h = 12540$ , and  $u'_{rms}/U_\infty = 0.35$  reduced  $X_R/h$  by as much as 28%, while the  $St_h = 0.42$ ,  $Re_h = 24500$ , and  $u'_{rms}/U_\infty = 0.2$

curve produced a local  $X_R/h$  reduction of 31%. Also, forcing at  $St_h = 0.35$ ,  $Re_h = 24500$ , and  $u'_{rms}/U_\infty = 0.2$  yielded a local reattachment length reduction of 27%. Each of these local reductions in reattachment length were greater than any average  $X_R/h$  reduction that we were able to produce using 2D forcing. These results were encouraging, and provided a reason to further explore the time-varying phase properties of Kang and Choi (2002). They stated that introducing a time-varying phase to the suction-and-blowing profile generated an increased number of inclined vortical structures (in the  $x - z$  plane), which greatly enhanced mixing and reduced reattachment. They used constant phase velocities of  $0.8U_\infty$  and  $1.2U_\infty$ , meaning that the actuation profiles travelled along the span of the step at velocities slightly higher and lower than that of the free stream. If the points of local minima from Figure 5.11 were moving temporally along the span of the RoboStep at a sufficient rate, it may be reasonable to predict that additional mixing would be generated in our case as well, thereby potentially increasing the effectiveness of our 3D forcing.

## 5.6 Dye Visualization Experiments

### 5.6.1 Sample Images and Results

Figure 5.12 (a), (b), and (c) show sample images for the  $Re_h = 12540$  dye visualization experiments. Figure 5.12 (a) gives an accurate representation of an unforced flow at this Reynolds number. Figure 5.12 (b) shows 2D forcing at a Strouhal number of 0.35, with  $u'/U_\infty = 0.35$  as well. Figure 5.12 (c) illustrates a generic result of 3D forcing with  $\lambda_z = 4h$ .

From Figures 5.12 (a) and (b), the presence of a pronounced 3D instability is apparent even in unforced and 2D-forced configurations. An attempt to highlight the natural spanwise wavelength of this instability is given by the dashed white line in Figure 5.12 (b). We can therefore infer that the natural wavelength of the spanwise vortices resulting from the 3D instability is roughly  $3.5h$ , due to the fact that there are just over 2 full waves viewable in the image (and keeping in mind that only  $\sim 70\%$  of the full test section height is illuminated). This estimate for natural wavelength is close to the optimal spanwise forcing  $\lambda_z = 4h$  identified by Kang and Choi (2001) in their numerical simulations; Figure 5.12 (b) may shed some light on why this forcing wavelength was so successful in promoting reattachment length reductions for them.

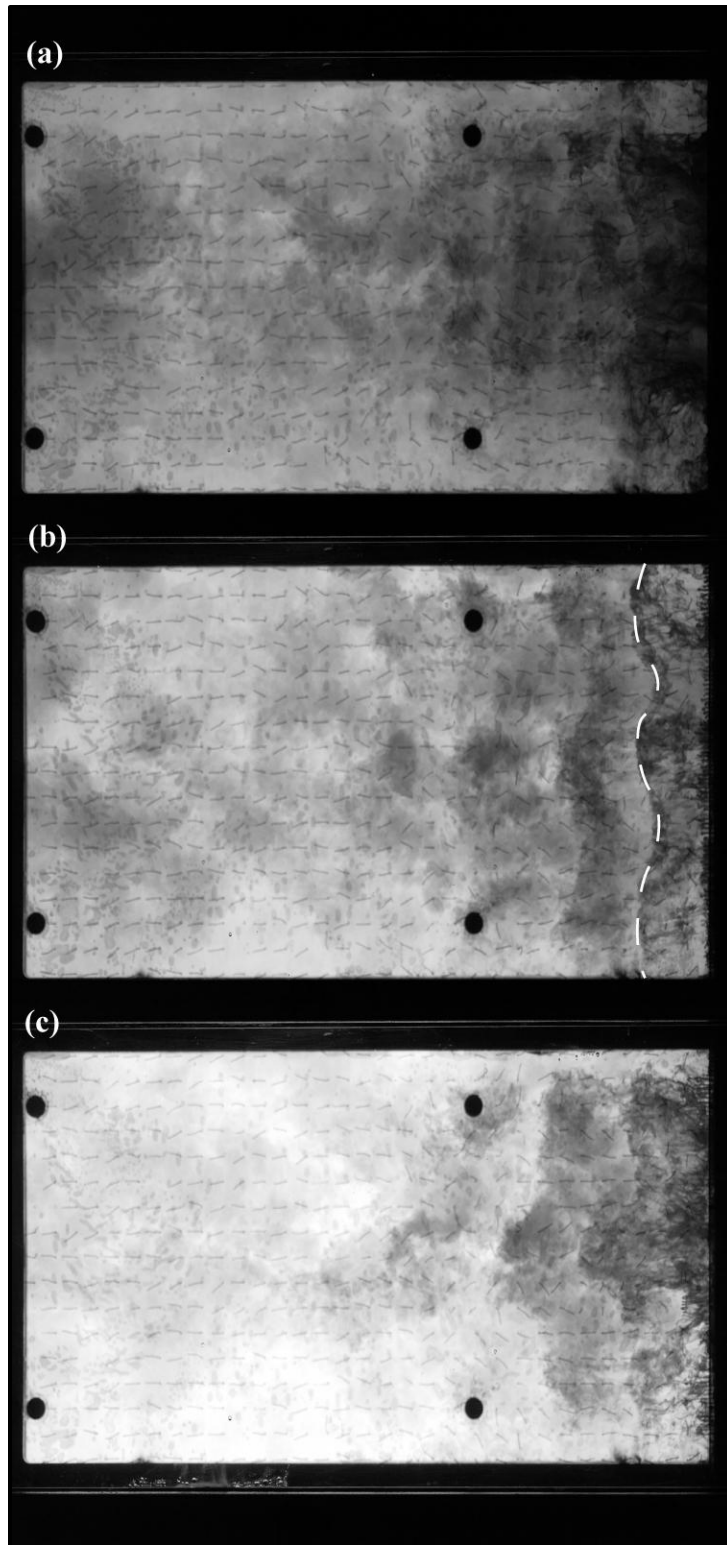


Figure 5.12 Sample photographs from the dye visualization experiments at  $Re_h = 12540$ . For photos with forcing,  $St_h = 0.35$  and  $u'/U_\infty = u'_{rms}/U_\infty = 0.35$ . (a) The unforced case. (b) Uniform spanwise (2D) forcing, with the wavelength of the natural 3D instability highlighted by a dashed white line. (c) Spanwise-varying (3D) forcing at  $\lambda_z = 4h$ .

Referring to both Figure 5.12 and Figure 5.13, note that in the unforced (a) images the dye is sheet-like while in the (b) and (c) forcing images the dye appears to be expelled in individual streamwise streaklines on the scale of the actuation ports. This is due to the fact that in the absence of forcing, the dye moves away from the dye slit due to fluid shear at separation until it is entrained in a roll-up vortex. During forcing, however, the dye is sucked into the actuation ports during the suction phase and then expelled as a jet in the blowing phase. Also, when comparing the  $Re_h = 12540$  and  $Re_h = 2140$  images, it becomes apparent how much more difficult dye visualization is at higher Reynolds numbers due to the immense number of smaller-scale turbulent structures that emerge in high  $Re_h$  flows.

Figure 5.13 (a), (b), and (c) show typical results obtained for the unforced, 2D forced, and 3D forced dye visualization experiments (respectively) for the transitional  $Re_h = 2140$ . For the (b) and (c) images, exaggerated standing-wave forcing profiles are shown in white. Proposed 3D interlocking “chain-link fence” (Sakakibara and Anzai, 2001) vortex structures are highlighted by the white dotted lines. These structures will be explained in greater detail in Section 5.6.2.

These results were obtained by reducing the water tunnel velocity to the point where the separation bubble was just beginning to go turbulent (which was made visible by using dye in the unforced case), and then beginning forcing experiments.

During the forcing experiments, the free stream velocity was checked intermittently by performing time-of-flight measurements on blobs of in the downstream part of the test section, due to the fact that the water tunnel speed seemed to fluctuate slightly at low pump speeds. The velocity values obtained from the time-of-flight measurements were, as always, scaled up to give  $Re_h = 2140$  at the inlet. This Reynolds number value for transition to turbulence agreed very well with  $Re_h = 2000$  (Adams and Johnston, 1988a), but not very well with the value of  $Re_h = 3300$  predicted by Nie and Armaly (2004). This was probably due to the fact that the experimental expansion ratio ( $ER = 1.25$ ) of Adams and Johnston (1988a) was more similar to ours. Although we performed additional transitional Reynolds number experiments forcing at  $St_h \approx 0.15$ , we do not include them in the sample results here.

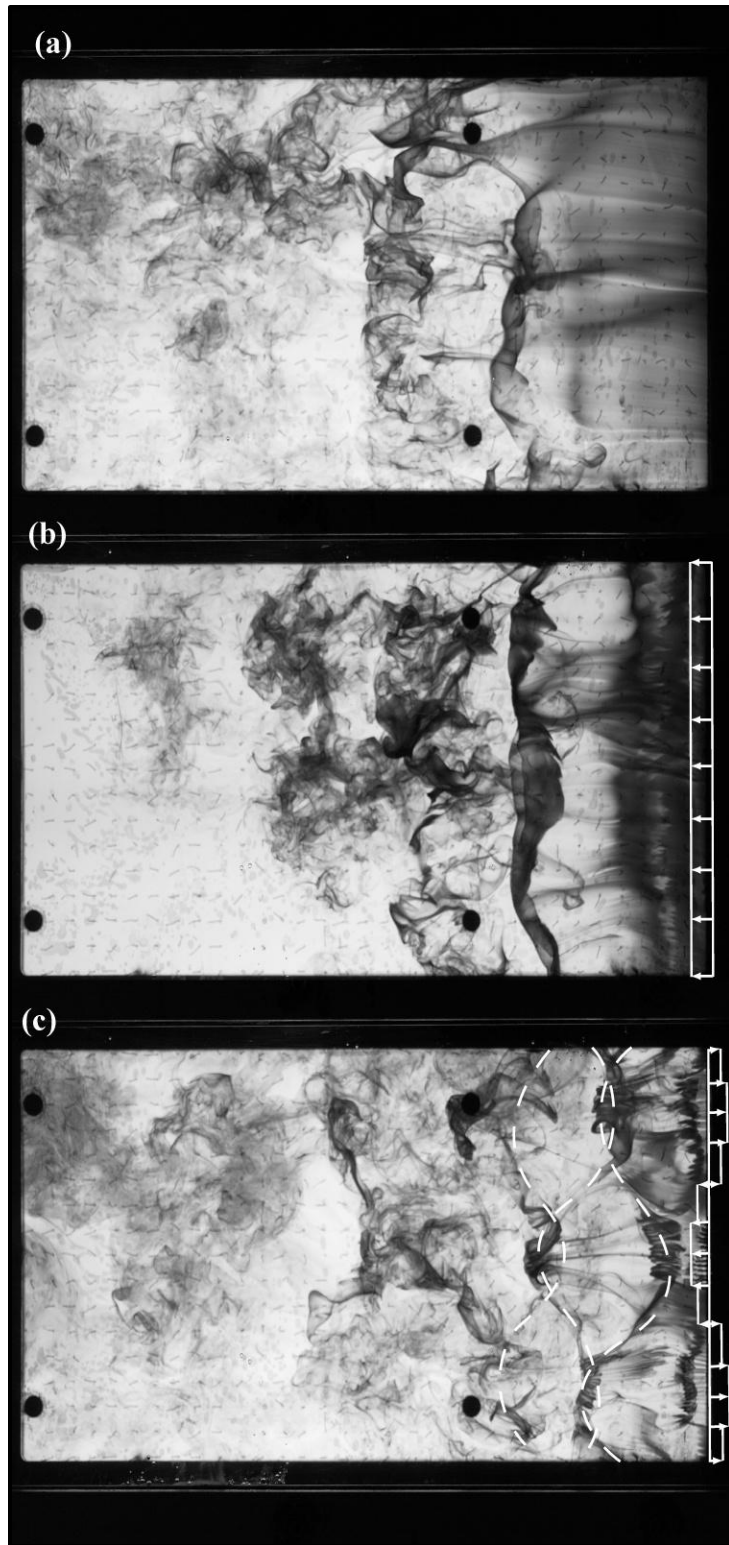


Figure 5.13 Sample dye photographs at the transitional  $Re_h = 2140$ . For photos with forcing,  $St_h = 0.35$  with  $u'$  and  $u'_{rms} \gg U_\infty$ . Forcing profiles (not to scale) are presented in white. (a) The unforced case. (b) Uniform spanwise (2D) forcing. (c) Spanwise-varying (3D) forcing at  $\lambda_z = 4h$ , with possible “chain-link fence” structures highlighted by white dotted lines.

### 5.6.2 Effect of Low $Re_h$ Forcing on the Expected Structures

Any type of forcing in a backward-facing step experiment is typically introduced in hopes of decreasing the reattachment length, which usually indicates an increase in entrainment and mixing through vortex interactions such as pairing. Kang and Choi (2002) hypothesized that the additional vorticity generated by their 3D numerical actuation technique in both the spanwise and streamwise directions would increase mixing more than previous 2D forcing techniques.

Our results, shown partly in Figure 5.13 (b) and (c), seem to agree with the simulations of Kang and Choi (2002) and are notable for two reasons: The first is that it is obviously possible to trigger the roll-up processes of the spanwise vortices during the blowing phase of actuation, as seen by the large spanwise vortex in Figure 5.13 (b). The second is that streamwise vorticity is also amplified by tilting and stretching of the spanwise components during 3D forcing, as seen in Figure 5.13 (c). According to Kang and Choi (2002), this tilting and stretching could be enhanced using spanwise phase movement of the forcing at a constant velocity (as was previously mentioned). By implementing this unique form of actuation, they were able to reduce the reattachment length by 6.5 ~ 9.7% more than the 22%  $X_R$  reduction obtained by their 2D forcing numerical simulations.

Referring again to Figure 5.13 (c), we can see that the tilting and stretching of the large spanwise vortices forms a staggered pattern of interlocking vortex structures  $180^\circ$  out of phase with one another. These structures are highlighted by white dotted lines in the figure, and are similar to the lambda-type vortices of Nygaard and Glezer (1990) and the “chain-link fence” structures of Sakakibara and Anzai (2001). Yanase et al. (2001) also observed similar structures downstream of a backward-facing step, which they termed “rib” structures.

We used open-loop suction-and-blowing actuation at a  $45^\circ$  angle relative to the free stream direction in hopes of increasing mixing behind the step. The selection of the  $45^\circ$  angle was not arbitrary. The  $45^\circ$  forcing angle means that additional transverse vorticity was generated in both the x-z and y-z planes, because a component of the sinusoidal forcing pattern was be projected in each of these planes.

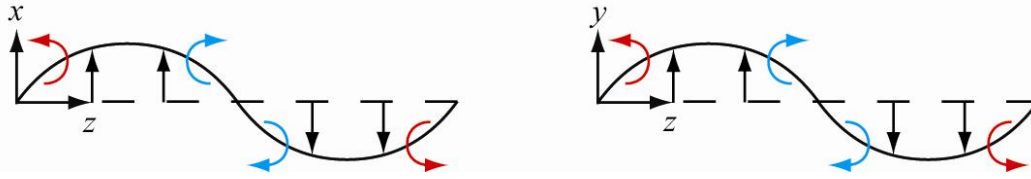


**Figure 5.14** The projected suction-and-blowing actuation velocity profiles in the  $x$ - $z$  (left) and  $y$ - $z$  (right) planes are shown for one wavelength of actuation. The signs of vorticity generation are shown by the counterclockwise (for positive) and clockwise arrows (for negative). The step separation point is represented by a dashed line for both planes.

The left side of Figure 5.14 shows  $\omega_y$  generation resulting from the approximated nonzero  $u$  gradient ( $\partial u/\partial z \neq 0$ ). This vorticity could interact with any “vertical” vortical structures evolving in the wake of the step. Similarly, the right side of Figure 5.14 illustrates the generation of streamwise vorticity ( $\omega_x$ ) due to the fact that  $\partial v/\partial z \neq 0$ .

Due to the location of dye introduction into the flow, we did not visualize most of the predicted structures from Section 2.3, save for the corner vortices immediately downstream of the BFS in the near wall region. These vortices are commonplace for these types of transitional and turbulent flows (Schäfer et al., 2009).

## 6 Conclusions and Proposed Future Work

### 6.1 Summary and Conclusions

We have successfully integrated the design of a single prototype actuator (Gilbert, 2007) into an effective hydraulic forcing mechanism which we have termed the “RoboStep”. The RoboStep promoted growth of the reattaching shear layer in a backward-facing step flow by enhancing mixing in the wake of the step. This system integration involved the construction of 22 such actuators and a LabVIEW program to control them, the design/construction of power and logic grid connections for the actuation array, the design/construction of a system of hydraulic connections and its associated support structure, significant participation in the development of a neutrally buoyant and sufficiently flexible tuft to work in water at low velocities, significant participation in the development of an image processing system to obtain time-averaged flow field information, and the partial design/construction of a dye visualization tool. After the complete apparatus was assembled, several upgrades to the backward-facing step module and actuator prototype (discussed below) were made in order to ensure that the system functioned sufficiently for the research purposes described here.

The RoboStep had a total of 128 actuation ports along its edge, which forced the flow at an angle of  $45^\circ$  relative to the free stream. The drivers for the suction-and-blowing hydraulic forcing utilized by the RoboStep were based largely upon the active control actuation technique employed by Sakakibara and Anzai (2001) in their experiments on a plane jet. The RoboStep is completely unique in terms of the spanwise resolution of actuation profiles that it can provide for a step flow. It can reproduce any periodic waveform that can be symmetrically discretized into 8 or 16 different velocity types, where each of these velocity types would be controlled by a single actuator. The hydraulic connections for each actuation port were made outside of the flow visualization tunnel in which the experiments were performed, so different forcing configurations were possible by simple “plug and play” modifications of the hydraulic connections. These hydraulic connections are the only aspects of the entire current RoboStep system that are not alterable in real-time. A leading edge attachment was constructed for the RoboStep in order to bridge a small gap that existed between the RoboStep and the test section wall.

Each actuator consisted of a servo motor that drove the plunger of a syringe back and forth, using a rack and pinion method of force transmission. In order to reduce the problems of syringe binding and actuator vibrations, and to make the actuators more robust, some modifications were made to the Gilbert prototype. Lock nuts and gasketing were used at the syringe/rack-and-pinion coupling site, to

lessen vibrations within the actuators. Syringe binding was reduced by using a special alignment tool, and by loosening or removing the syringe clamps holding the syringe housings in place. In order to prevent the syringes from rupturing during movement of the actuator board, rectangular tube clamps were developed to do so and also to hold the syringes in place.

A LabVIEW program was developed which allowed real-time control of the actuators, thereby enabling us to perform open-loop control experiments with both uniform (2D) and spanwise-varying (3D) forcing experiments. The 3D forcing experiments were experimental approximations of some of the numerical simulations by Kang and Choi (2002); the 2D forcing experiments had already seen a considerable amount of attention in the literature.

Approximately 1000 of the novel aqueous tufts were placed downstream of the RoboStep in an array to serve as flow visualization tools for determining instantaneous flow field information along the reattachment wall. A MATLAB image processing program was developed to successfully measure the changes in reattachment length resulting from the different forcing patterns that we used. To do so, the program would calculate a vector field for a single backlit image of the tuft plate using a linear regression analysis. Vector fields from multiple images could then be averaged to obtain time-averaged flow field information, with the possibility of performing additional statistical analyses on the averaged data. The results from averages of 50 or more images were compared to visual inspections of the tuft motion – a previously accepted standard of locating the reattachment point.

We used this program to process data obtained from a series of experiments, both with and without forcing. In the first of these experiments, we learned that our average unforced reattachment length ( $X_{Ro}/h = 5.0$ ) was independent of Reynolds number within a turbulent range of  $3770 \leq Re_h \leq 46100$ . This unforced reattachment length is significantly less than those of other experiments ( $6.0 \leq X_{Ro}/h \leq 8.2$ ). We attribute this unusually short value of  $X_{Ro}/h$  to our non-2D aspect ratio and our unknown inlet boundary layer conditions. There is also the possibility that our tufts themselves modified the results of our experiments, due to their ability to move with the flow in any position above the tuft plate (even completely orthogonal to the plate – traditional aerodynamic tufts would always remain parallel to the surface to which they were attached). As a result, the data obtained using the tuft image processing method for determining reattachment should be verified using a separate  $X_R$  calculation method at some point in the future.

Using spanwise-invariant (2D) forcing across the span of the step at the optimal Strouhal number of 0.3 suggested by Sigurdson (1995) and Henning and King (2007), we determined that our forcing became saturated at a perturbation velocity of  $u'/U_\infty = 0.35$  for  $Re_h = 24500$ . We then performed an additional series of 2D forcing experiments for our high and low Reynolds numbers. We tested perturbation velocity amplitudes of  $u'/U_\infty = 0.1, 0.2, 0.35, \text{ and } 1.08$ . In general, increased perturbation velocities produced higher reductions in  $X_R/h$  as expected. For the higher  $Re_h$  case, when forcing two-dimensionally with perturbation amplitudes close to  $u'/U_\infty = 0.35$ , average  $X_R/h$  values were reduced by approximately 20% over an optimal range of  $0.3 \leq St_h \leq 0.41$ . For the lower  $Re_h$  case, we experienced similar reductions in  $X_R/h$  for similar optimal  $St_h$  values.

Following these 2D forcing experiments, we performed a series of complementary 3D forcing experiments at the same two Reynolds numbers. Our forcing pattern approximated a cosine wave (of wavelength  $\lambda_z/h = 4$ ) centered across the RoboStep's span, which imitated the numerical simulations of Kang and Choi (2002) that produced their optimum open-loop forcing results. In fact, our 3D tests were the first experimental reproductions of Kang and Choi's (2002) zero phase velocity simulations.

At the beginning of this thesis, we stated that one of our objectives was to determine whether or not 3D forcing was more effective than 2D forcing in reducing the size of the recirculation bubble. In general, our spanwise-varying forcing experiments were less effective than our spanwise-invariant forcing experiments in terms of the average reductions in reattachment length that they produced. This may be a trend, or it may be that we have simply not found the optimal temporal/spanwise waveform and Strouhal number combination for more effective forcing.

An exception to the generalization above occurred for the low Reynolds number test. In this case, our 3D forcing nearly duplicated the  $X_R/h$  reduction from the 2D experiment, leading us to conclude that our selected 3D forcing at  $\lambda_z/h = 4$  becomes more effective when forcing at lower turbulent Reynolds numbers. Additionally, when forcing three-dimensionally at perturbation amplitudes and Strouhal numbers that were close to the optima, 3D forcing produced local reductions in  $X_R$  (as high as 31%) at various span points ( $z/W_a = 0.25, 0.5, \text{ and } 0.75$ ) that were greater than *any* of the average  $X_R$  reductions produced by 2D forcing. These maximum reductions in reattachment length corresponded to the antinodes of our spanwise forcing profile, i.e. the actuation ports forcing at the highest-amplitude velocity types produced the greatest reductions in  $X_R$ . We can say, therefore, that although we still require a complete port-by-port assessment of our forcing fidelity, the actuation system performed well enough to produce

results that were comparable with previous experimental and numerical studies (Henning and King, 2007; Chun and Sung, 1996; Kang and Choi, 2002). These results must be considered preliminary, because there are indications from the follow-on work of Marc Schostek that the actuators would not always be following the inputted sine wave very well.

In addition to the tuft-based flow visualization technique, we used backlit dye to track the evolution of vorticity in the wake of the backward-facing step. The dye was introduced into the flow through a slit directly below the actuation ports, so that the dye would become entrained in and convected downstream with the large-scale structures (LSS) that formed during flow separation.

The dye experiments at the transitional  $Re_h = 2140$  were successful in producing visualizations of vortex structures that were similar to the ones numerically simulated by Kang and Choi (2002). Both our 2D and 3D forcing types were able to effectively lock-in the formation of spanwise vortices. Our 3D forcing also successfully amplified a 3D instability (most likely the Görtler instability), which created structures in the flow very similar in appearance to the interlocking rib-like structures of Yanase et al. (2001), and also to the structures proposed by Sigurdson and Roshko (1984) and Sigudson (1986).

Perhaps most importantly, in both the high and low Reynolds number dye visualizations we were able to verify that the RoboStep was able to influence the flow in a manner that produced significant observable responses. This result is encouraging when examining the possibilities for future RoboStep forcing experiments, which are outlined in the following section.

## **6.2 Future Work**

### **6.2.1 Proposed Apparatus Improvements**

The primary shortfall of the RoboStep apparatus is that it does not yet have a flow visualization method in place to measure important characteristics at the point of inflow; primarily the boundary layer thickness  $\delta/h$  and momentum thickness  $\theta$ . The RoboStep is upgradeable to incorporate a hydrogen bubble wire to measure these boundary layer quantities, but does not as of yet have the necessary fittings to install the hydrogen wire. The clearance hole for the hydrogen bubble wire is drilled 1.3 step heights upstream of the step's separation edge; when in place, it will provide sheets of pulsed bubbles in the  $x - y$  plane. We would then be able to use the image correlation velocimetry technique of Apps et al. (2003) to determine said boundary layer quantities. Of all of the proposed equipment

improvements, this is by far the most essential upgrade and should be completed before any further data collection.

It would be beneficial to have complete calibrations performed on all of the servos, as it appears that there are small differences in performance between individual servos. As we mentioned earlier in 3.3.7, this was attempted by sampling data directly from the servo potentiometers. After we observed unexpected voltage outputs and unusual signal noise in the acquired potentiometer signals, we concluded that we could not be sure of the data that this technique provided. Most of the calibration data presented in Appendices G1 and G3 were obtained by Marc Schostek using LVDT measurements; a complete characterization of servo performance will be undertaken in his master's thesis. In terms of data acquisition, we have the capability of real time monitoring of all servo positions; for this reason, it would be ideal to have an LVDT for every servo in lieu of our potentiometer data. This upgrade would be costly and may not be entirely necessary; in fact, it may not even be necessary to perform individual calibrations (Schostek, 2010).

Although servos performed well enough to produce reductions in reattachment comparable to those of other studies, an examination of the forcing (Appendices G1 to G3) indicated that improvements to servo performance were still necessary in terms of reducing total harmonic distortion and "clipping" – a term we use to describe the actuation amplitude truncation due to the servo deadband. Unfortunately, the deadband is inherent to this type of servo, and cannot be overcome without a complete replacement of the servo motors.

Marc Schostek also made recommendations for improved servo performance, and had already implemented several of them during the time of writing this thesis. Joining rods were installed to make the servo support L-brackets more rigid, which improved amplitude response of the forcing at high frequencies. The syringe mounting tube clamps (Figure 3.6) were removed completely to alleviate the friction between the plunger and syringe wall. The friction tended to occur as a result of the radial forces applied by the tube clamps. This loosening technique had been used before when tuning the servos, but the complete removal of the tube clamps had never been attempted. The plunger affixing plate (Figure 3.6) was also completely removed, being replaced by double sided foam adhesive tape. In addition to completely eliminating occasional binding problems, the tape coincidentally acted as somewhat of a mechanical filter, removing some of the 50 Hz servo sampling signal noise. The final suggestion made by Marc Schostek (although it has not yet been implemented) was to use smaller syringes than the existing ones. During his recent calibrations (Appendices G1 and G3), Marc Schostek noted that the servos performed worst at low amplitude forcing. He

suggested that smaller syringes could be used to eliminate this problem; for many of the additional low Reynolds number experiments this is seen as an essential upgrade.

As a side note, in Section 5.2 we mentioned that it may be beneficial to remove the debris screen downstream of the RoboStep to test whether or not the blockage has an effect on the unforced flow properties. This is not an essential immediate adjustment, as it would also require that the test section be drained. However, as the experiments in Section 6.2.2.2 would require test section draining regardless, it would be interesting to remove the screen before these experiments and perform a quick unforced re-calibration.

## **6.2.2 Additional Experiments**

### ***6.2.2.1 Low Reynolds Number Testing***

As we mentioned earlier, the spanwise wavelength of the forcing pattern can only be changed by physically altering the hydraulic connections to the actuation ports. Doing so requires draining of the test section, which in turn requires an air purge of all the hydraulic lines upon refilling. In light of this fact, any additional experiments not requiring wavelength modification should be performed prior to those outlined in Section 6.2.2.2.

In Section 5.4.2, we stated that our optimal Strouhal numbers may have a Reynolds number dependence based on the discrepancies between our  $X_R/X_{Ro}$  vs.  $St_h$  results at  $Re_h = 12540$  and  $24500$ . It would be relatively easy to test a wider range of  $Re_h$  values to determine whether or not this is true without altering the state of the equipment. It would be beneficial to test 3D forcing at both lower and higher Reynolds numbers, although based on the results of our high  $Re_h$  tests we may not obtain any useful data at higher Reynolds numbers without a greater knowledge of the turbulence statistics at the inlet. We are not recommending any further 2D forcing at this point in time; our current 2D experiments have already provided repeatable results (Appendix F2) that largely agreed with those of other studies.

These low Reynolds number tests would also enable us to completely test a range of Strouhal numbers from 0 to 5.0, thereby duplicating the experiments of Chun and Sung (1996). Doing so would allow us to see if our reattachment length overshoots the unforced value by 5% at very high Strouhal numbers, as our low  $Re_h$  data hinted at. The only caveat for this test is that it may be necessary to obtain more tuft plate images per data set, or use a different reattachment measurement tool completely. As Reynolds numbers near the transitional range, the tufts become less and less responsive; more are ‘thrown out’ during image

processing due to the criterion outlined in Section 4.4.4.4. More images would give less chance of this happening.

### **6.2.2.2 Additional Wavelengths**

One of the most unique features of the RoboStep design is the controllability of the spanwise wavelength. Although the hydraulic connections must be physically manipulated, the current experimental setup can accommodate spanwise wavelengths  $\lambda_z/h = 0.5, 1, 1.5, 2, 4, 6, 7.5,$  and  $8$ ;  $\lambda_z/h = 3, 5,$  and  $7$  could be incorporated with a small system upgrade (Gilbert, 2007). Gilbert (2007) also notes that for resolutions of both 8 and 16 velocity types per wavelength, we expect our best results in terms of spatial resolution to occur for  $\lambda_z/h \geq 2$ . As was previously mentioned, no experiments to date have been performed with this level of spatial resolution and spanwise variability.

As a starting point, it would be interesting to test  $\lambda_z/h = 8$ , which corresponds to a single wavelength across the span of the step. We suggest this wavelength because although our spanwise wavelength was the same as Kang and Choi's (2002), we had two waves across the span because our aspect ratio was twice as large (compared to their one wave). Although this is not expected to completely account for the differences between our results, it would be interesting to see if the number of standing waves over the span had any influence.

### **6.2.2.3 Time-Varying Phase**

In Section 2.2 we outlined the numerical simulations of Kang and Choi (2002) and the three variations on phase velocity that they tested. To date, we have experimentally tested some of the zero-phase velocity simulations of Kang and Choi (2002), but none of the time-varying phase models. QRP should be omitted from future experiments; not only because it did not produce an additional  $X_R$  reduction compared to their 2D simulations, but also because implementing the scheme in a physical sense (with our current control program) would be extremely difficult. The constant phase velocity, however, would be relatively simple to apply and is expected to improve 2D results by roughly 6% to 10% (Kang and Choi, 2002). Initial experiments would most likely be conducted with constant phase velocities in  $z$  of 80% and 120% of the free stream velocity (Kang and Choi, 2002).

### **6.2.2.4 Multiple Frequency Forcing**

In Section 2.2, we outlined the multiple forcing frequency experiments of (Kim et al. (2007). They found that combinations of the shear layer instability frequency and various subharmonics allowed them to either stabilize the formation or

enhance the pairing of roll up vortices. This would be an interesting set of experiments to attempt to duplicate, especially for dye visualization experiments, but implementing the forcing would require substantial modifications to our current actuator control scheme – much more than the time-varying phase experiments. Also, the 20 ms pulse width sampling rate of the servos would severely limit their ability to force at high frequency subharmonics with adequate resolution. Gilbert (2007) predicted that our actuators would be able to duplicate these experiments for step height Reynolds numbers under 9000 (corresponding to a single frequency actuation  $f = 1.5$  Hz), but the most recent servo performance testing suggests otherwise (Schostek, 2010). For this reason, unless upgrades are made to digital servos with higher temporal sampling resolution, this is not recommended as a future study.

Gilbert (2007) suggests a combination of the forcing techniques of Kang and Choi (2002) and Kim et al. (2007) as the best possible actuation technique:

$$V_{act}(z, t) = A_o \sin \left[ \frac{2\pi}{\lambda_z} (z + z_p(t)) \right] \sum_{n=1}^{N_f} V_{A,peak,n} \sin(2\pi f_n t - \phi_n) \quad (6.1)$$

Here, the actuator would force at a total number of  $N_f$  frequency contents offset by initial phases  $\phi_n$ , which would be the part of the forcing contributed by the techniques of Kim et al. (2007).  $V_{A,peak,n}$  denotes the peak actuation velocity for a given frequency; the harmonic frequency contents would correspond to the shear layer mode of instability, whereas the subharmonics would correspond to the step mode.

The first part of equation 6.1 is adapted from the numerical simulations of Kang and Choi (2002), and is included to provide the spanwise-varying profile of our 3D forcing experiments. The amplitude  $A_o$ , spanwise wavelength  $\lambda_z$  (which Gilbert (2007) calls  $L_z$ ), and time-varying spanwise phase  $z_p(t)$  are the same as those outlined in Section 2.2. Should this type of forcing be implemented, any results produced would be completely unique. No other experimental study exists in the literature that includes forcing with this many frequency contents at this high a spatial resolution.

In light of our belief that the actuator would struggle to duplicate the dual frequency content forcing of Kim et al. (2007), forcing with a higher number of frequencies seems very unlikely. As with the dual frequency forcing, this would require considerable upgrades to our servo motors and control program. For now, it would make better sense to focus first on the additional experiments outlined in Sections 6.2.2.1, 6.2.2.2, and 6.2.2.3.

### ***6.2.2.5 Feedback Control***

As a final suggestion, Gilbert (2007) notes that optimal (Bewley et al., 2001; Henning and King, 2007) and suboptimal (Choi, 1999; Kang and Choi, 2002) control strategies could be implemented in feedback schemes.

As with Gilbert's (2007) proposed ideal forcing technique, feedback schemes would also require significant upgrades to the servos and control program. The most significant problem with implementing feedback methods with our current experimental setup is the inherent time lag involved in processing images of the tuft plate. It currently takes roughly one hour of processing time to obtain an accurate calculation of the reattachment line location, which is far too long for appropriate feedback responses to account for the relatively rapid temporal fluctuations or the reattachment point. Therefore, in addition to the problems that exist for the other forcing techniques from Sections 6.2.2.3 and 6.2.2.4, an entirely new method of reattachment location measurement would have to be implemented for feedback control. As a result, we are not recommending that feedback control methods be attempted in the near future.

## 7 References

Adams, E. W., & Johnston, J. P. (1988a). Effects of the separating shear layer on the reattachment flow structure, part 1: Pressure and turbulence quantities. *Experiments in Fluids*, 6(6), 400-408.

Adams, E. W., & Johnston, J. P. (1988b). Effects of the separating shear layer on the reattachment flow structure, part 2: Reattachment length and wall shear stress. *Experiments in Fluids*, 6(7), 493-499.

Adams, E. W., Johnston, J. P., & Eaton, J. K. (1984). Experiments on the structure of turbulent reattaching flow. Report MD-43. Stanford University, USA.

Apps, C. (2001). A Study of Synthetic Fence Jets Using I.C.V. Master's Thesis, Department of Mechanical Engineering, University of Alberta.

Apps, C. P., Chen, T., & Sigurdson, L. (2003). Image correlation velocimetry applied to discrete smoke-wire streaklines in turbulent pipe flow. *Experiments in Fluids*, 35(3), 288-290.

Armaly, B. F., Durst, F., Pereira, J. C., & Schönung, B. (1983). Experimental and theoretical investigation of backward-facing step flow. *Journal of Fluid Mechanics*, 127, 473-496.

Beaudoin, J., Cadot, O., Aider, J., & Eduardo Wesfreid, J. (2004). Three-dimensional stationary flow over a backward-facing step. *European Journal of Mechanics-B/Fluids*, 23(1), 147-155.

Beaudoin, J., Cadot, O., Aider, J., & Wesfreid, J. (2006). Drag reduction of a bluff body using adaptive control methods. *Physics of Fluids*, 18(8).

Becker, R., Garwon, M., Gutknecht, C., Barwolff, G., & King, R. (2005). Robust control of separated shear flows in simulation and experiment. *Journal of Process Control*, 15(6), 691-700.

Bewley, T., Moin, P., & Temam, R. (2001). DNS-based predictive control of turbulence: an optimal benchmark for feedback algorithms. *Journal of Fluid Mechanics*, 447, 179-225.

Bhattacharjee, S., Scheelke, B., & Troutt, T. R. (1986). Modification of Vortex Interactions in a Reattaching Separated Flow. *AIAA Journal*, 24(4), 623-629.

Breakey, D. (2009). Private Communication.

de Brederode, V., & Bradshaw, P. (1972). Three dimensional flow in normally two dimensional separation bubbles. I.C. Aero Report 72-19. Imperial College, UK.

Choi, H. (1999). Instantaneous control of backward-facing step flows. *Applied Numerical Mathematics*, 31(2), 133-158.

Choi, H., Jeon, W., & Kim, J. (2008). Control of Flow Over a Bluff Body. *Annual Review of Fluid Mechanics*, 40(1), 113-139.

Chun, K., & Sung, H. (1996). Control of turbulent separated flow over a backward-facing step by local forcing. *Experiments in Fluids*, 21(6), 417-426.

Chun, S., Lee, I., & Sung, H. J. (1999). Effect of spanwise-varying local forcing on turbulent separated flow over a backward-facing step. *Experiments in Fluids*, 26(5), 437-440.

Eaton, J. K., & Johnston, J. P. (1981). A review of research on subsonic turbulent flow reattachment. *AIAA Journal*, 19(9), 1093-1100.

Ferrell, M. D. (1991). An analysis of the Bernoulli lift effect as a propulsive component of swimming strokes. Master's Thesis, Department of Education, State University of New York College at Cortland.

Gilbert, S. K. (2007). Unsteady Spatially Varying Flow Control. Master's Thesis, Department of Mechanical Engineering, University of Alberta.

Greenblatt, D., & Wygnanski, I. (2000). The control of flow separation by periodic excitation. *Progress in Aerospace Sciences*, 36, 487-545.

Hasan, M. A. (1992). The flow over a backward-facing step under controlled perturbation: laminar separation. *Journal of Fluid Mechanics*, 238, 73-96.

Henning, L., & King, R. (2007). Robust Multivariable Closed-Loop Control of a Turbulent Backward-Facing Step Flow. *Journal of Aircraft*, 44(1), 201-208.

Hillier, R., & Cherry, N. (1981). The effects of stream turbulence on separation bubbles. *Journal of Wind Engineering and Industrial Aerodynamics*, 8(1-2), 49-58.

Isomoto, K., & Honami, S. (1989). The Effect of Inlet Turbulence Intensity on the Reattachment Process Over a Backward-Facing Step. *Journal of Fluids Engineering*, 111(1), 87.

Kang, S., & Choi, H. (2002). Suboptimal feedback control of turbulent flow over a backward-facing step. *Journal of Fluid Mechanics*, 463, 201-227.

- Kim, S., Choi, H., & Yoo, J. Y. (2007). Effect of local forcing on backward-facing step flow with laminar separation. *Journal of Turbulence*, 8(6), 1-23.
- Lai, J., Yue, J., & Platzer, M. (2002). Control of backward-facing step flow using a flapping foil. *Experiments in Fluids*, 32, 44-54.
- Le, H., Moin, P., & Kim, J. (1997). Direct numerical simulation of turbulent flow over a backward-facing step. *Journal of Fluid Mechanics*, 330, 349-374.
- Lee, I., & Sung, H. J. (2001). Characteristics of wall pressure fluctuations in separated and reattaching flows over a backward-facing step. *Experiments in Fluids*, 30(3), 262-272.
- Lee, I., & Sung, H. J. (2002). Multiple-arrayed pressure measurement for investigation of the unsteady flow structure of a reattaching shear layer. *Journal of Fluid Mechanics*, 463, 377-402.
- Löfdahl, L. (1999). MEMS applications in turbulence and flow control. *Progress in Aerospace Sciences*, 35(2), 101-203.
- Mabey, D. (1972). Analysis and correlation of data on pressure fluctuations in separated flow. *Journal of Aircraft*, 9(9), 642-645.
- Marié, S., & Lambaré, H. (2010). On the unsteady loads induced by the bluff body wake of the Ariane 5 rocket. In *IUTAM Symposium on Bluff Body Wakes and Vortex-Induced Vibrations* (pp. 305-308). Capri, Italy.
- Neumann, J., & Wengle, H. (2003). DNS and LES of Passively Controlled Turbulent Backward-Facing Step Flow. *Flow, Turbulence and Combustion (formerly Applied Scientific Research)*, 71(1-4), 297-310.
- Nie, J., & Armaly, B. (2004). Reverse flow regions in three-dimensional backward-facing step flow. *International Journal of Heat and Mass Transfer*, 47(22), 4713-4720.
- Nygaard, K. J., & Glezer, A. (1990). Core instability of the spanwise vortices in a plane mixing layer. *Physics of Fluids A*, 2(3), 461-464.
- Ötügen, M. (1991). Expansion ratio effects on the separated shear layer and reattachment downstream of a backward-facing step. *Experiments in Fluids*, 10(5), 273-280.
- Park, H., Jeon, W., Choi, H., & Yoo, J. Y. (2007). Mixing enhancement behind a backward-facing step using tabs. *Physics of Fluids*, 19(10), 1-12.

- Rani, H. P., Sheu, T. W., & Tsai, E. S. (2007). Eddy structures in a transitional backward-facing step flow. *Journal of Fluid Mechanics*, 588, 43-58.
- Roos, F. W., & Kegelmann, J. T. (1986). Control of Coherent Structures in Reattaching Laminar and Turbulent Shear Layers. *AIAA Journal*, 24(12), 1956-1963.
- Sakakibara, J., & Anzai, T. (2001). Chain-link-fence structures produced in a plane jet. *Physics of Fluids*, 13(6), 1541-1544.
- Schostek, M. (2009). Private Communication.
- Schostek, M. (2010). Private Communication.
- Schäfer, F., Breuer, M., & Durst, F. (2009). The dynamics of the transitional flow over a backward-facing step. *Journal of Fluid Mechanics*, 623, 85-119.
- Sheu, T. W., & Rani, H. P. (2006). Exploration of vortex dynamics for transitional flows in a three-dimensional backward-facing step channel. *Journal of Fluid Mechanics*, 550, 61-83.
- Sigurdson, L. W. (1986). The structure and control of a turbulent reattaching flow. Doctoral Thesis, Aeronautics Department, California Institute of Technology.
- Sigurdson, L. W. (1995). The structure and control of a turbulent reattaching flow. *Journal of Fluid Mechanics*, 298, 139-165.
- Sigurdson, L. W., & Roshko, A. (1984). The large-scale structure of a turbulent reattaching flow. *Bulletin of the American Physical Society*, 29, 1542.
- Wengle, H., Huppertz, A., Bärwolff, G., & Janke, G. (2001). The manipulated transitional backward-facing step flow: an experimental and direct numerical simulation investigation. *European Journal of Mechanics-B/Fluids*, 20, 25-46.
- Williams, P. T., & Baker, a. J. (1997). Numerical simulations of laminar flow over a 3D backward-facing step. *International Journal for Numerical Methods in Fluids*, 24(11), 1159-1183.
- Yanase, S., Kawahara, G., & Kiyama, H. (2001). Three-Dimensional Vortical Structures of a Backward-Facing Step Flow at Moderate Reynolds Numbers. *Journal of the Physics Society Japan*, 70(12), 3550-3555.
- Yao, S., Krishnamoorthy, C., & Chambers, F. (2007). Experiments on Backward-Facing Step Flows Preceding a Filter. In *ASME JSME 2007 5th Joint Fluids Engineering Conference* (pp. 1179-1189). San Diego, USA.

Yoshioka, S., Obi, S., & Masuda, S. (2001a). Organized vortex motion in periodically perturbed turbulent separated flow over a backward-facing step. *International Journal of Heat and Fluid Flow*, 22(3), 301–307.

Yoshioka, S., Obi, S., & Masuda, S. (2001b). Turbulence statistics of periodically perturbed separated flow over backward-facing step. *International Journal of Heat and Fluid Flow*, 22(4), 393–401.

## 8 Appendices

The following appendices are included to supplement the body of work in a few key areas. We begin this section in Appendix A with details of the pump RPM versus water tunnel velocity re-calibration that was performed after the RoboStep was inserted.

Appendix B provides complete details of the experiments that were visited for the preliminary data presented in this thesis. We split this section into three parts: a complete table of experiments (B1), a second table summarizing the  $X_R$  reduction results from the corresponding experiments (B2), and any additional charts that were produced from these results but were not included in the body of the thesis (B3).

Appendix C includes important equipment operational procedures that should be followed whenever operating the RoboStep apparatus. Appendix C1 focuses on the air bleed procedure that must be performed any time air bubbles appear in the hydraulic forcing lines, while Appendix C2 outlines the basic guidelines for actuator use.

Appendix D summarizes our LabVIEW servo control scheme, including a brief overview of the program (D1) and program usage instructions (D2). Appendix E does the same for our MATLAB image processing program, with the overview and usage instructions in E1 and screen images in E2. Section E1 is comprised of David Breakey's ReadMe.txt file, with permission from the author.

Appendix F outlines some statistical analyses that we performed to determine the number of images that were required for a given data set (F1), and also summarizes some repeatability checks (F2) that we used to check the consistency of our results.

Finally, Appendix G focuses on the fidelity of our forcing, beginning in G1 with a summary of an initial unloaded servo calibration performed by Marc Schostek and David Breakey. Appendix G2 outlines a brief manual calibration of all of the servos to check the variance between individual operational characteristics, followed by a summary of a more detailed calibration performed by Marc Schostek (G3).

## **Appendix A: Tunnel Velocity Calibration – RoboStep In**

This section presents the results from a re-calibration of pump RPM vs. water tunnel velocity that was performed after the RoboStep was inserted into the test section, in order to account for any changes in tunnel velocity due to the additional head loss resulting from the step insertion.

This calibration was performed by using time of flight measurements on blobs of dye added into the free stream approximately 0.8 m downstream of the step's separation edge. For a given pump RPM, the blobs of dye were added after the tunnel velocity had been allowed to settle, and multiple (typically 10) measurements were taken for the time it would take the dye to travel the length of the last half of the test section (75.0 cm exactly). The results from this downstream calibration were then scaled to give inlet velocity and Reynolds number estimates using the expansion ratio of 1.26.

Based on an error analysis of this method, we expect the maximum error in velocity measurements to be  $\pm 8.2$  cm/s at our maximum pump RPM of 56.2. This is a very conservative estimate, as evidenced by the fact the calibration curves all had near-perfect R-squared values. In addition, the maximum error estimates would be far less for lower pump RPM values; i.e. closer to the RPM values of our experiments. In the future, the results from this calibration will be verified using ICV.

Figure 8.1 shows the results of this calibration; curves for downstream velocities and Reynolds numbers, as well as inlet velocities and Reynolds numbers.

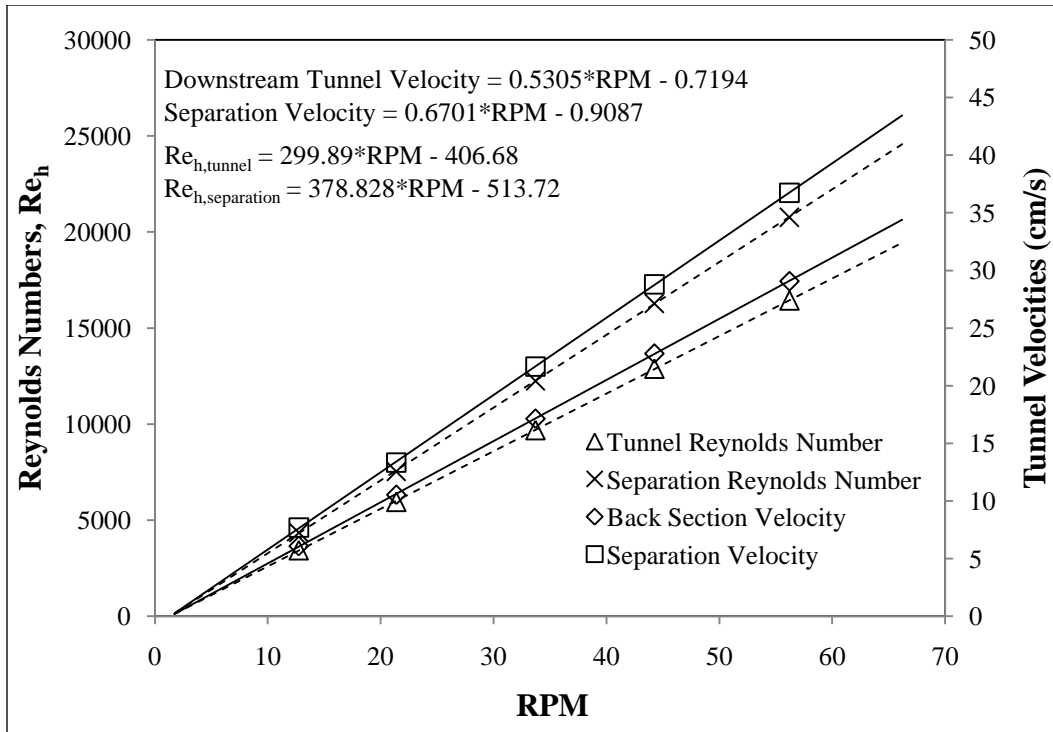


**Figure 8.1** The calibration curves for the velocity testing with the backward-facing step in the water tunnel. Curves and equations are shown for both the inlet and downstream velocities and Reynolds numbers.

## Appendix B: Experiments Visited and Complete Results

### B1: Complete Table of Experiments

Table 8.1 presents a summary of all of the experiments visited, excluding the dye visualizations, which were undertaken to obtain the data presented in this thesis. Note that each cell in the table corresponds to averaged data from at least 50 tuft plate images. The table is split into (a), (b), and (c) parts due to the amount of data presented.

**Table 8.1 (a) Table of experiments, from (1):  $X_R$  vs.  $Re_h$  to (4): 2D Forcing -  $X_R$  vs.  $St_h$  ( $Re_h \approx 24500$ ).**

Test	RPM	$U_{\infty,sep}$ (cm/s)	$Re_h$	$\lambda_z/h$	$u'/U_{\infty}$	F (Hz)	$St_h$
(1) $X_R$ vs. $Re_h$	11.3	6.8	3774	N/A	N/A	N/A	N/A
	22.4	14.3	7983				
	29.6	19.2	10699				
	45.1	29.7	16574				
	65.2	43.3	24192				
	83.9	56.0	31276				
	103.4	69.2	38655				
	123.7	83.0	46099				
(2) 2D - $X_R$ vs. $u'/U_{\infty}$ ( $Re_h \approx 24500$ )	65.2	43.3	24499	N/A	0.04	2.5	0.30
					0.10	2.5	0.30
					0.14	2.5	0.30
					0.20	2.5	0.30
					0.26	2.5	0.30
					0.35	2.5	0.30
					0.60	2.5	0.30
	1.08	2.5	0.30				
(3) 2D - $X_R$ vs. $St_h$ ( $Re_h \approx 24500$ )	64.5	42.8	24499	N/A	0.10	0.5	0.06
	64.5	42.8				1.0	0.12
	65.2	43.3				1.5	0.18
	65.2	43.3				2.0	0.24
	65.2	43.3				2.5	0.30
	65.2	43.3				3.0	0.36
	65.2	43.3				3.5	0.42
	65.2	43.3				4.0	0.48
(4) 2D - $X_R$ vs. $St_h$ ( $Re_h \approx 24500$ )	66.7	44.4	24499	N/A	0.20	0.5	0.06
	66.7	44.4				1.0	0.12
	66.7	44.4				1.5	0.18
	66.7	44.4				2.0	0.24
	65.2	43.3				2.5	0.30
	66.7	44.4				3.0	0.35
	66.7	44.4				3.5	0.41
	66.7	44.4				4.0	0.47

**Table 8.1 (b) Table of experiments, from (5): 2D Forcing -  $X_R$  vs.  $St_h$  ( $Re_h \approx 24500$ ) to (9): 3D Forcing -  $X_R$  vs.  $St_h$  ( $Re_h \approx 24500$ ).**

Test	RPM	$U_{\infty,sep}$ (cm/s)	$Re_h$	$\lambda_z/h$	$u'/U_{\infty}$	f (Hz)	$St_h$
(5) 2D - $X_R$ vs. $St_h$ ( $Re_h \approx 24500$ )	67.5	44.9	24499	N/A	0.35	0.5	0.06
	67.5	44.9				1.0	0.12
	67.5	44.9				1.5	0.17
	67.5	44.9				2.0	0.23
	65.2	43.3				2.5	0.30
	67.5	44.9				3.0	0.35
	67.5	44.9				3.5	0.41
	67.5	44.9				4.0	0.47
(6) 2D - $X_R$ vs. $St_h$ ( $Re_h \approx 24500$ )	66.0	43.8	24499	N/A	1.08	0.5	0.06
	66.0	43.8				1.0	0.12
	66.0	43.8				1.5	0.18
	66.0	43.8				2.0	0.24
	65.2	43.3				2.5	0.30
	66.0	43.8				3.0	0.36
	66.0	43.8				3.5	0.42
	66.0	43.8				4.0	0.48
(7) 2D - $X_R$ vs. $St_h$ ( $Re_h \approx 12540$ )	34.4	22.4	12542	N/A	0.35	0.5	0.12
						1.0	0.23
						1.5	0.35
						2.0	0.47
						2.5	0.58
						3.0	0.70
						3.5	0.81
						4.0	0.93
(8) 3D - $X_R$ vs. $St_h$ ( $Re_h \approx 24500$ )	64.5	42.8	24499	4	0.10	0.5	0.06
						1.0	0.12
						1.5	0.18
						2.0	0.24
						2.5	0.30
						3.0	0.37
						3.5	0.43
						4.0	0.49
(9) 3D - $X_R$ vs. $St_h$ ( $Re_h \approx 24500$ )	66.0	43.8	24499	4	0.20	0.5	0.06
						1.0	0.12
						1.5	0.18
						2.0	0.24
						2.5	0.30
						3.0	0.36
						3.5	0.42
						4.0	0.48

**Table 8.1 (c) Table of experiments, from (10): 3D Forcing -  $X_R$  vs.  $St_h$  ( $Re_h \approx 12540$ ) to (11): 3D Forcing -  $X_R$  vs.  $St_h$  ( $Re_h \approx 12540$ ).**

Test	RPM	$U_{\infty,sep}$ (cm/s)	$Re_h$	$\lambda_z/h$	$u'/U_{\infty}$	f (Hz)	$St_h$
(10) 3D - $X_R$ vs. $St_h$ ( $Re_h \approx 24500$ )	66.7	44.4	24499	4	0.35	0.5	0.06
						1.0	0.12
						1.5	0.18
						2.0	0.24
						2.5	0.29
						3.0	0.35
						3.5	0.41
(11) 3D - $X_R$ vs. $St_h$ ( $Re_h \approx 12540$ )	34.4	22.4	12542	4	0.35	0.5	0.12
						1.0	0.23
						1.5	0.35
						2.0	0.47
						2.5	0.58
						3.0	0.70
						3.5	0.81
	4.0	0.93					

## B2: Complete Table of Results

The corresponding results for the experiments outlined in B1 are tabulated below, according to the “Test” column values in Table 8.2.

**Table 8.2 (a) Table of results, from (1):  $X_R$  vs.  $Re_h$  to (2): 2D Forcing -  $X_R$  vs.  $St_h$  ( $Re_h \approx 24500$ ). Results are shown for each of the 4  $X_R$  calculation methods.**

Test	% Down. $X_R/h$	Unit Norm. $X_R/h$	Non-Norm. $X_R/h$	Eyeballed $X_R/h$
(1) $X_R$ vs. $Re_h$	5.11	5.12	5.07	5.01
	4.97	4.96	5.00	5.01
	5.01	4.98	5.03	5.01
	5.06	5.11	5.10	5.01
	4.88	4.90	4.91	5.01
	5.00	5.04	5.04	5.01
	5.06	5.09	5.08	5.01
	5.17	5.22	5.21	5.01
(2) 2D - $X_R$ vs. $u'/U_{\infty}$ ( $Re_h \approx 24500$ )	4.80	4.80	4.84	4.80
	4.39	4.44	4.44	4.44
	4.16	4.19	4.20	4.25
	4.07	4.13	4.14	4.25
	4.01	4.07	4.05	4.25
	3.91	3.96	3.94	4.25
	4.02	4.08	4.09	4.25
	3.93	3.98	3.95	4.25

**Table 8.2 (b) Table of results, from (3): 2D Forcing -  $X_R$  vs.  $St_h$  ( $Re_h \approx 24500$ ) to (7): 2D Forcing -  $X_R$  vs.  $St_h$  ( $Re_h \approx 12540$ ). Results are shown for each of the 4  $X_R$  calculation methods.**

Test	% Down. $X_R/h$	Unit Norm. $X_R/h$	Non-Norm. $X_R/h$	Eyeballed $X_R/h$
(3) 2D - $X_R$ vs. $St_h$ ( $Re_h \approx 24500$ )	5.01	5.05	5.04	5.01
	4.89	4.89	4.93	5.01
	4.79	4.84	4.83	4.80
	4.47	4.53	4.50	4.63
	4.39	4.44	4.44	4.44
	4.08	4.06	4.08	4.44
	4.36	4.39	4.38	4.63
	4.38	4.46	4.47	4.63
(4) 2D - $X_R$ vs. $St_h$ ( $Re_h \approx 24500$ )	4.99	5.04	5.05	5.01
	4.96	4.95	5.00	5.01
	4.71	4.74	4.74	4.80
	4.21	4.26	4.26	4.44
	4.07	4.13	4.14	4.25
	4.01	4.06	4.05	4.06
	4.03	4.12	4.14	4.25
	4.17	4.16	4.14	4.44
(5) 2D - $X_R$ vs. $St_h$ ( $Re_h \approx 24500$ )	4.95	4.98	5.00	5.01
	4.83	4.85	4.86	4.44
	4.64	4.71	4.68	4.44
	4.06	4.10	4.11	4.25
	3.91	3.96	3.94	4.25
	3.90	3.92	3.94	4.06
	3.97	4.04	4.05	4.25
	4.22	4.24	4.24	4.44
(6) 2D - $X_R$ vs. $St_h$ ( $Re_h \approx 24500$ )	4.68	4.74	4.72	5.01
	4.29	4.32	4.32	4.80
	4.08	4.12	4.14	4.44
	3.67	3.72	3.72	3.86
	3.93	3.98	3.95	3.86
	3.98	4.07	4.06	3.86
	4.02	4.11	4.10	4.25
	4.10	4.14	4.16	4.44
(7) 2D - $X_R$ vs. $St_h$ ( $Re_h \approx 12540$ )	4.54	4.63	4.62	4.63
	4.13	4.20	4.22	4.25
	3.90	4.01	4.00	4.25
	3.92	4.01	4.01	4.06
	4.36	4.41	4.41	4.44
	4.71	4.79	4.76	4.80
	4.97	4.98	4.99	5.01
	5.22	5.25	5.25	5.01

**Table 8.2 (c) Table of results, from (8): 3D Forcing -  $X_R$  vs.  $St_h$  ( $Re_h \approx 24500$ ) to (11): 3D Forcing -  $X_R$  vs.  $St_h$  ( $Re_h \approx 12540$ ). Results are shown for each of the 4  $X_R$  calculation methods.**

Test	% Down. $X_R/h$	Unit Norm. $X_R/h$	Non-Norm. $X_R/h$	Eyeballed $X_R/h$
(8) 3D - $X_R$ vs. $St_h$ ( $Re_h \approx 24500$ )	5.05	5.10	5.08	5.01
	4.95	4.98	4.99	5.01
	4.84	4.88	4.89	5.01
	4.81	4.84	4.84	4.80
	4.51	4.60	4.56	4.44
	4.29	4.35	4.34	4.44
	4.51	4.58	4.56	4.63
	4.60	4.62	4.63	4.80
(9) 3D - $X_R$ vs. $St_h$ ( $Re_h \approx 24500$ )	4.98	5.05	5.03	5.01
	4.90	4.93	4.94	5.01
	4.74	4.82	4.80	4.80
	4.56	4.62	4.61	4.63
	4.30	4.36	4.37	4.25
	4.22	4.22	4.25	4.25
	4.17	4.19	4.22	4.63
	4.41	4.43	4.47	4.80
(10) 3D - $X_R$ vs. $St_h$ ( $Re_h \approx 24500$ )	5.02	5.08	5.08	5.01
	4.87	4.91	4.91	5.01
	4.76	4.82	4.78	4.80
	4.38	4.46	4.45	4.44
	4.26	4.28	4.27	4.44
	4.43	4.46	4.47	4.63
	4.66	4.71	4.68	4.63
	4.77	4.80	4.81	4.80
(11) 3D - $X_R$ vs. $St_h$ ( $Re_h \approx 12540$ )	4.72	4.76	4.74	5.01
	4.30	4.35	4.33	4.44
	4.12	4.13	4.15	4.06
	4.00	4.02	4.03	4.25
	4.50	4.55	4.55	4.63
	4.86	4.90	4.90	4.80
	5.04	5.09	5.06	5.01
	5.21	5.24	5.23	5.01

### **B3: Collection of Generated Charts**

Here, we present every Excel chart that was omitted from the body of the thesis. The first nine charts present all of the time-averaged spanwise reattachment lines for all of the reattachment reduction vs. Strouhal number experiments. Next, we present the data from the reattachment vs. amplitude (one chart) and reattachment vs. Strouhal number (nine charts) tests for all four reattachment calculation methods.

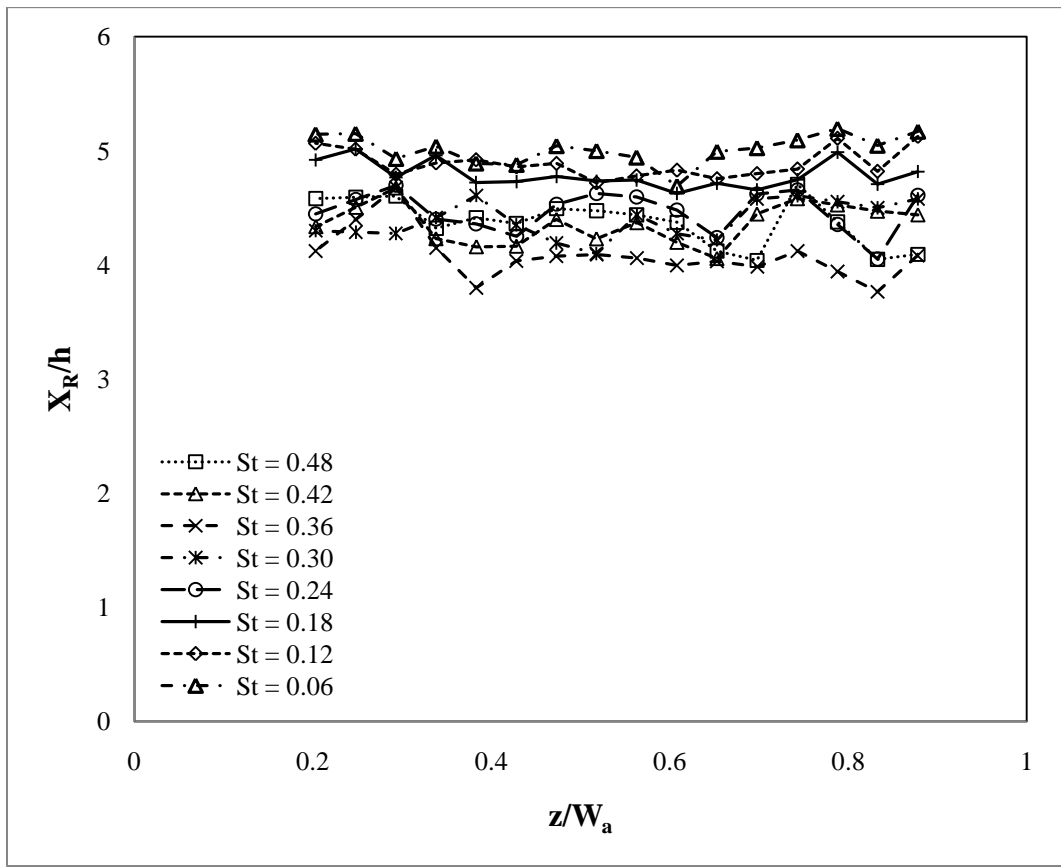


Figure 8.2 Spanwise variation of the reattachment lines for 2D forcing at  $u'/U_\infty = 0.1$ , for  $Re_h = 24500$ .

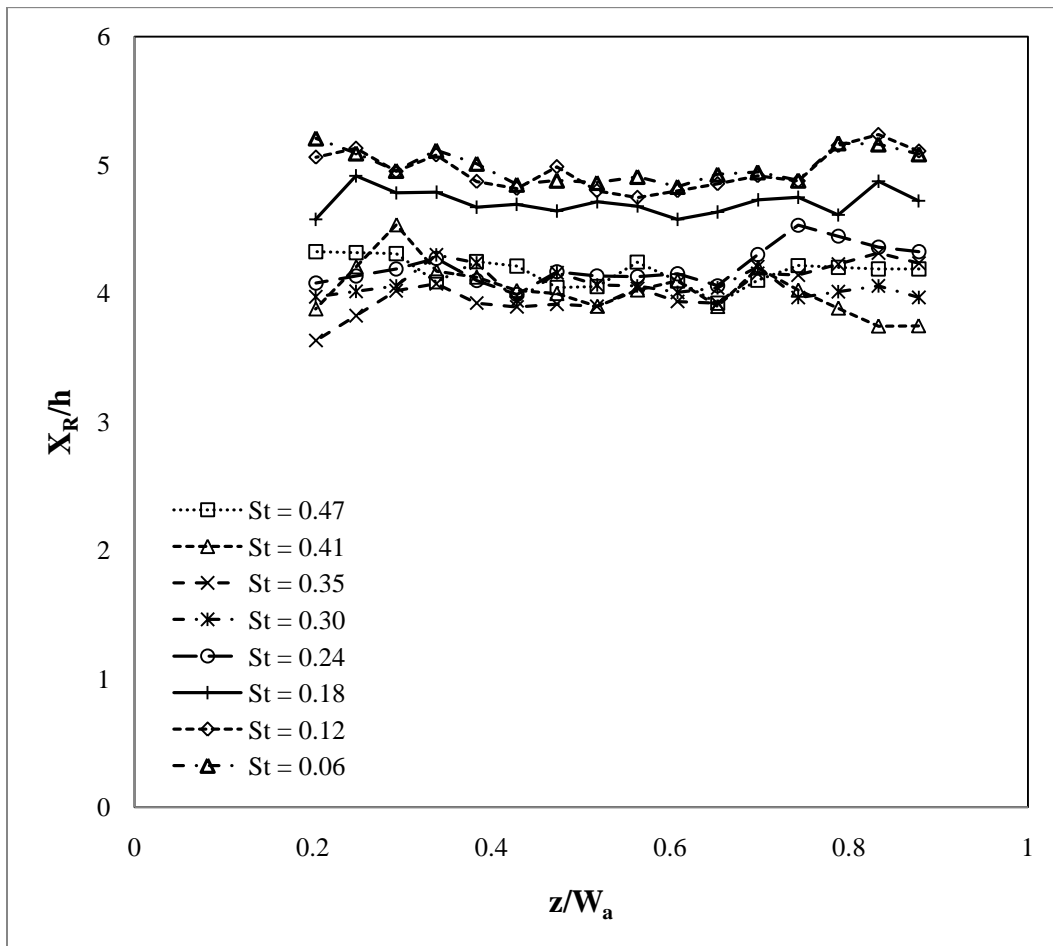


Figure 8.3 Spanwise variation of the reattachment lines for 2D forcing at  $u'/U_\infty = 0.2$ , for  $Re_h = 24500$ .

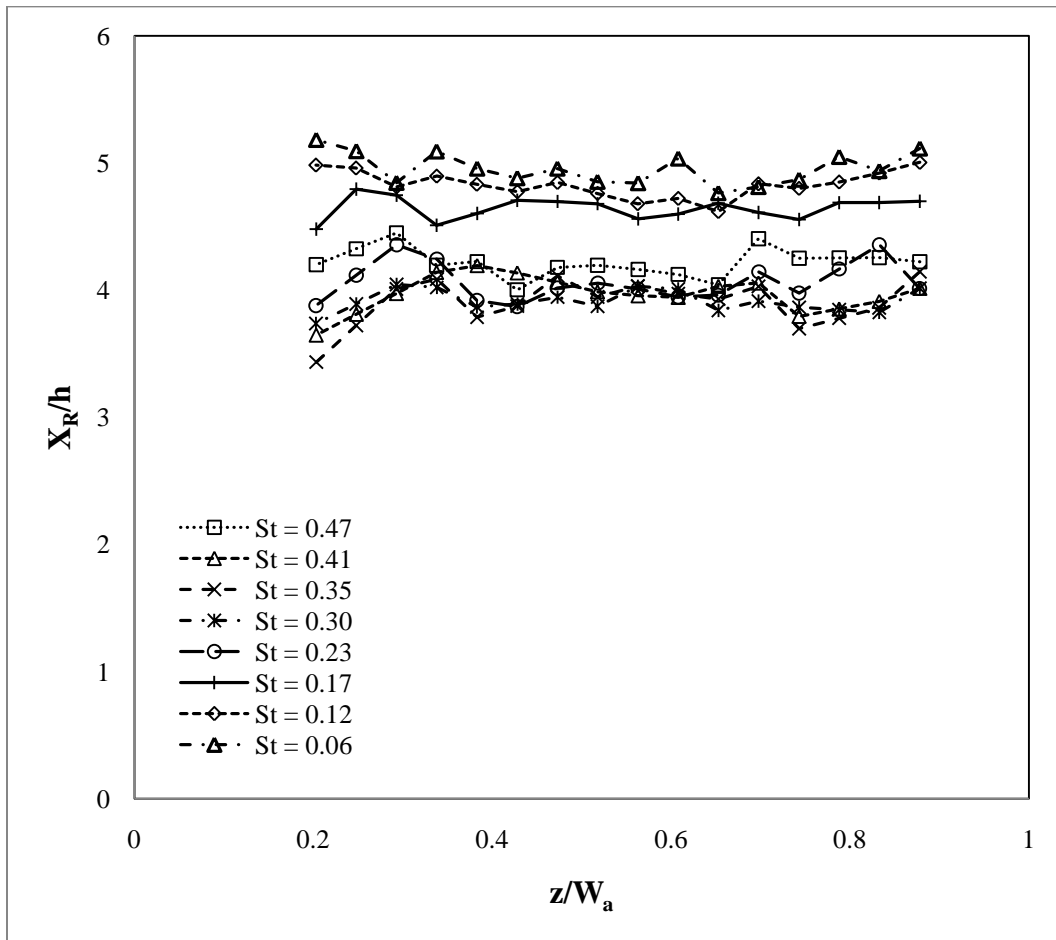


Figure 8.4 Spanwise variation of the reattachment lines for 2D forcing at  $u'/U_\infty = 0.35$ , for  $Re_h = 24500$ .

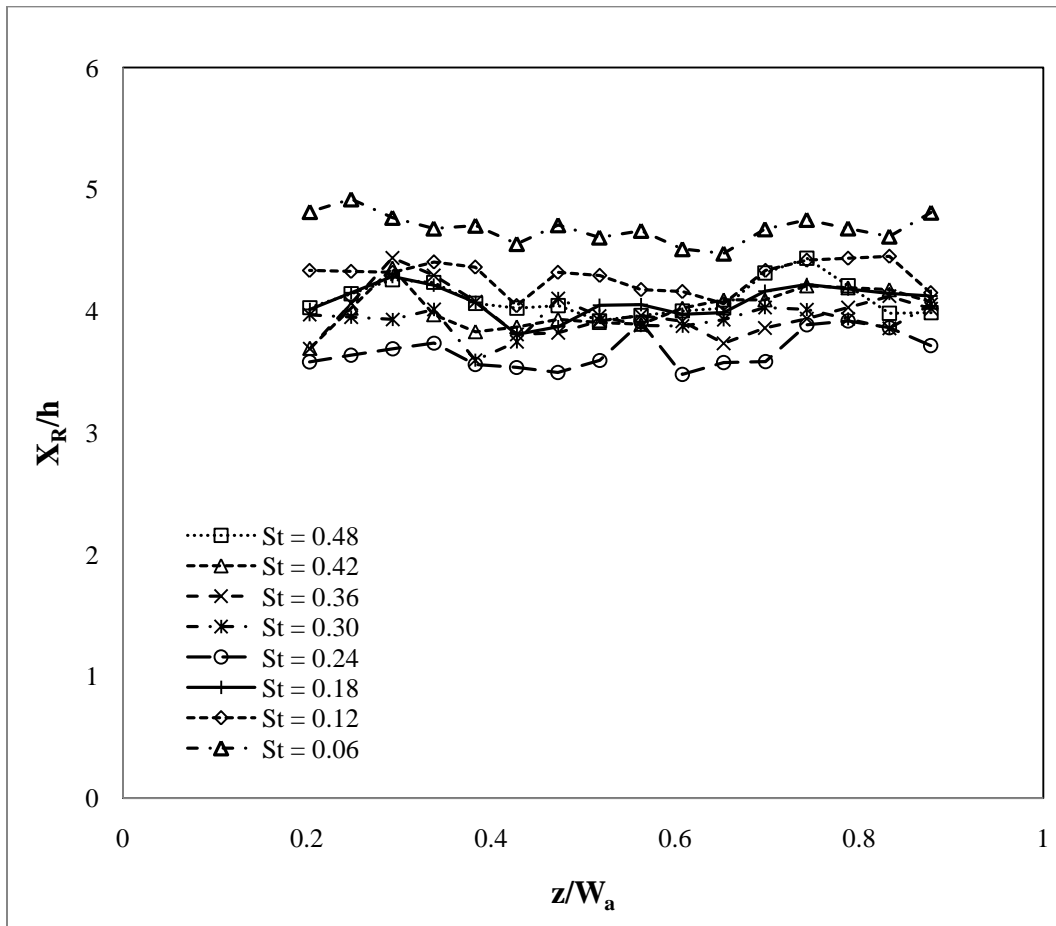


Figure 8.5 Spanwise variation of the reattachment lines for 2D forcing at  $u'/U_\infty = 1.08$ , for  $Re_h = 24500$ .

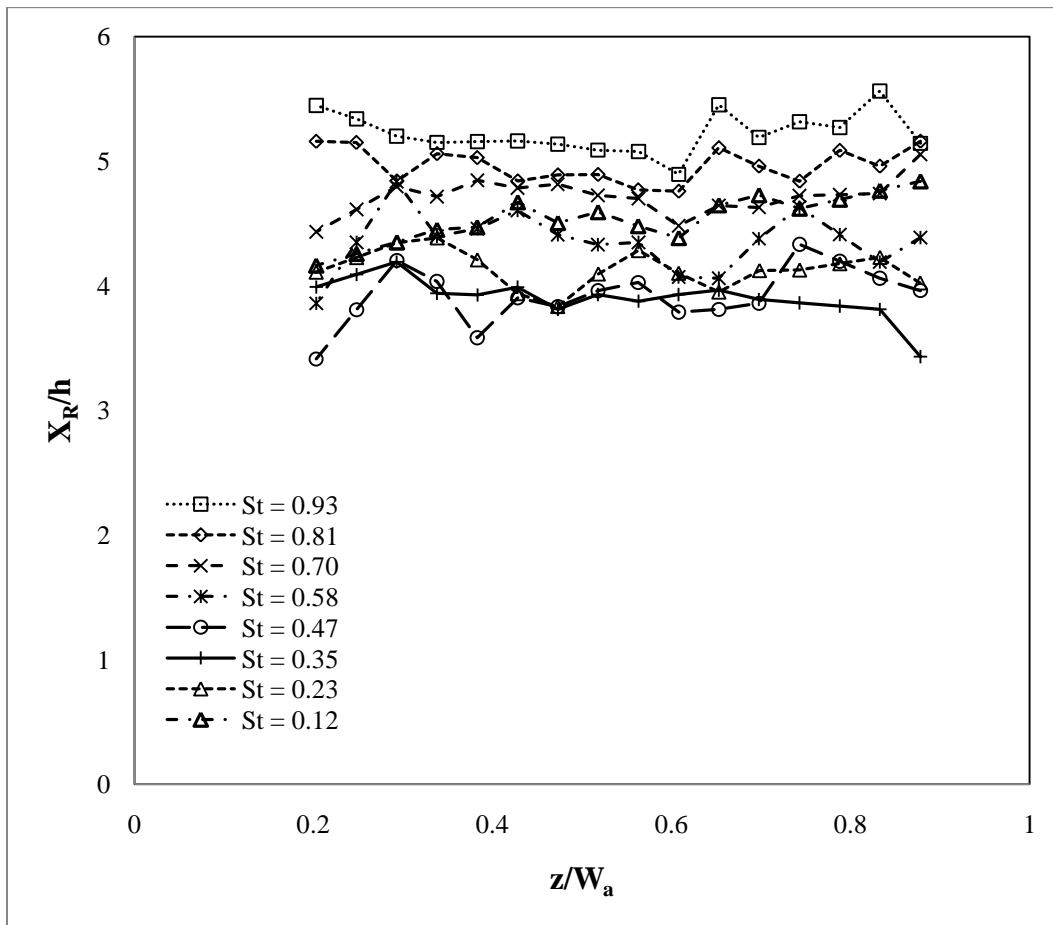


Figure 8.6 Spanwise variation of the reattachment lines for 2D forcing at  $u'/U_\infty = 0.35$ , for  $Re_h = 12540$ .

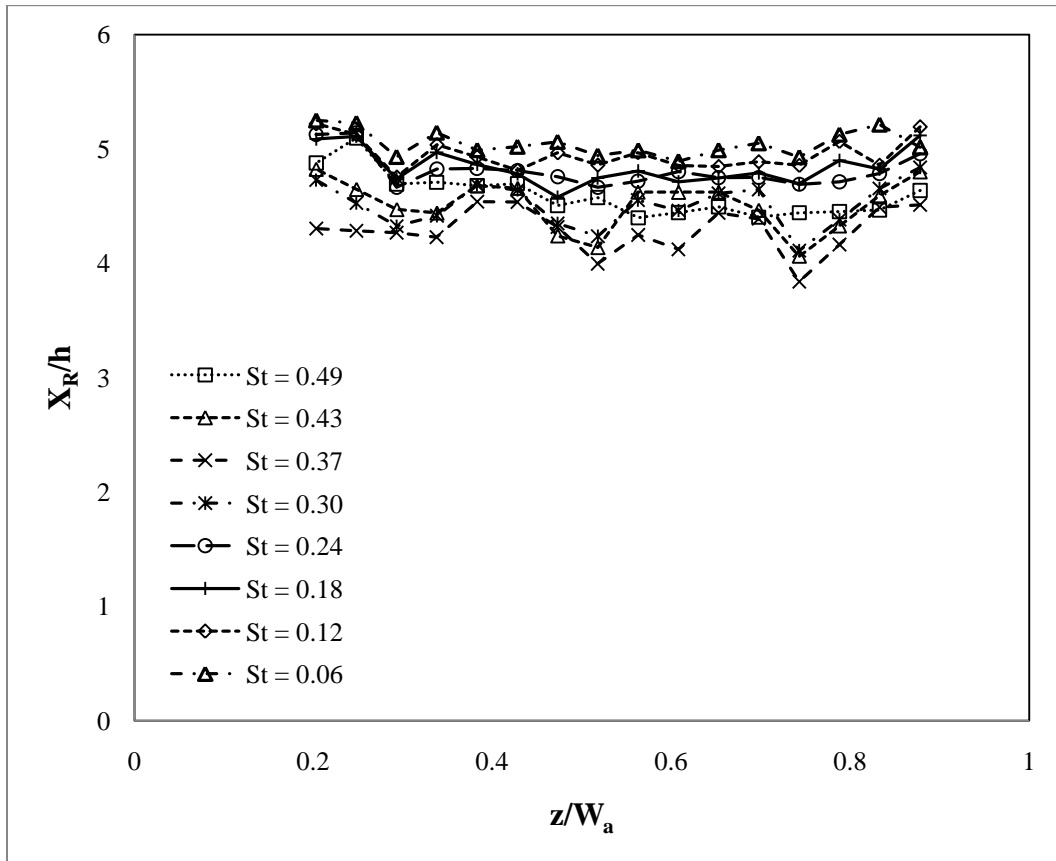


Figure 8.7 Spanwise variation of the reattachment lines for 3D forcing at  $u'_{rms}/U_{\infty} = 0.1$ , for  $Re_h = 24500$ .

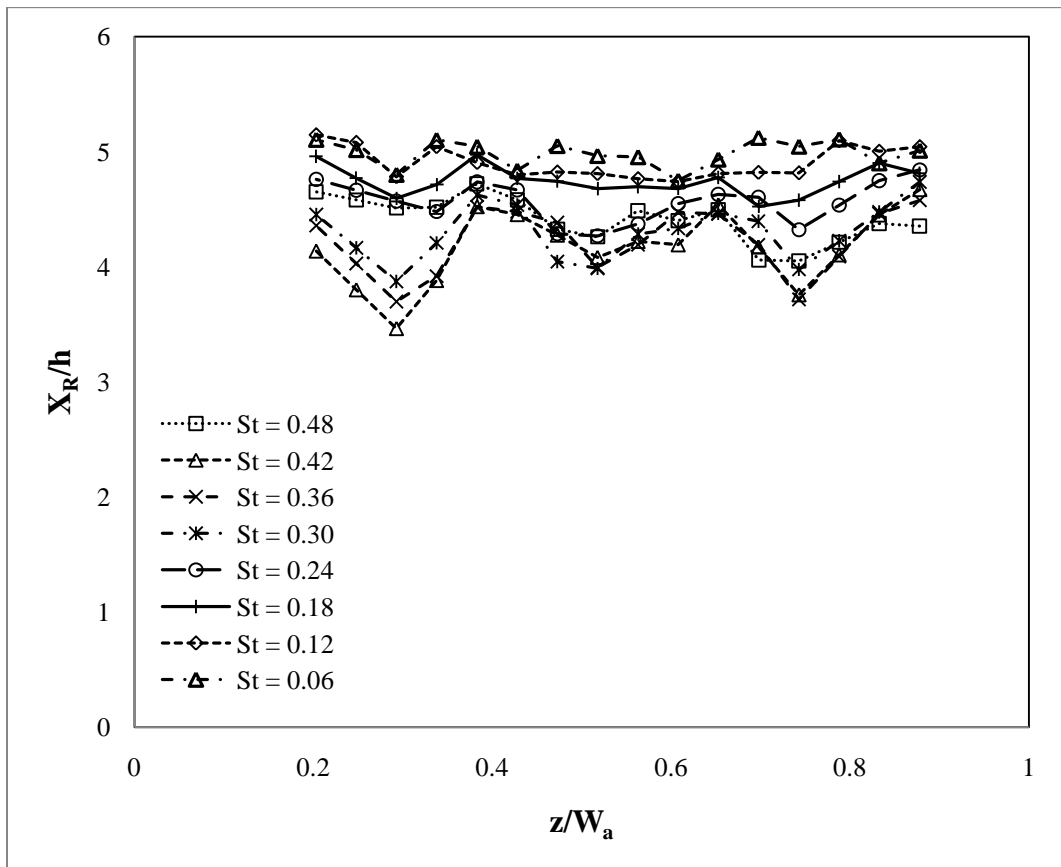


Figure 8.8 Spanwise variation of the reattachment lines for 3D forcing at  $u'_{rms}/U_\infty = 0.2$ , for  $Re_h = 24500$ .

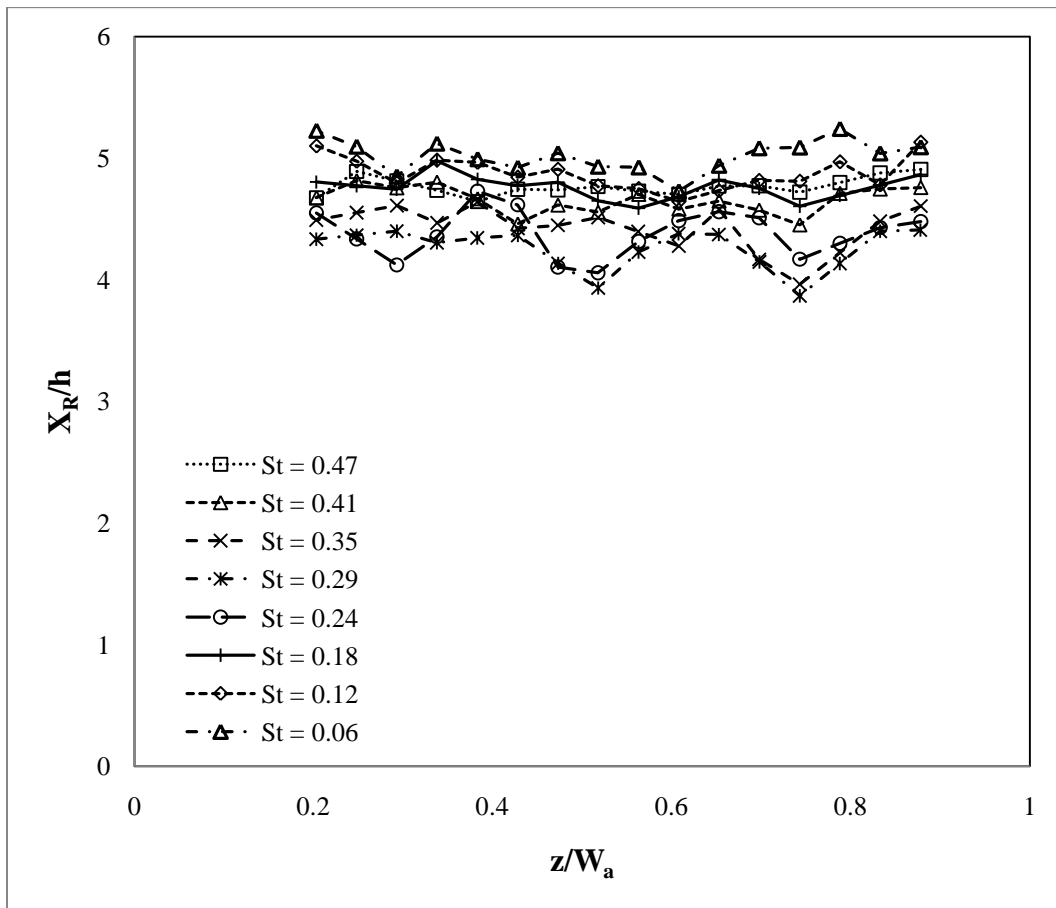


Figure 8.9 Spanwise variation of the reattachment lines for 3D forcing at  $u'_{rms}/U_\infty = 0.35$ , for  $Re_h = 24500$ .

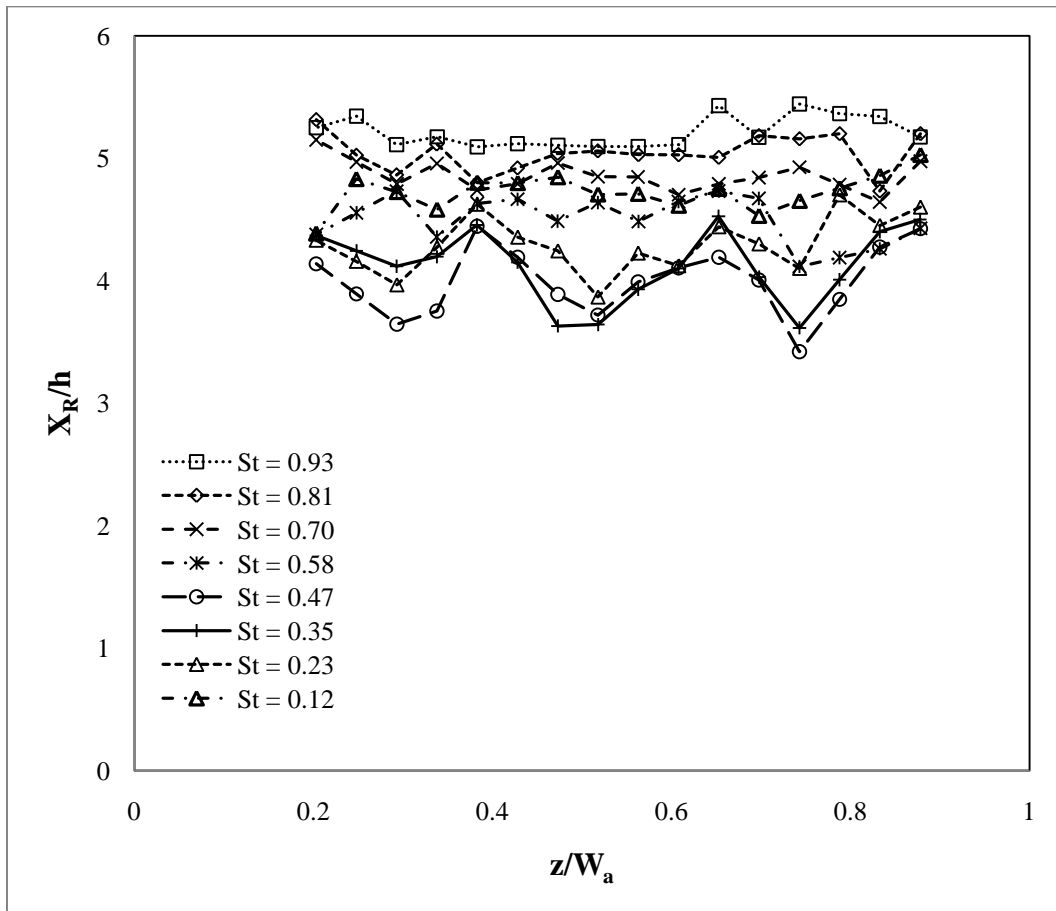


Figure 8.10 Spanwise variation of the reattachment lines for 3D forcing at  $u'_{rms}/U_\infty = 0.35$ , for  $Re_h = 12540$ .

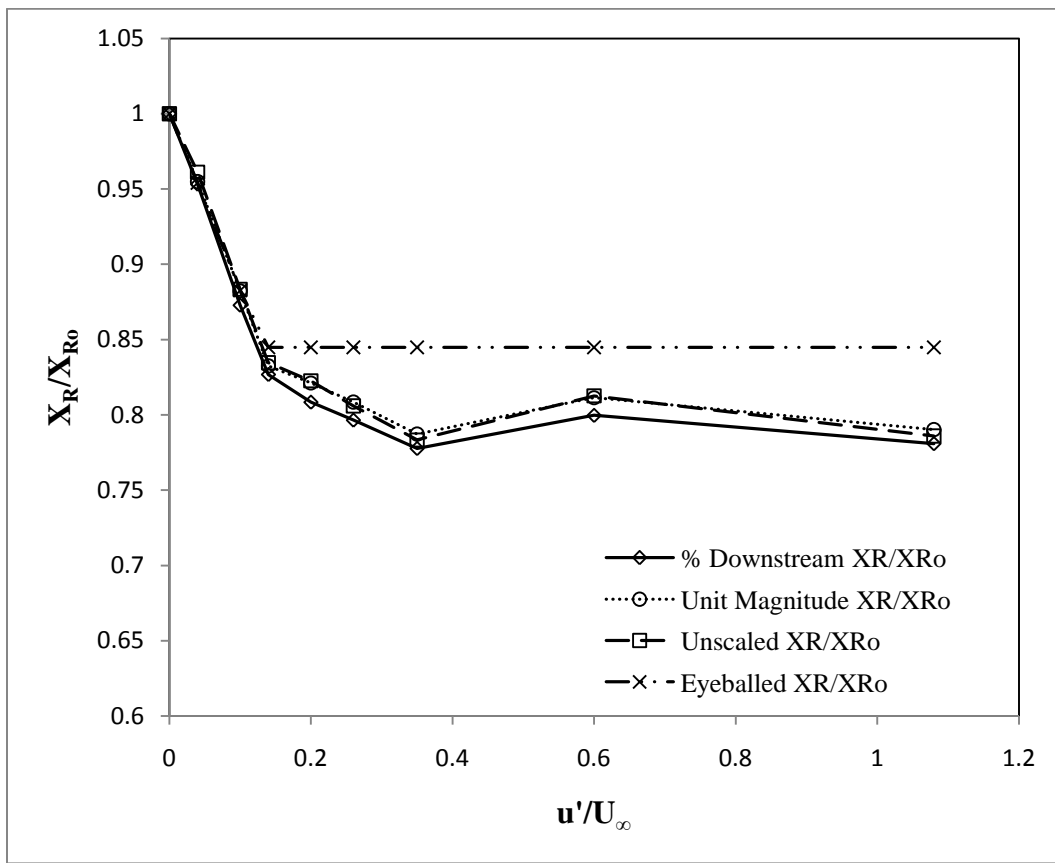
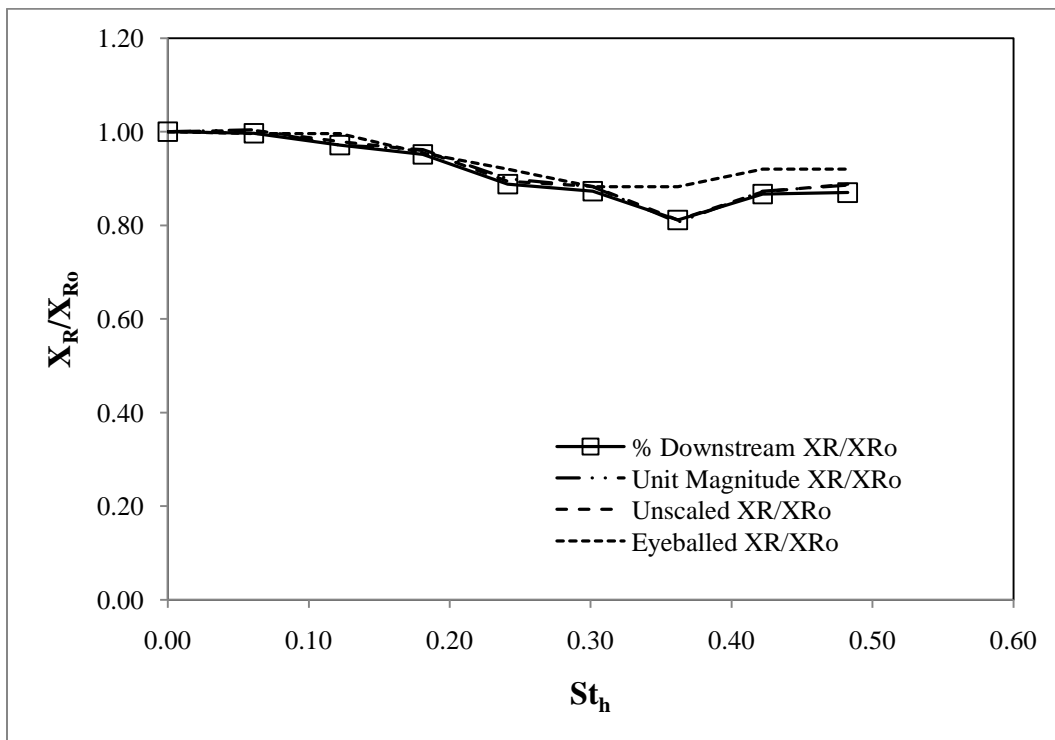
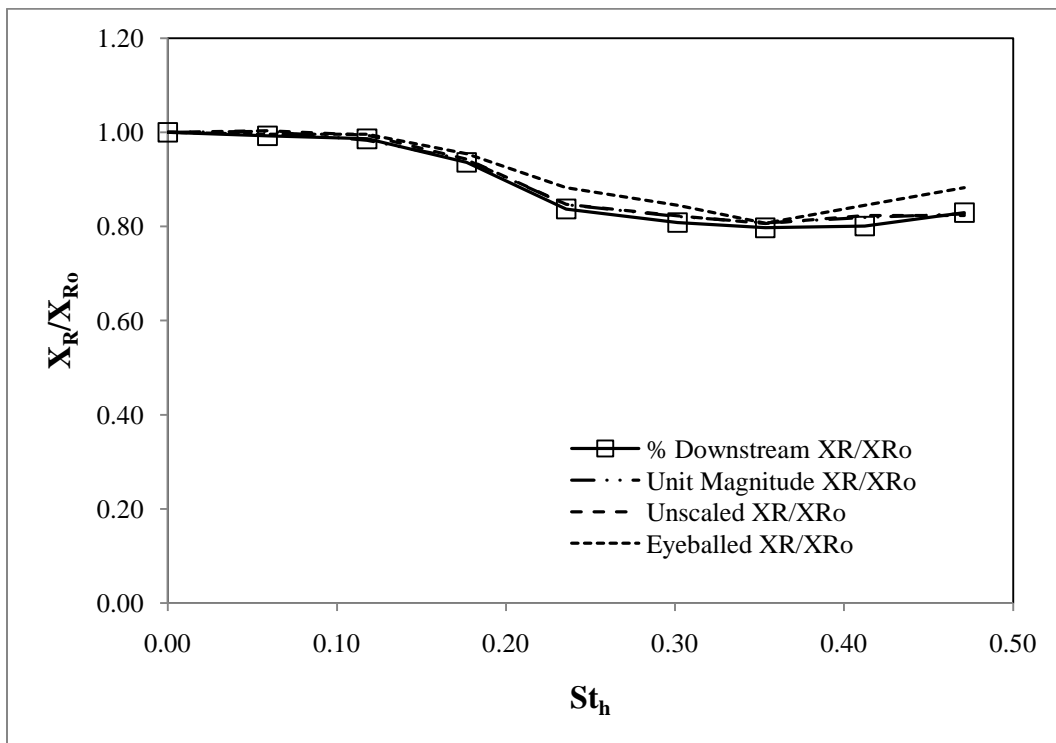


Figure 8.11 Normalized reattachment length vs. perturbation amplitude for 2D forcing at  $St_h = 0.3$ , for the different  $X_R$  calculation methods.



**Figure 8.12** Normalized reattachment length vs. Strouhal number based on step height, for 2D forcing at  $u'/U_\infty = 0.1$  and  $Re_h = 24500$ . Results are plotted for the four different reattachment length calculation methods.



**Figure 8.13** Normalized reattachment length vs. Strouhal number based on step height, for 2D forcing at  $u'/U_\infty = 0.2$  and  $Re_h = 24500$ . Results are plotted for the four different reattachment length calculation methods.

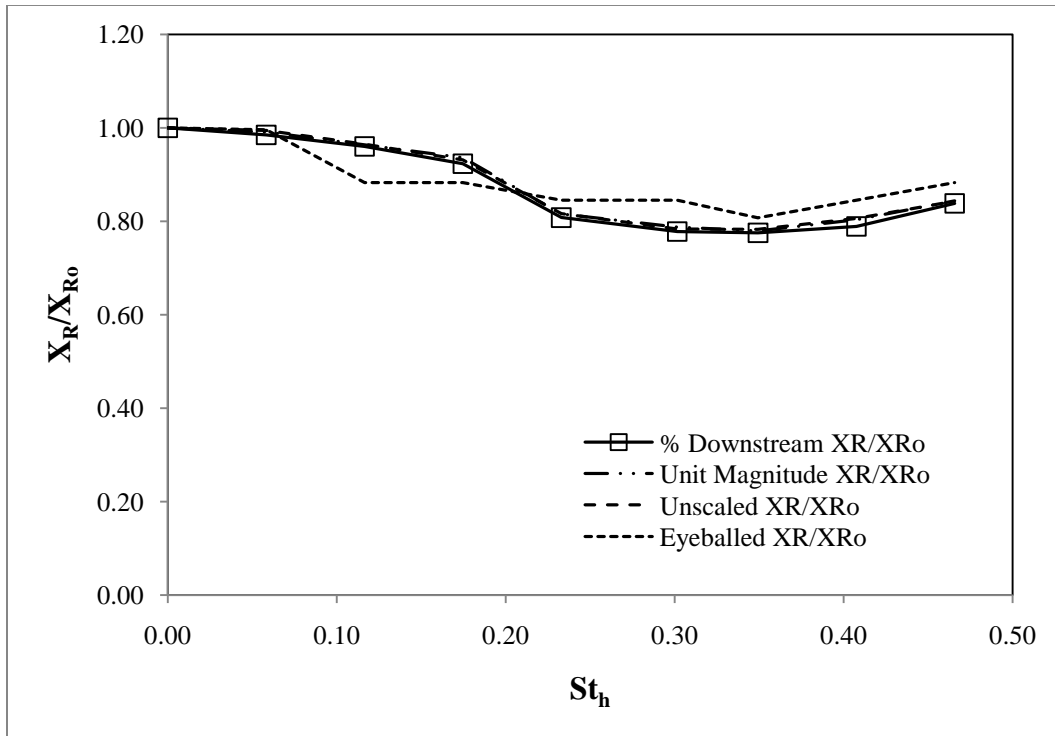


Figure 8.14 Normalized reattachment length vs. Strouhal number based on step height, for 2D forcing at  $u'/U_\infty = 0.35$  and  $Re_h = 24500$ . Results are plotted for the four different reattachment length calculation methods.

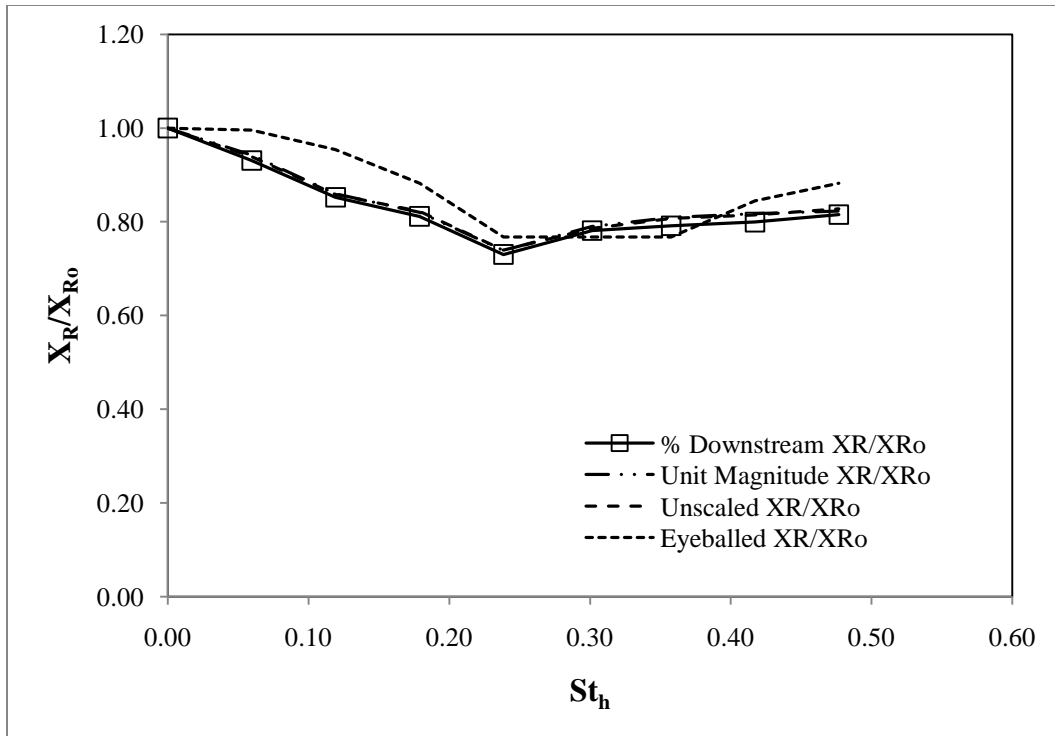


Figure 8.15 Normalized reattachment length vs. Strouhal number based on step height, for 2D forcing at  $u'/U_\infty = 1.08$  and  $Re_h = 24500$ . Results are plotted for the four different reattachment length calculation methods.

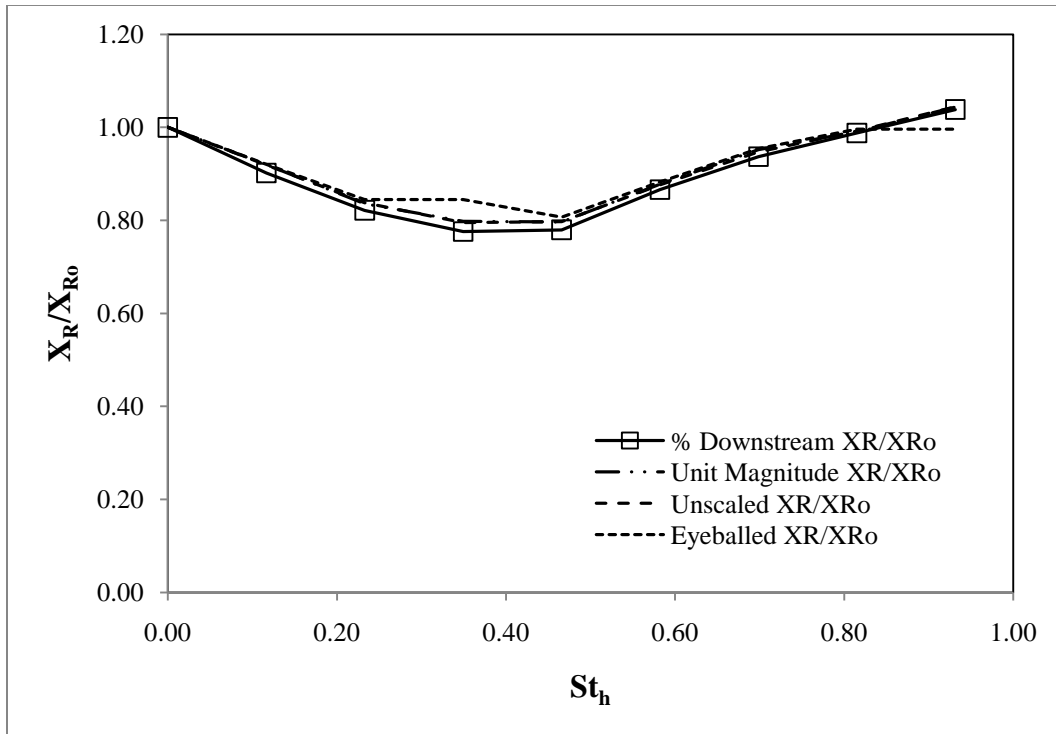


Figure 8.16 Normalized reattachment length vs. Strouhal number based on step height, for 2D forcing at  $u'/U_\infty = 0.35$  and  $Re_h = 12540$ . Results are plotted for the four different reattachment length calculation methods.

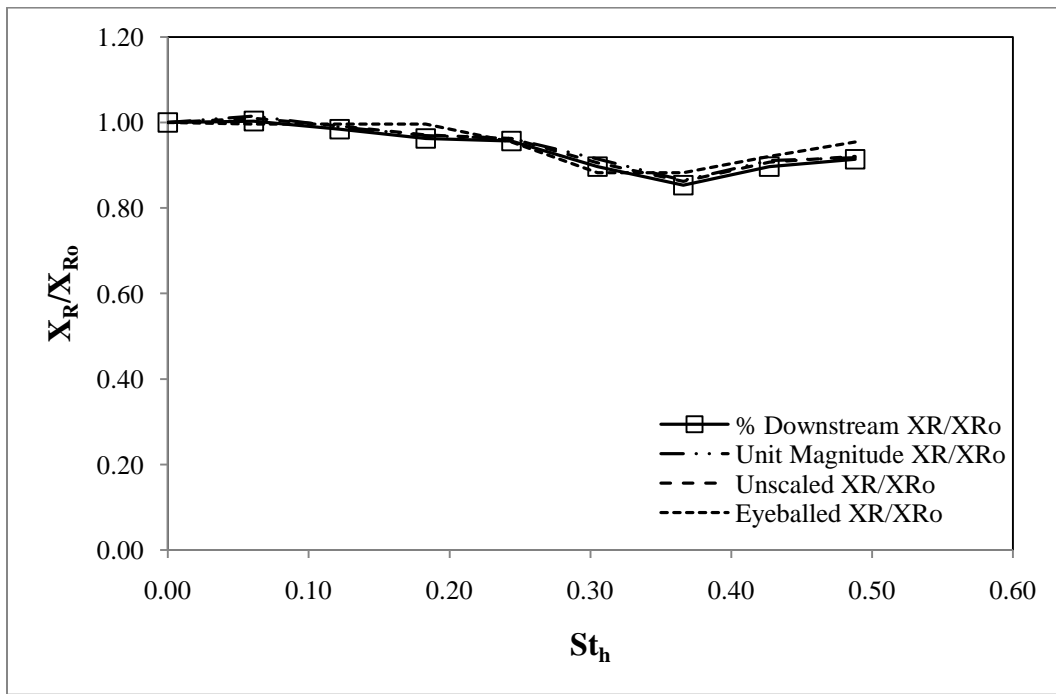
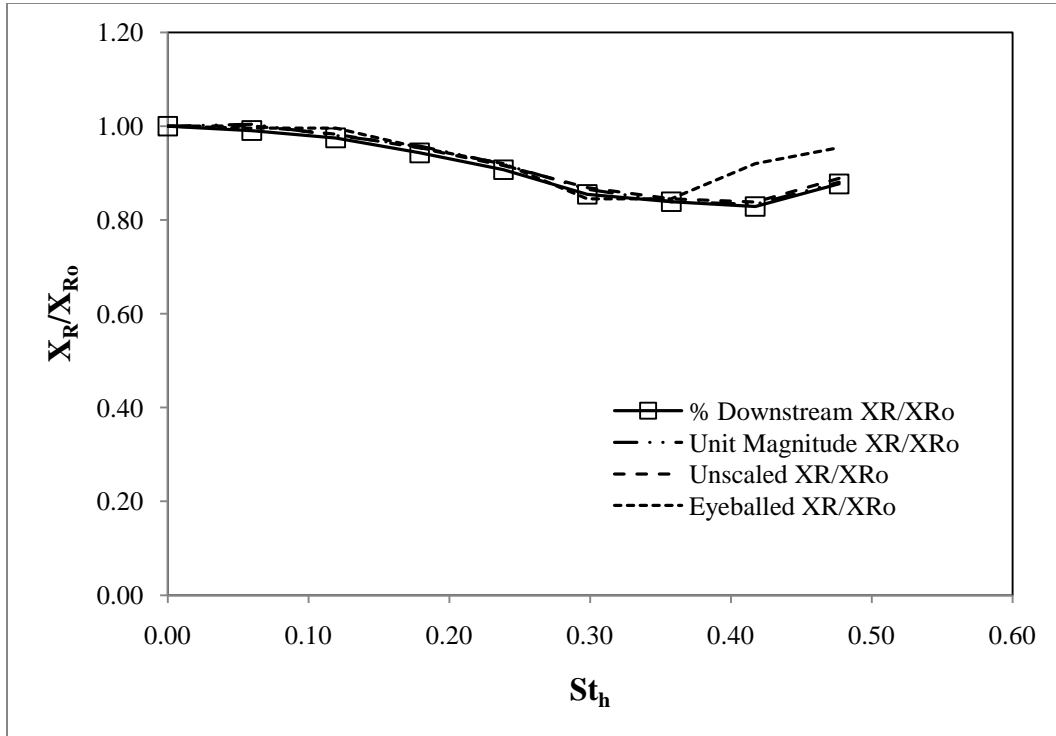


Figure 8.17 Normalized reattachment length vs. Strouhal number based on step height, for 3D forcing at  $u'_{rms}/U_\infty = 0.1$  and  $Re_h = 24500$ . Results are plotted for the four different reattachment length calculation methods.



**Figure 8.18** Normalized reattachment length vs. Strouhal number based on step height, for 3D forcing at  $u'_{rms}/U_\infty = 0.2$  and  $Re_h = 24500$ . Results are plotted for the four different reattachment length calculation methods.

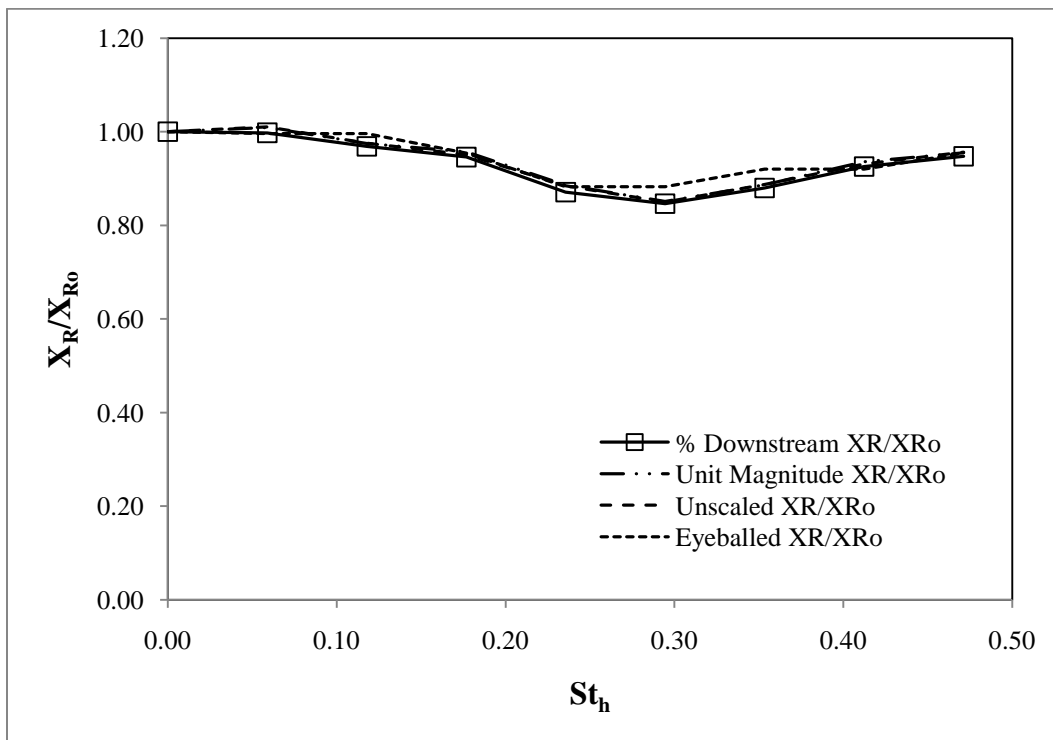
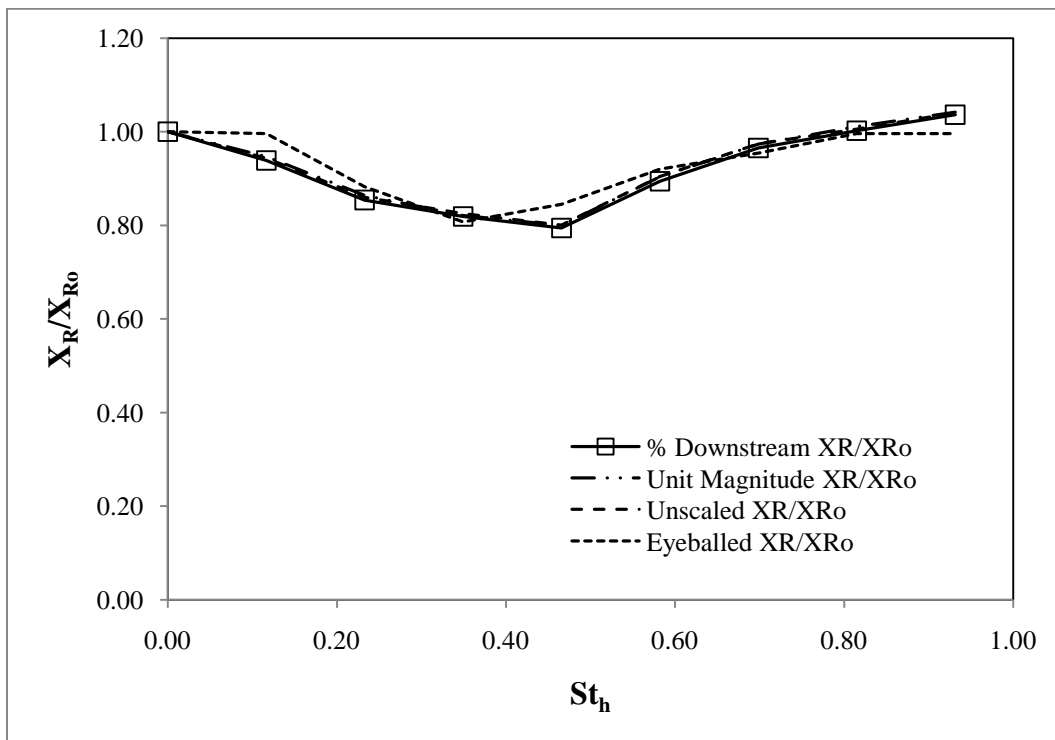


Figure 8.19 Normalized reattachment length vs. Strouhal number based on step height, for 3D forcing at  $u'_{rms}/U_\infty = 0.35$  and  $Re_h = 24500$ . Results are plotted for the four different reattachment length calculation methods.



**Figure 8.20** Normalized reattachment length vs. Strouhal number based on step height, for 3D forcing at  $u'_{rms}/U_\infty = 0.35$  and  $Re_h = 12540$ . Results are plotted for the four different reattachment length calculation methods.

## Appendix C: Operational Procedures

### C1: Air Bleed

This section outlines the procedure for purging small air bubbles from the hydraulic lines, assuming that the lines are not completely dry and the water tunnel is filled to the base of the snorkel. If the lines are completely dry, follow steps 1 and 2 only. Then, for each syringe, detach and hold the syringe below the level of the test section. Completely remove the plunger from the syringe, which will cause the all of the lines connected to said syringe to fill with water. When water fills the syringe, replace the plunger and re-fasten the syringe into its location on the actuator board. Then complete the rest of the following air bleed procedure starting with step 3, as small bubbles will likely remain in the lines. Figure 8.21 labels all associated positions and components.

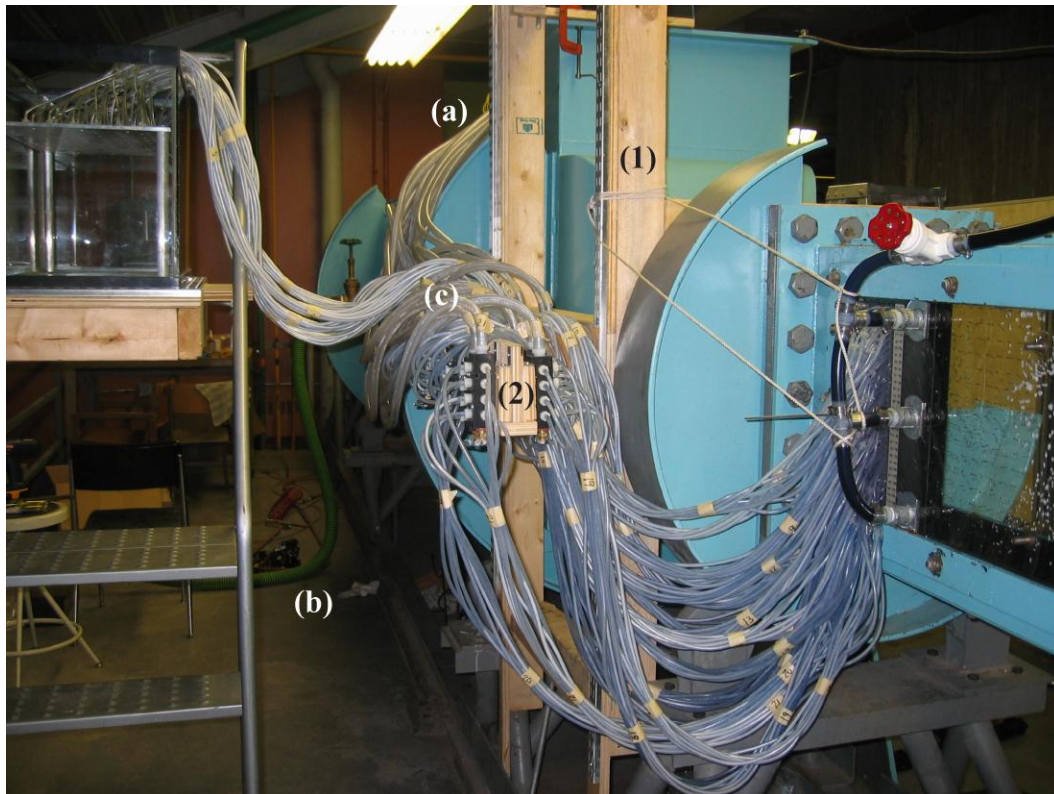


**Figure 8.21** Important components and positions associated with the air bleed procedure.

1. Disconnect all power and logic cables from their actuator board connections; i.e. the 9-pin serial cable to the SSC-32 servo controller card, and the positive and negative cables to the DC power supply. If an LVDT is attached to the actuator board, disconnect its power and data acquisition cables as well.

2. Carefully move the actuator board from position (a) at the top of the water tunnel to position (b) on the floor, on the manifold side of the water tunnel. This requires two people, and ensures that the actuator board is at the lowest elevation of any part of the hydraulic system.
3. As a general rule, the manifold rack (2) should be attached to the manifold support frame (1) at an elevation equal to the midpoint of the test section (Figure 8.21). If it is not, unhook the manifold rack at its joint with the rail system, and move it to the aforementioned location.
4. With the actuator board on the floor, bubbles will flow to the high points of the system. The high points will be at the tops of the bends in the 3/8 inch inner diameter tubes (c) where the tubing connects to the manifolds. Allow approximately 10 minutes for this to happen following step 2.
5. Unscrew the L-bracket supports that hold each manifold pair to the manifold rack. Holding them at the same elevation as the manifold rack, vertically flip the manifold pair so that the red-threaded stopcocks become the high points in the system. This allows the bubbles to move to the inside of the stopcocks.
6. Over a large bucket, slightly loosen one of the stopcocks. Hissing will be heard as the bubble escapes, and once the air bubble has been bled out of the system water will begin dripping from the stopcock into the bucket. Allow the water to drip; gently tapping the group of 1/8 inch manifold-to-step lines to ensure that no more bubbles exist. Close the stopcock, and repeat this step for the other stopcock in the manifold pair.
7. Re-fasten the manifold pair to the manifold rack in its original position, and repeat steps 5 to 7 for each manifold pair.
8. Return the actuator board to position (a), and reconnect power and logic cables.

## **C2: Actuator Use**

This section outlines basic startup instructions for the actuators. The actuator control instructions are outlined in Appendix D.

1. Visually verify that there are no bubbles in any of the hydraulic lines. If there are, perform the procedure outlined in Appendix C1.
2. Ensure that the actuator board is situated on top of the water tunnel settling tank, corresponding to position (a) in Figure 8.21. Also ensure that the water tunnel's free surface is at the same elevation as the actuators, in order to obey the condition of fluid dynamic similarity outlined by Gilbert (2007).

3. Begin running the water tunnel as per the usage instructions contained in its manual. Open and run PumpRPM.vi to monitor the water tunnel's speed based on a Hall Effect sensor designed and built by Marc Schostek.
4. Assuming that all power and logic connections are made (if the air bleed procedure has been followed correctly, they will be), switch on the Kepco box power supply and ensure that the voltage is between 5 and 6 V. Also ensure that the AC to DC converter (which powers the logic circuit) is set between 6 and 9 V. Incorrect power or logic voltage settings can cause the servo motors to behave erratically or to burn out completely.
5. If an LVDT is being used, turn on the LVDT power supply. If the data acquisition wires are to be used, make the connections with the NI USB-6229 box, then power on the control computer followed by the NI USB-6229 box. This order is crucial in preventing control program crashes.
6. Open TopLevelServoController.vi and test run the actuators at mid-range frequency and amplitude settings. Visually verify that the actuators are functioning as expected before attempting and high frequency or high amplitude tests. The usage instructions for TopLevelServoController.vi are included in Appendix D2.

## **Appendix D: LabVIEW**

### **D1: TopLevelServoController.vi Program Overview**

TopLevelServoController.vi is a servo control program that was written in conjunction with David Breakey. This program was used to control the actuators during all of the experiments pertaining to this thesis. However, at the time of writing this thesis, an improved servo control program was being developed by Marc Schostek in order to implement some of the proposed experiments in section 6.2.2. Due to the fact that the latest servo control program will be significantly different from the one outlined here, only a brief outline will be given. A more detailed description of the new servo control program will be included in Marc Schostek's master's thesis.

TopLevelServoController.vi is a program that allows the servo operator the ability to modify built-in LabVIEW waveform generation functions to produce desired actuation characteristics. The default output of the program is in the form of ASCII text strings that are sent to the SSC-32 servo controller card on a channel-by-channel-basis. Batch control options are also available. The program is currently configured to send sinusoidal (in time) actuation waveforms. Spanwise wave variations can be generated by altering the amplitudes and initial phase offsets for each servo channel. The program is currently configured to produce standing waves across the span of the step. The program's output strings are converted into pulse width modulated voltages by the firmware in the SSC-32 servo controller card, which are subsequently sent to the servos.

### **D2: Program Usage Instructions**

Before following these instructions, the procedure from Appendix C2 must have already been completely implemented. Figure 8.22 shows the front panel for TopLevelServoController.vi; to view the program code in the form of a block diagram the user can select (from the file menu): Window > Show Block Diagram.

1. Ensure that the VISA settings are correctly set to the port, BAUD rate, bits, and parity settings of the SSC-32 servo controller card.
2. Hit the Run arrow in the top left corner of the window, but first ensure that only the oval buttons in the "Active" line (Figure 8.22) have their green triangles illuminated. Toggling these buttons determines which servos are sent signals.
3. Before applying any sine wave forcing, ensure that the servo motors are centered in their amplitude range; this can be completed by pressing the

“All to 1500” button near the top of the window. When the servos are centered, the “Position” indicator bars will appear as they do in Figure 8.22.

4. Set the desired amplitudes, offsets, and frequencies for each servo motor. This can be done manually in the boxes under each servo’s position indicator, or as a batch control (effective for 2D forcing) using the boxes in the bottom left corner of the window.
5. Amplitude settings must be between 500 and 2500. A pulse width to syringe displacement calibration factor can be found in the Excel file ServoExperimentControl.xls. Alternately, the Excel file itself can be altered to save pre-set waveforms for quick interchanges between experimental runs. Once the Excel file has been altered and saved, the “Get Run Information From Excel File”, and the “Refresh Control Data From Current Run” will apply the pre-set waveform to the new run. All preset waveforms are displayed in the “Select Run...” box.
6. When experiments are completed, as an extra measure of safety it is generally a good idea to re-center the servos in case this step is accidentally omitted at the beginning of the next run.
7. Hit “STOP” and turn off the servo and logic power.

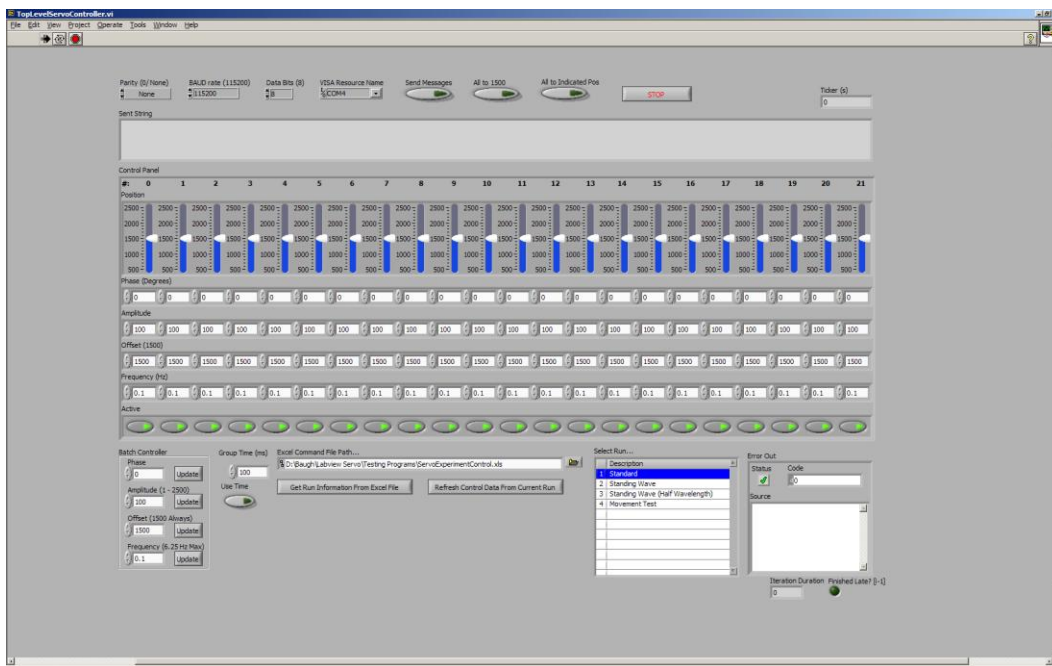


Figure 8.22 The TopLevelServoController.vi program front panel.

## Appendix E: MATLAB

This appendix presents the program overview and usage instructions for our tuft-based image processing application, tuftImgProApp.m, in a slightly different manner than we presented our LabVIEW control program. Rather than separate overview and usage instructions sections as in Appendix D, this section contains the file ReadMe.txt as Section E1 which both outlines the programs and provides usage instructions. This file was written by David Breakey, and initially accompanied tuftImgProApp.m as a supplemental piece of information on the program. This file is provided with the express written consent of the author. Section E2 provides screen shots of the program to accompany the instructions in E1.

### E1: tuftImgProApp.m Program Overview: ReadMe.txt

```
%%%%%%%%%%%%%%%%%%%%%%%%%%%%%%%%%%%%%%%%%%%%%%%%%%%%%%%%%%
%
%
%   tuftImgProApp Application Description   %
%               (And Readme)              %
%
%
%%%%%%%%%%%%%%%%%%%%%%%%%%%%%%%%%%%%%%%%%%%%%%%%%%%%%%%%%%
%
%
%   *** IN PROGRESS ***                   %
%   Version: 1.1                          %
%   Last Revision: 30. September 2009    %
%
%   Coded by:                             %
%   David Breakey (breakey@ualberta.ca)  %
%
%   Vortex Fluid Dynamics Laboratory     %
%   University of Alberta                 %
%   5-31 Mechanical Engineering Building  %
%   University of Alberta                 %
%   Edmonton, Alberta, Canada T6G 2G8    %
%   Tel. 780 492-1284                    %
%
%
%%%%%%%%%%%%%%%%%%%%%%%%%%%%%%%%%%%%%%%%%%%%%%%%%%%%%%%%%%
```

#### CONTENTS

- 0. Executive Summary
- 1. Overview
- 2. Structure
- 3. Use
  - I. Importing Image Files
  - II. Previewing Images to be Transformed
  - III. Transforming Files

- IV. Saving Data and Images
  - V. Averaging Vector Data
    - i. Previewing Data
    - ii. Averaging Data
    - iii. Viewing Averages
    - iv. Saving Data
    - v. Threshold
  - VI. Importing Vector Data
- 4. Data Files
- 5. A Note on the Universal Coordinate System
- 6. Additional Licenses

%%%

## 0. Executive Summary

To run the application without reading the instructions, type the command "tuftImgProApp" into the MATLAB command line.

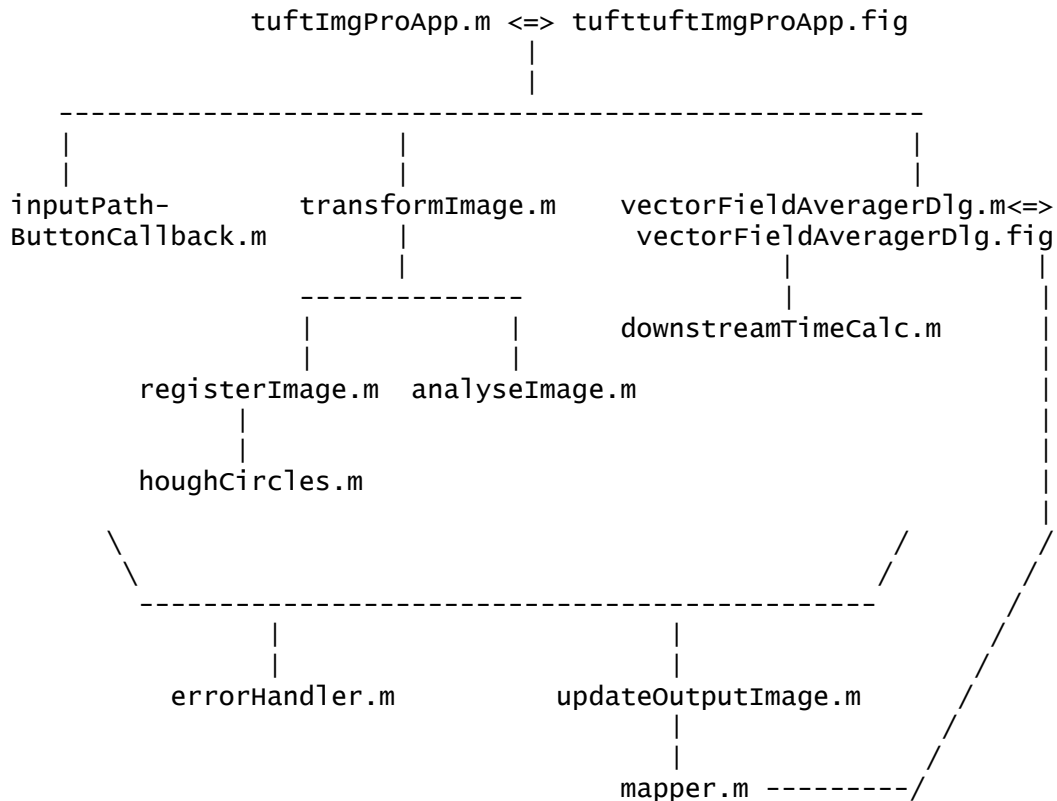
### 1. Overview

tuftImgProApp is a MATLAB application for processing images from a tuft array. tuftImgProApp takes images, and determines how the tufts are oriented. The program then creates vector fields from the images. These vector fields can be saved as data (they are automatically saved as .xls [Microsoft Excel] files with the filename of the input image but in the chosen directory) and they can also be viewed against the images. These images can be saved as .tif files.

After the data has been obtained, opening the Average Fields Dialogue allows the chosen fields to be averaged by direction (n.b. the averaging maintains only the direction data, not magnitudes). If fields were previously saved as .xls files, the data can be imported directly into the Average Fields Dialogue using the import button. This allows the data to be used without having to redo the image processing tasks, which can take a considerable amount of time. This also allows averages to be made in different combinations of data sets that were not processed together.

### 2. Structure

The main application file for the application is tuftImgProApp.m. This file has all the callbacks for tuftImgProApp.fig, which is the main GUI for the application. Contents.m contains a list and brief description of all the m-files in the application directory; this can also be accessed using MATLAB's Content's Report command. Further details are available in each m-file. The program hierarchy is as follows:



Note: errorHandler.m is called in almost any error instance.  
 updateOutputImage.m is called from both  
 vectorFieldAveragerDlg.m and tuftImgProApp.m.

### 3. Use

- I. Importing Image Files
- II. Previewing Images to be Transformed
- III. Transforming Files
- IV. Saving Data and Images
- V. Averaging Vector Data
  - i. Previewing Data
  - ii. Averaging Data
  - iii. Saving Data
- VI. Importing Vector Data

#### I. Importing Image Files

Image files are imported using the "Import Images From..." field. Clicking the "..." button brings a dialog for selecting files to be imported. Multiple files can be selected. When the images are imported, their filenames appear in the "Preview Image" listbox. Several image types are supported.

#### II. Previewing Images to be Transformed

Before transforming the images, which can be a long process, it is a good idea to confirm that the selected images are correct. This can be done by clicking the filenames in the "Preview Image" listbox. The selected image appears in the "Source Image" pane.

### III. Transforming Files

To transform the selected files, click the "Transform Selected Images..." button. During this process, a wait bar indicates the progress in terms of how many images have been completed. WARNING: This process can take a long time. Usually about 75 seconds per image.

### IV. Saving Data and Images

After the images have been transformed, the transformed and registered images as well as the vector fields are available for preview. This can be done in same way as previewing the input files. The "Transformed Image Options" pane determines what is to be displayed in the "Transformed Image" pane (e.g. choosing "Registered Image" and "Vector Field" will superimpose the vector field over the image). The data can be saved to .xls files, which will share the filenames of their respective images by using the "Save data to..." pane. These files will also contain the filename and timestamp when the file was made. They can be used later (see "VI. Importing Vector Data"). The images displayed in the "Transformed Image" pane can also be saved as .tif files. They will be saved using the preferences from the "Transformed Image Options" pane. These will be saved with the name "Trans\_XXX.tif", where XXX represents the filename of the respective input image.

### V. Averaging Vector Data

After the images have been transformed, the same selection of vector fields can be averaged in the "Average Vector Fields" dialogue. Clicking "Average Vector Fields for All Images..." opens this dialogue. NOTE: Averages can only be performed on images that have the same points mapped. This means that the same number of tufts (in both x and z directions) have to have been detected in each set. This can be checked by inspecting the .xls file.

#### i. Previewing Data

The fields can be previewed in the same way as in the original application: clicking the listbox with the filename makes that field appear in the preview pane.

#### ii. Averaging Data

The fields are averaged when the "Average Fields" button is pressed. The new field is then displayed in the "Averaged Field" pane. This method determines the average direction of the tuft over the specified data sets. A second method that determines the percent of fields in which each tuft is pointing downstream is performed when the "% Fields Downstream Average" button is clicked.

#### iii. Viewing Averages

In addition to the two averaging methods, the "Average Fields" statistic can be viewed in two ways. When the "Average Fields" operation has been performed, a menu will appear to the right of the averaging window allowing the selection of either a vector or contour plot. Selecting the radio button will display that plot. There is a slight delay between clicking the button and the plot (~1 sec), so patience is necessary.

iv. Saving Data

Saving the data will create both a .tif file of the image displayed in the "Averaged Field" pane, and a .xls file of the averaged data. The .xls file will also contain a timestamp and a list of the files used in the average. The files will be named "XXX.xls" and "XXX.tif", where XXX represents a chosen filename given in the save dialogue. The averaging method saved will be whatever method was used last. The saved image will represent whatever image was displayed in the averaging pane when the save button was pressed.

v. Threshold

The threshold value slider chooses a minimum x-component for the tuft to be considered valid. Every tuft that has a x-component less than this value is turned into a zero vector for the averaging operation. This is to stop tufts with very little motion from being read as valid tufts. This is specifically for tufts right behind the step so they don't get erroneously included.

## VI. Importing Vector Data

Vector files created by the program in .xls format can also be imported into the "Average Vector Fields" dialogue. This is done using the "Import Fields..." button. After the fields are selected, the use is identical to that given in "V. Averaging Vector Data." NOTE ON IMPORTED DATA: Only images that see same tufts can be averaged together. Data that was taken from two different camera positions (different enough that the visible tufts are different) can't be averaged together. Confirm--either visually or in the excel files--that the grid was the same.

### 4. Data Files

The data files are written in .xls format for Microsoft Excel. They contain several text header lines that include a timestamp, a list of input files used to create the file, and column headers for the data. .xls format was chosen because of its versatility and stability. This leaves the option of using the data for a wide variety of analyses. Although the program doesn't currently use it, the data files contain an additional two columns that contain non-normalized versions of the tuft data. The program normally normalizes the vectors so they represent only direction. At the time of writing, it is believed that this is the more useful form of the data. However, in order to preserve as much information as possible, the non-normalized data was obtained in case it can ever be found useful. The actual data reflects only

the distance from the tuft's centroid to the point (in pixels) and may have no important use at all.

The data file headers are:

x coordinate (px)	The coordinates of the data point, given
y coordinate (px)	in pixels in the image coordinate system.
x coordinate (cm)	The coordinates in cm in the Universal
y coordinate (cm)	Coordinate system.
x component (reg)	Normalized components of vectors in Universal
y component (reg)	coordinate system. Uses regression method
	performed during the image processing tasks.
x component (px, cent, non-normalized)	Non-normalized components
y component (px, cent, non-normalized)	of vectors in pixels.
	Uses centroid method
	performed during the
	image processing tasks.

## 5. A Note on the Universal Coordinate System

The universal coordinate system used in the program reflects an x-distance measured from the step edge heading downstream in the water tunnel. The y-coordinate is measured from the bottom of the water tunnel to the top. Theoretically, regardless of camera position as long as the image is square with the tuft plate, each tuft will have the same location in the universal coordinate system. This is depended upon to perform the averaging of the vector fields. Minor differences may mean slight error in the averaged field. This is only a concern if the images used are from different sets where the camera position differs. This should be kept in mind when judging whether the program is functioning properly.

## 6. Additional Licenses

HOUGHCIRCLES.M was obtained from:

<http://www.mathworks.com/matlabcentral/fileexchange/22543> on:  
2. June 2009 and is used and modified under the following  
copyright notice:

```
%%%%%%%%%%%%%%%%%%%%%%%%%%%%%%%%%%%%%%%%%%%%%%%%%%%%%%%%%%%%  
Copyright (c) 2008, Yuan-Liang Tang  
All rights reserved.
```

Redistribution and use in source and binary forms, with or without modification, are permitted provided that the following conditions are met:

- \* Redistributions of source code must retain the above copyright notice, this list of conditions and the following disclaimer.
- \* Redistributions in binary form must reproduce the above copyright notice, this list of conditions and the following disclaimer in the documentation and/or other materials provided with the distribution

THIS SOFTWARE IS PROVIDED BY THE COPYRIGHT HOLDERS AND CONTRIBUTORS "AS IS" AND ANY EXPRESS OR IMPLIED WARRANTIES, INCLUDING, BUT NOT LIMITED TO, THE IMPLIED WARRANTIES OF MERCHANTABILITY AND FITNESS FOR A PARTICULAR PURPOSE ARE DISCLAIMED. IN NO EVENT SHALL THE COPYRIGHT OWNER OR CONTRIBUTORS BE LIABLE FOR ANY DIRECT, INDIRECT, INCIDENTAL, SPECIAL, EXEMPLARY, OR CONSEQUENTIAL DAMAGES (INCLUDING, BUT NOT LIMITED TO, PROCUREMENT OF SUBSTITUTE GOODS OR SERVICES; LOSS OF USE, DATA, OR PROFITS; OR BUSINESS INTERRUPTION) HOWEVER CAUSED AND ON ANY THEORY OF LIABILITY, WHETHER IN CONTRACT, STRICT LIABILITY, OR TORT (INCLUDING NEGLIGENCE OR OTHERWISE) ARISING IN ANY WAY OUT OF THE USE OF THIS SOFTWARE, EVEN IF ADVISED OF THE POSSIBILITY OF SUCH DAMAGE.

%%%

## E2: Screen Images

Here we briefly present two screen images to supplement the instructions from E1. Figure 8.23 shows the tuftImgProApp.m main window, and pertains to the instructions from points I to IV in David Breakey’s ReadMe.txt file. Figure 8.24 shows the vector averaging window pertaining to the instructions in points V and VI.

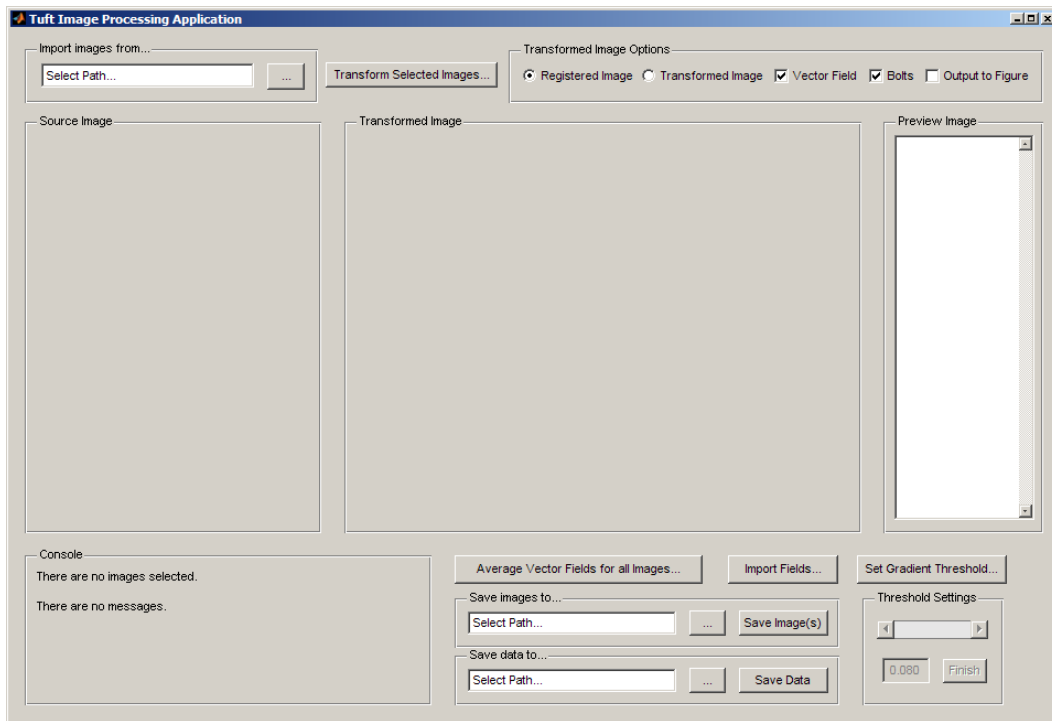


**Figure 8.23** The main window for tuftImgProApp.m (accompanies instruction points I to IV in ReadMe.txt).

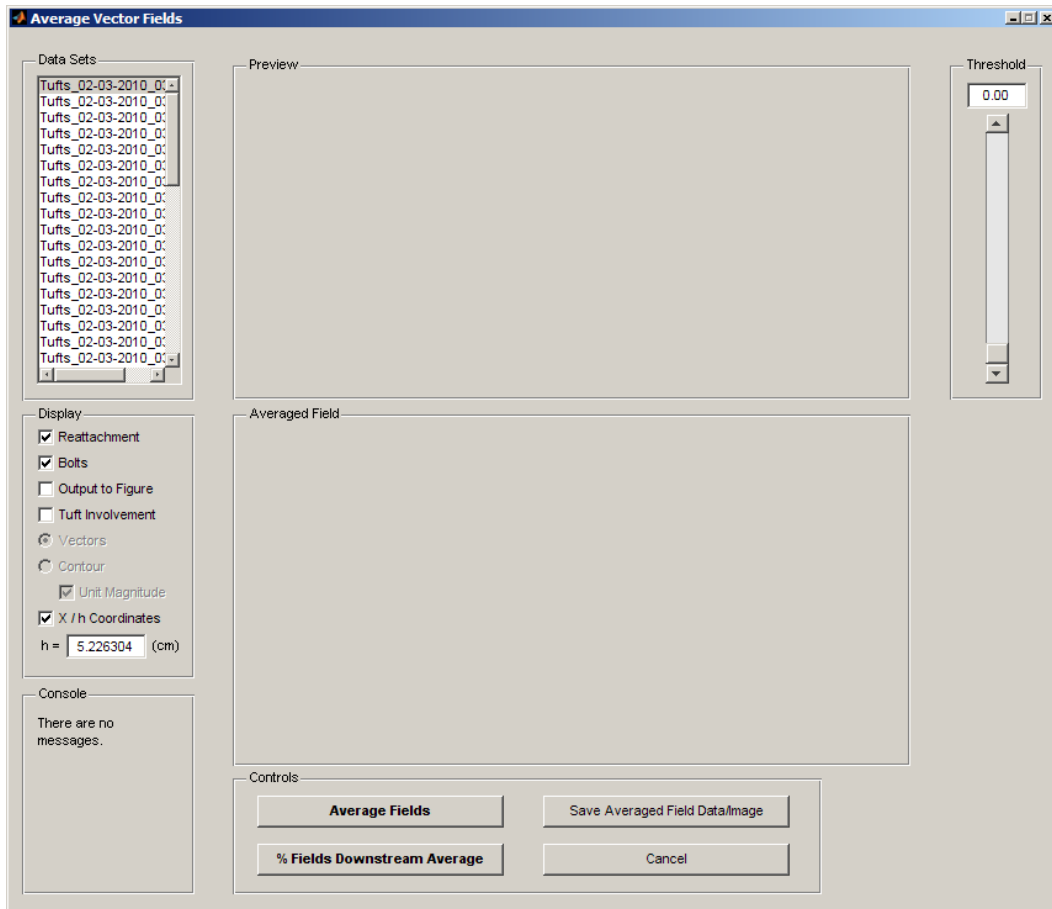


**Figure 8.24** The vector field averaging window for `tuftImgProApp.m` (accompanies instruction points V and VI in `ReadMe.txt`).

## Appendix F: Statistical Error Analysis

This section presents two brief tests that were undertaken to determine the number of images that were necessary to obtain reliable time-averaged information for a given data point (F1), and some random repeatability tests as well (F2).

### F1: Number of Images Necessary for Convergence

We mentioned earlier that for each data point (i.e. one forcing profile, at specific  $u'/U_\infty$  and  $St_h$  values, for a specific  $Re_h$ ) at least 50 images were averaged to obtain the time-averaged flow information that we presented. The 50 image criterion was not selected arbitrarily. Figure 8.25 displays the data from our brief test to determine this criterion.

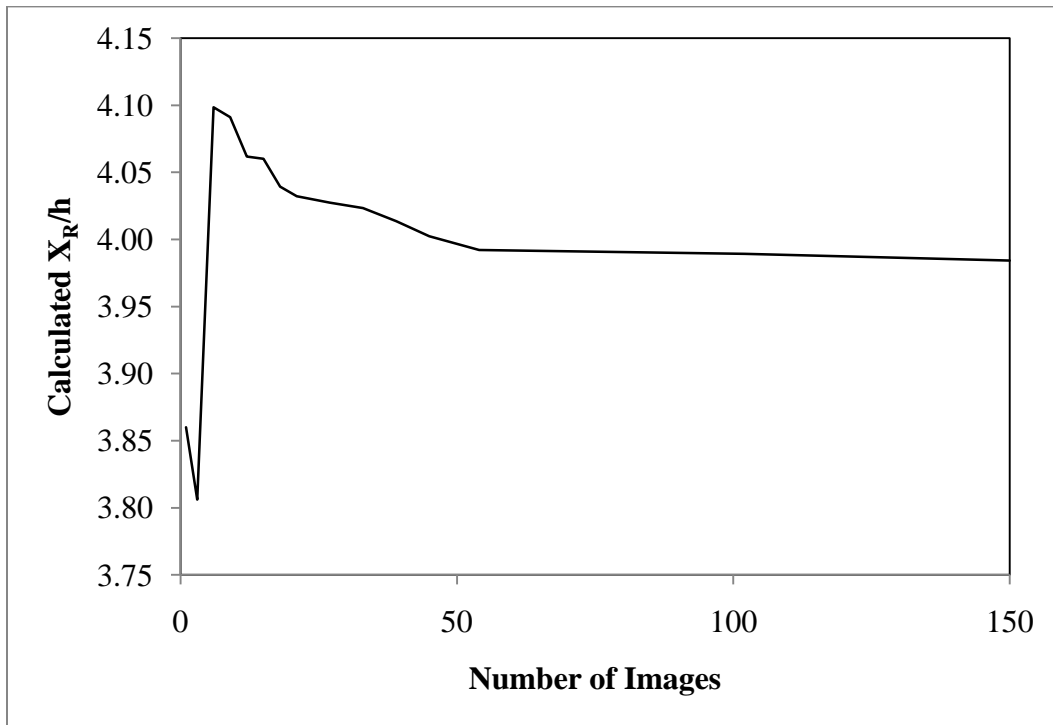


**Figure 8.25** Data from the test to determine the number of images that were required for time averaging of a single data point. The data point, randomly selected, corresponded to  $Re_h = 24500$ ,  $u'/U_\infty = 1.08$ ,  $St_h = 0.3$  for 2D forcing. The average value of  $X_R/h$  was 3.988 over 150 images.

To do so, we randomly selected a single data point which had a least 50 images worth of raw output data. The selected data point was from our reattachment reduction vs. 2D perturbation amplitude testing; with  $Re_h = 24500$ ,  $u'/U_\infty = 1.08$ , and  $St_h = 0.35$ . To produce Figure 8.25, we performed the same  $X_R/h$  averaging calculations on image groups with increasing numbers of images in each group.

When 50 or more images were used in  $X_R/h$  averaging calculations, the calculated values for average  $X_R/h$  differed by no more than  $0.02h$ , which corresponded to an agreement within roughly 0.4%. Also, we noted that for image groups of 18 or greater, the calculated values of  $X_R/h$  were consistent to  $\pm 0.04h$ . This indicated that for our initial uncertainty estimate of  $\pm 0.1h$  (based differences between the three  $X_R/h$  calculation methods) was most likely a very conservative estimate.

Still, instead of using fewer images in averaging calculations, we elected to use 50 as our minimum number to add a measure of increased certainty to our results. As was previously stated, at lower Reynolds numbers individual tufts have a greater chance of being omitted from image processing calculations. Using more images would likely account for this possible additional loss in data. Conceivably, we could also have done the opposite and used more images in our time averaging calculations. However, with 50 images corresponding to roughly one hour of data processing time, we concluded that the small increase in accuracy due to 150 image data sets was not worth the extra 2 hours of processing time per data point that this would involve.

## F2: Repeatability of Results

In addition to the minimum number of images calculation, we also performed four random repeatability verifications to gain an understanding of the degree to which our results varied between trials. We decided to carry out these verifications during our 2D forcing experiments as a means of checking that our actuators were producing consistent reductions in average reattachment for the same runs, on different days. Table 8.3 displays the results of these 5 verification runs.

The results from these verifications were encouraging, with all but the final test agreeing within our  $\pm 0.1h$  estimate of uncertainty in reattachment measurements.

**Table 8.3 Results from 5 separate repeatability verifications performed for our high Reynolds number, 2D forcing experiments.**

Test	$St_h$	$u'/U_\infty$	Date of Test	$X_R/h$	Difference
Re = 24500 2D Forcing	0.3	0.1	11/02/2010	4.391	0.2%
			16/02/2010	4.396	
Re = 24500 2D Forcing	0.3	0.2	11/02/2010	4.067	1.2%
			17/02/2010	4.149	
Re = 24500 2D Forcing	0.3	0.35	11/02/2010	3.913	1.2%
			17/02/2010	3.964	
Re = 24500 2D Forcing	0.3	1.08	12/02/2010	3.929	1.0%
			19/02/2010	3.907	
Re = 24500 2D Forcing	0.36	0.1	15/02/2010	4.081	3.8%
			16/02/2010	4.238	

## **Appendix G: Fidelity of Forcing**

This section attempts to characterize the extent to which we are confident that our actuators are functioning properly. Sections G1 and G3 briefly summarize the results obtained from two separate calibrations performed by David Breakey and Marc Schostek (Appendix G1) and Marc Schostek (Appendix G3). Section G2 outlines the results of a manual calibration that was performed as a precursor the more detailed measurements found in Appendix G3. Only brief summaries of the calibration results will be presented here, as Marc Schostek will provide complete calibration information in his master's thesis.

### **G1: Initial Calibration Results**

The first calibration the actuators occurred in July of 2009, performed in conjunction with Marc Schostek and David Breakey. A disconnected and unloaded servo was tested over a high amplitude range for frequencies ranging from 0 to 3 Hz, and again over a low amplitude range for frequencies ranging from 0 to 4 Hz. These tests were performed to duplicate the prototype testing of Gilbert (2007), and to check the linearity of the servos' amplitude response. The data obtained from this initial calibration agreed with that of Gilbert (2007) for low amplitude testing. For the high amplitude testing, strong nonlinearities were observed at the higher frequencies.

Following the initial unloaded calibration, the calibration procedure outlined above was performed again this time with the servo operating under normal experimental conditions (fully connected hydraulically, forcing flow into the water tunnel). This test was repeated to check the extent of the differences between the loaded/unloaded states. The calibration was performed for only the low amplitudes from the unforced cases; all amplitudes for both of these tests were measured using an LVDT. The unloaded and loaded cases differed very significantly, with percentage errors between the two cases ranging from a minimum of 10% to a maximum value of approximately 160%. These differences call into question the results of the prototype testing by Gilbert (2007).

An FFT was also performed on the data using spectral analysis tools in LabVIEW; the FFT quality was good (i.e. large spikes corresponded to the forcing frequencies, with no other discernable spikes at any other frequencies) for Strouhal numbers and amplitudes close to the optimum values, but deteriorated quickly when forcing at low amplitudes and frequencies.

## **G2: Manual Calibration**

The calibrations outlined in G1 provided us with good performance data for a single servo, but we had no way of knowing whether or not all of the servos were performing identically. A manual calibration to determine the degree of variability between each individual was performed, which tested all 22 actuators in the array at two operating configurations: one corresponding to a low Strouhal number, high amplitude forcing experiment; the other corresponding to optimal amplitude and Strouhal values. The displacements for each servo were measured manually and checked against the displacement value provided by the LVDT. Several servos were judged to be problematic, with amplitude responses 20% different than the mean amplitude response. These servos were then adjusted and re-checked, and were functioning normally at the time of data collection. The standard deviation in peak actuation slot velocities for the optimal and non-optimal runs were 8 mm/s and 24 mm/s respectively, which corresponded to roughly 9% and 13% of the mean values for those runs.

## **G3: Final Calibration Results**

At the time of writing this thesis, Marc Schostek was in the process of performing a detailed characterization of the forcing. After making several improvements to the servos (some of which were outlined in the “Future Work” section of the thesis), he performed the same 0 to 3 Hz calibration outlined in G1. However, he performed the calibration on 4 servos (#10, #12, #14, and #16) for multiple runs, making detailed measurements using the LVDT on each servo. He used a four stage analog Butterworth low pass filter to remove high frequency noise from the signals, and then performed total harmonic distortion spectral analyses on them.

The improvements made to the actuators drastically improved their performance; at the time of his final calibration, the servo position %THD values were almost all below 10% even in the poor performance range from the previous calibrations.